UCLA
UCLA Electronic Theses and Dissertations

Title
Reflective Terahertz Imaging for early diagnosis of skin burn severity

Permalink
https://escholarship.org/uc/item/51r0n1j4

Author
TEWARI, PRIYAMVADA

Publication Date
2013

Supplemental Material
https://escholarship.org/uc/item/51r0n1j4#supplemental

Peer reviewed|Thesis/dissertation

UNIVERSITY OF CALIFORNIA

Los Angeles

Reflective Terahertz Imaging

for early diagnosis of skin burn severity

A dissertation submitted in partial satisfaction

of the requirements for the degree

Doctor of Philosophy in Biomedical Engineering

by

Priyamvada Tewari

2013

ABSTRACT OF THE DISSERTATION

Reflective Terahertz Imaging

for early diagnosis of skin burn severity

by

Priyamvada Tewari

Doctor of Philosophy in Biomedical Engineering

University of California, Los Angeles, 2013

Professor Warren S. Grundfest, Chair

The work presented in this thesis explores the potential of Reflective THz imaging in early detection of skin burns. In the past decade, THz imaging has gathered a lot of attention for biomedical applications. Properties like sensitivity to water; low energy, non-ionizing nature, transparency to clothing and plastics, and less scattering compared to IR have led to the exploration of THz radiation for imaging of biological tissues. Several investigators have

reported the application of THz imaging in identification and differentiation between tissues, surface hydration detection and imaging of skin abnormalities both ex vivo and in vivo. The drawbacks with most of these findings are that they are preliminary and lack a sufficient sample size to make a significant claim.

The motivation for this research was provided by early work done by our group at University of California Santa Barbara, where the Reflective THz system was developed. Reflective THz systems' sensitivity to change in water concentration, a parameter defined as NEΔWC was calculated as 0.054%. This provided inspiration to image biological samples like deli meats, teeth, cornea and skin. The major breakthrough came when differences in hydration among artificially prepared ex vivo porcine samples were shown. This study incorporated a reasonable sample size and was shown to be repeatable. The next step was the exploration of a disease model that causes variation in surface hydrations in skin. The answer was skin burns. The first set of skin burn experiments were performed on ex vivo porcine skin. It was demonstrated that our system could visualize burns by creating a contrast between burnt and the surrounding unburnt region.

The next step was translation to in vivo settings. This thesis builds up from the discovery to proof of concept to repeatability of imaging skin burns with Reflective THz imaging system in live rats. Immediate edematous response followed by evolution of burn wound zones, reorganization, redistribution and dissipation of edema was captured in the Terahertz images of burns in rats over a span of three days. Experimental design, modifications and an attempt to quantify the findings are discussed. Statistical tests revealed that distinction among partial and

full thickness severities might be possible in early phases of injury. This gives THz imaging an edge over other imaging modalities like Infra red, Laser Doppler imaging and Polarization sensitive coherence tomography etc which are unable to detect the injured area early on. In this thesis we propose that early detection of skin burns is the clinical killer application of Reflective Terahertz imaging.

The dissertation of Priyamvada Tewari is approved

Harold G. Monbouquette

Tsu-Chin Tsao

Daniel B. Ennis

Zachary D. Taylor

Warren S. Grundfest, Committee chair

University of California, Los Angeles

2013

Table of Contents

List of figures

xiii

List of tables

Acknowledgement

This work like many other PhD's is a result of collaborative effort, guidance and supervision, and help from many organizations and individuals. Without contribution from any of the above, this thesis would not have been up to its degree.

My heartiest gratitude goes to Prof. Warren Grundfest under whose able guidance I was able to realize my full potential. I am extremely fortunate to have an advisor who was extremely considerate and put all his trust in me. His ingenuity and creativity not only reaped new ideas for the project but also inspired me to explore the unconventional route, which paid off in the end. Apart from guiding the project on the technical front, he also provided the big picture clinical perspective, which immensely helped in discovering the killer application for this novel technology. All of us in the Terahertz group have benefited from his guidance and support. My sincere thanks are due to my mentor Dr Martin Culjat, who recruited me, identified my strengths and helped me develop skills that were crucial for the project. Though being the only biologist in a team of engineers, he never let me feel out of place and emphasized the importance of diversity in a team. I will always be grateful to him for giving me this opportunity.

I am extremely proud of the Terahertz group where teamwork is exemplary. All the experiments that I have performed right from inception to data interpretation have been the result of combined effort from Dr Zachary D Taylor supervising the project on a day to day basis to graduate students David Bennett, Neha Bajwa, Shijun Sung and James Garritano helping with

I cannot appreciate and thank all my friends enough for helping me survive the vagaries of graduate school. Their support helped me fight the frustration and disappointment of failed experiments and emerge a stronger and more confident individual especially during the final stages of PhD. I was deeply touched when so many of friends despite their busy schedules attended my final defense.

Finally it would be unfair not to dedicate this thesis to my parents and dear brother. My mother, a PhD herself has been the strongest force in me pursuing and completing a work of this caliber. She has always maintained the importance and sanctity of this degree and taught me to be honest and conscientious. I'm grateful to my father for instilling a faith in higher education and the wisdom and enlightenment gained through it. He has always entrusted me with the confidence of achieving the impossible. I appreciate their patience and support and bearing the pain of not seeing me for long periods of time during these past six years. My loving brother who is also my biggest critic inspired me to improve all the time. His feedbacks and encouragement ensured that I didn't falter even once during any of the oral presentations I have given on my work including the final oral defense.

I consider myself blessed for getting all this support and guidance. PhD's are generally a bittersweet experience, for me more sweet than bitter. I'm truly grateful to god for making this experience worth all its while.

Curriculum vitae

Priyamvada Tewari

11140 Rose Avenue, Apt-101∗ Los Angeles CA-90034, (310)-968-2165 ∗priatewari@gmail.com

EDUCATION

University of California Los Angeles   **February 2012**
PhD in Biomedical Engineering; Dissertation title: "Applications of terahertz technology in medical diagnostic surface imaging"
UCLA graduate division fellowship (tuition &stipend)

Panjab University, India   **2006**
Masters (Honors) in Biophysics; GPA 4.0 **Thesis**: "Effect of alcohol on long bones in rat model"
S.R Bawa scholarship (Rs 10,000) for excellence in academics

Panjab University, India   **2004**
Bachelors (Honors) in Biophysics; GPA 4.0
Panjab University gold medal for outstanding academic achievement

WORK EXPERIENCE   **Present**
Marketing& Sales intern at M.H.M & Associates Enterprise, Inc.
- Identifying potential profit and nonprofit clients for funding from federal and state agencies
- Cultivating and fostering relationships with existing and prospective clients
- Writing and editing letters of intent, press releases and sections for grant applications

Contract editor at American Journal Experts
- Editing scientific journal manuscripts written by non native speakers
- Fixing grammar, spelling, punctuation and syntax

RESEARCH EXPERIENCE   **2007 - present**
Graduate student researcher at Center for Advanced Surgical and Interventional Technology (CASIT), UCLA
Involved in developing a non-invasive, high precision, user-friendly medical imaging technology for early detection of skin and eye disorders. Led the investigation from concept of simulation to successful in vivo studies.
- Established multidisciplinary collaborations with Departments of Surgery, Pathology and Dentistry
- Secured funding from - NIH ($2 million, 2010), H.M. Jackson ($500,000; 2010), TATRC ($300,000; 2008) &NSF ($300,000; 2008)
- Led in vivo animal trials for Terahertz in vivo skin burn imaging and corneal hydration at UCLA
- Obtained Animal Research Committee approval for first in vivo animal trial for Terahertz imaging of burns in rat &pig model

Collaborated with UCLA/Getty Conservation center for evaluating Terahertz system's capability for cultural heritage applications
- Identified art pigments and geometries and fabricated test targets representing real world frescos and seccos for preliminary evaluations
- Designed and machined mounts for holding art and parchment samples
- Modified and adjusted system to optimal settings for imaging specimens

MANAGEMENT EXPERIENCE   **2007 - 2011**
Coordinator &Mentor for two high school outreach programs -SMART& HSSRP with a total of 20 participants
- Devised, developed & implemented research curriculum for the 10 week programs
- Arranged special guest lecturers & lab tours in minimally invasive technologies

- Trained students in presentation skills and technical writing

Directed four undergraduate students' research
- Taught designing, machining and other experimental skills
- Supervised project progress and helped with research reports, evaluations and providing feedback

Teaching associate for Life sciences, Biochemistry, Bioethics & Physiology courses
- Led molecular biology & chemistry lab sections. Trained undergraduates in biology and chemistry experimental techniques
- Prepared educational hand outs and presentations for discussion sessions

ADDITIONAL EXPERIENCE   2002 - 2005
Doordarshan Public service broadcaster, India
- Talk show host for an hour long weekly live show
- Interviewed eminent personalities & covered important sports and cultural events
- Assisted show director in script writing & editing

PUBLICATIONS (PEER REVIEW JOURNALS)
- **P. Tewari**, C.P. Kealey, D.B. Bennett, N. Bajwa, K.S. Barnett, R.S. Singh, M.O. Culjat, A. Stojadinovic, W.S. Grundfest & Z.D. Taylor, "In vivo THz Imaging of Rat Skin Burns", Journal of biomedical optics, (2012)
- **P. Tewari**, C.P. Kealey, J. Sung, A. Maccabi, N. Bajwa, R. Singh, M. Culjat, W. Grundfest & Z.D. Taylor, "Advances in biomedical imaging using THz technology with applications to burn-wound assessment", Proc. SPIE 8261,(2012)
- **P. Tewari**, Z.D. Taylor, D. Bennett, R.S. Singh, M.O. Culjat, J.P. Hubschman, S. White, A. Cochran, E.R. Brown & W.S. Grundfest "Terahertz imaging of biological tissues" MMVR 18 (2011)
- **P. Tewari**, M. O. Culjat, Zachary D. Taylor, J. Y. Suen, B. O. Burt, Hua Lee, Elliott R. Brown, W. S. Grundfest & R.S. Singh, "Role of collagen in terahertz absorption in skin" Proc. of SPIE Vol. 7169 71691A-1, (2009)
- M.O. Culjat, D. Goldenberg, **P. Tewari**, R.S. Singh "A Review of tissue substitutes for Ultrasound imaging" Ultrasound in Medicine and Biology, 36(6), 861-873, (2010)
- D.V. Rai, G. Kumar, **P. Tewari** & D.C. Saxena, "Acute and chronic dose of alcohol affect the load carrying capacity of long bone in rat" Journal of Biomechanics, 41, 20–24, (2008)
- D.B. Bennett, Z.D. Taylor, **P. Tewari**, R.S. Singh, M.O. Culjat, W.S. Grundfest, D.J. Sasoon, R.D. Johnson, J.P. Hubschman, E.R. Brown, "Terahertz sensing in corneal tissues", Journal of biomedical optics 16(5), 057003, (2011)
- R.S. Singh, Z D. Taylor, **P. Tewari**, D. Bennett, M O. Culjat, H Lee, E. R. Brown & W. S. Grundfest "THz Imaging of Skin Hydration: Motivation for the Frequency Band" Proc. of SPIE Vol. 7555 755513-1, (2010)
- Z.D. Taylor, R.S. Singh, D.B. Bennett, **P. Tewari**, C.P. Kealey, N. Bajwa, M.O. Culjat, A. Stojadinovic, J.P. Hubschman, E.R. Brown, W.S. Grundfest, "THz Medical Imaging: *in vivo* Hydration Sensing", IEEE Transactions on Terahertz Science and TechnologySpecial Inaugural Issue, 1(1), (2011)

SKILLS
- Languages: English, Hindi, Punjabi, Urdu (spoken)
- Computing skills: Microsoft office, MATLAB, LaTeX, GIMP, Windows XP, Windows 7, Statistical software SAS
- Biology techniques: Cell culture, Histology, Electrophoresis, Western blotting, Radioimmunoassay, Animal handling
- Technical Designing: Microsoft VISIO, Adobe illustrator, Solidworks, CNC programming & machining
- Technical writing: Grant writing, protocol & scientific journal writing

OTHER ACOMPLISHEMNTS
- Government of India scholarship for training in classical vocal music (1992)
- One of 30 selected for the annual 'Communicating science' workshop with Alan Alda by Center for communicating science (2011)
- UCLA chancellors certificate for inter group dialogue on Race and Immigration in United States (2010)

CHAPTER -1: INTRODUCTION:

There has been tremendous development in the field of medical imaging in the past century. Imaging has now become an integral part of medicine with diagnosis relying heavily on imaging. Medical decision-making is to a large part dependent on the diagnostic capabilities rendered by different imaging modalities. The need for specificity and sensitivity in diagnosis, low cost, ease of operation, non-invasiveness, and minimal discomfort to the patient continues to motivate the development of new technologies.

One such emerging technology is Terahertz (THz) imaging. THz imaging involves the use of THz waves situated between microwave and infrared in the electromagnetic spectrum for generating images. Properties of THz waves like sensitivity to polar substances like water, transparency to clothing and plastics, low energy (1 - 12 meV), non-ionizing nature and less scattering compared to IR have led to the exploration of THz radiation for imaging of biological tissues. Contrast in skin, adipose tissue, striated muscle, and nerve tissue has been observed in the frequency range 0.5 – 1.5 THz demonstrating the potential ability of THz in differentiating between tissues[1]. Studies have reported the success of THz in identifying inflamed regions of skin, burns, psoriasis, basal cell carcinomas and melanomas[2-4]. These findings coupled with recent advances in THz generation and detection schemes have opened doors for THz medical imaging.

A very promising application of THz imaging from a clinical viewpoint seems to be the detection of skin disorders. Hydration is a key factor in determining the health of skin tissue.

Abnormal or diseased states in skin can be associated with an imbalance in hydration levels. For instance skin cancers and edema are associated with increased hydration while skin burns result in local dehydration[5, 6]. Therefore an accurate sensing of skin hydration levels could provide an early insight into diseased states like psoriasis, eczema, basal cell carcinomas and melanomas, detection of skin burns and wound healing. Not only this but monitoring skin hydration levels can impact drug delivery and absorption and qualitatively gauge the effectiveness of various cosmetic appliqués.

At present there is no standard technique for estimating skin hydration levels. While X-ray, ultrasound and MRI have become gold standards in bone, fetal, brain imaging etc, these modalities have not been very successful in diagnosis of skin disorders. The use of X-rays for skin has been hampered because of the invasive nature of the radiation. Ultrasound has been nascent in development due to lack of chemical specificity and cost factor and inability to resolve the first few micrometers has impeded the use of MRI for skin. Even though terahertz has poor resolution and lower penetration depth as compared to these modalities, it is aptly suited for skin imaging. Because of its extreme sensitivity to water, THz is able to capture slight differences in water concentrations and translate those variations into contrast. Water being the primary contrast mechanism in THz imaging obviates the need for any chemical or dye for enhanced contrast as in Raman spectroscopy. Moreover it is easy to read and interpret the images and locate the areas of abnormal activity based on the color scale.

The THz research group at University of Leeds carried out in vivo experiments to ascertain skin hydration levels using reflective THz imaging. Stratum corneum-epidermal

2

interface was visualized on the arm of a volunteer using their THz system. THz was able to resolve the two layers due to inherent differences in water concentrations between these layers. The topmost layer stratum corneum is relatively dehydrated as opposed to the epidermis thereby giving a large fraction of reflection from the stratum corneum – epidermis interface[4].

This thesis explores the potential of THz in becoming a clinical diagnostic tool for skin disorders. The focus of the research work is using reflective THz imaging for early detection and diagnosis of skin burns. Despite the decline in incidence of burn injuries over the last few decades, 1.25 million patients are still treated for burns annually in the United States[7].Most commonly used methods for estimating burn severity and depth is visual and tactile assessment[8]. These methods are highly inaccurate and invasive. The feasibility of THz imaging in detection of burn severity was originally reported using chicken breast as model[9]. Circular burns of varying severities were induced using an Argon laser. The changes induced in the optical properties of tissue by burns generated contrast between burnt and unburnt regions of tissue visible in the THz reflection image. Our group had imaged severe burns on ex-vivo porcine skin samples[10]. The burnt region in the image was clearly distinguishable from the surrounding unburnt region because of contrast. Despite these encouraging results obtained by our group and other groups a very small sample size has prevented from reaching any substantial conclusions.

The above shortcomings were overcome in this research work by employing a large sample size and statistically analyzing the data for significance. A reflective THz system developed in our lab operating at 0.5 THz (0.125 THz bandwidth) that raster scans the target was

used for all the experiments. The initial part of the thesis reports the calibration and feasibility experiments on biological tissues. Porcine skin a good mimic of human skin was used for hydration experiments whereby it was shown that THz is sensitive to distinguishing between different hydration states of skin. Ex-vivo skin burn experiments were based on the positive results from the hydration experiments. A detailed study involving a large sample size and four different burn temperatures was carried out to estimate the sensitivity of our system in imaging skin burns. High-resolution images of specimens were obtained where burnt and unburnt area could be distinguished with a high SNR. The success of the ex-vivo experiments motivated the in vivo burn study. In a rat model superficial, partial and full thickness burns were induced and imaged with the reflective THz imaging system. This was the first in vivo study involving THz for detection and monitoring skin burns. The burnt region was clearly visible and distinguishable from the surrounding normal area.

The purpose of this thesis is to prove the capability of reflective THz imaging in early diagnosis of skin burns. Through ex-vivo and in-vivo experiments it has been shown that THz imaging definitely holds promise in becoming a medical diagnostic tool for early detection of skin burns.

CHAPTER – 2: BACKGROUND – Why Terahertz for skin burn imaging

2.1 Terahertz (THz) waves

2.1.1 What is THz?

Terahertz band occupies the region of electromagnetic spectrum corresponding to frequencies between 0.1 – 10 THz (1 THz = 10^{12}Hz). For the purpose of this thesis we will define the frequency range from 0.3 – 3 THz, corresponding to wavelength range between 1mm and 100 μm. Flanked on the lower frequency end by microwaves and upper end by infrared, THz waves have a better resolution than microwaves and lower scattering as compared to IR. Properties of THz waves include sensitivity to polar substances like water, transparency to non-metallic and non-polar media, low ionizing power (4 meV at 1 THz) and much lower Rayleigh scattering as in IR[11, 12].
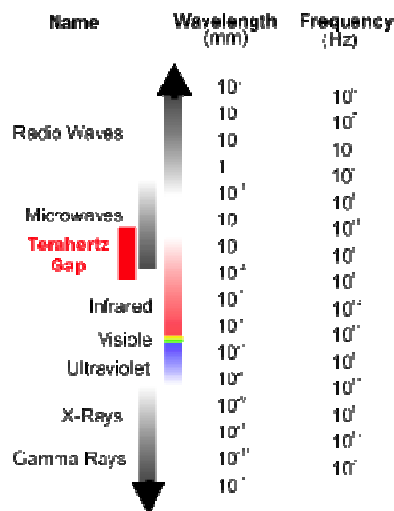
Fig 2.1: Electromagnetic spectrum highlighting THz gap

Many biological and chemical compounds have been found to have characteristic spectra in the THz range[13]. Fortuitously due to differences in water concentrations, tissues seem to have different THz reflectivity thereby permitting differentiation in the THz range[14]. A major advantage of THz radiation is transmission through clothing and fabric. This has important implications in medical imaging where wound healing can be monitored through bandages and casts. The energies of THz waves are in the order of meV, which is about a million times less than X-rays ensuring no damage to cells or tissues. Further because of longer wavelengths, scattering probability, which is inversely proportional to the fourth power of wavelength, is much more reduced.

2.1.2 Historical background:

THz band was considered elusive for a long time due to lack of sophisticated technology for generation and detection of THz waves. The region was identified as the band in the electromagnetic spectrum where neither optical nor electrical mechanisms dominate acquiring the name 'THz gap'. Far Infrared as THz was traditionally called was generated using either thermal sources or bulky molecular vapor lasers that produced weak and incoherent radiation. Detection schemes involved using liquid helium cooled bolometers that had very low sensitivity and gave a poor noise performance[9].

The breakthrough came with the advances in laser technology, semiconductor and crystal growth techniques and non-linear optics. The Auston switch developed in 1975 made generation of THz radiation possible by optically gating the photoconductive emitter. THz spectroscopy has been used extensively for security and astronomical applications for the detection of explosives, chemical agents and drugs for the past several years. THz imaging sparked interest in the

6

biomedical community following the first real time imaging demonstration by Huss & Nu in 1995[15]. They were able to obtain water distribution within a leaf and fat distribution in a piece of bacon using Terahertz time domain spectroscopy (THz-TDS). Mittleman used a chicken breast model to display the possible use of reflective THz imaging in estimating burn severity and depth[9]. Since then many groups have ventured into biomedical imaging with THz waves. Further, the development of Terahertz pulsed imaging (TPI) systems showed the potential of THz in medical imaging. Dental caries were detected using a TPI system with enamel, dentine and pulp visible in the THz image[16]. Tera View Ltd, at Cambridge has employed THz for early detection of basal cell carcinomas. Tumors are associated with higher water content and this generates a contrast between the healthy and carcinomatous regions in the THz range. Experiments were done on both in vitro samples and in vivo. The same group was also able to visualize stratum corneum epidermis junction on the arm of a volunteer and evaluate skin hydration levels [2,4,17,18].

2.1.3 THz wave interaction with biological materials

At the macroscopic level, the ability of the medium to be polarized defined as electric permittivity (ε) and bulk conductivity (σ) which is the measure of the ease of movement of ions through a medium are two parameters that can be used to describe THz wave interactions with tissues. Tissues can be considered to be a collection of molecules like water and proteins. For understanding THz tissue interaction at the microscopic level an insight into molecular and quantum energy levels is required.
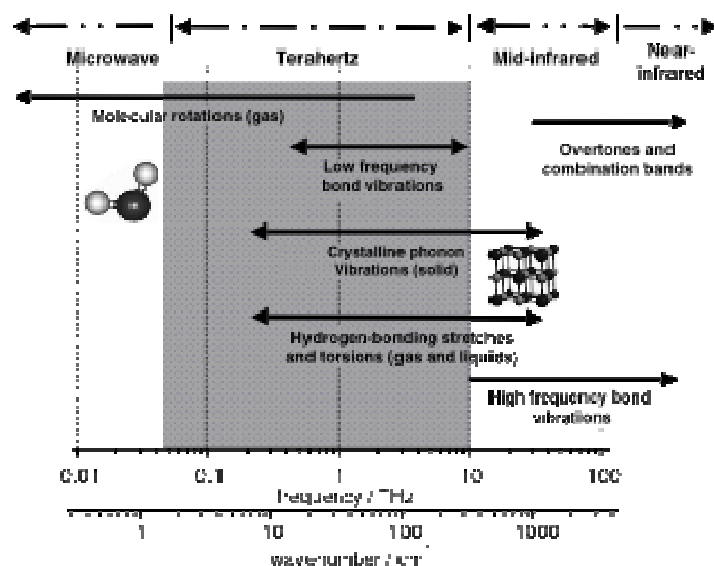
Fig 2.2: Molecular transitions in the THz region

For diatomic molecules (atomic mass < 20), the energy of separation between rotational states is $\Delta E \sim 1.602 \times 10^{-22}$ J corresponding to 0.242 THz and between low lying vibrational levels is 1.6×10^{-20} J implying that the absorption of THz radiation leads to changes in rotational and vibrational modes of polar diatomic molecules. Another motion exhibited by polar diatomic molecules in the THz band is librations. Librations are restricted oscillatory motion of molecules[11]. All these molecular movements are more pronounced in case of polar molecules that forms inter and intra molecular hydrogen bonds. The rotational, vibrational and translational transitions in the THz range are specific to the molecule and therefore many biological compounds have distinct THz spectra.

The most abundant polar diatomic molecule in biological tissues is water. Because of this abundance and extreme sensitivity to THz, signature features from other molecules in tissues can usually be ignored while studying the response to THz. For instance, the refractive indices of

8

many tissues are found to change in the frequency range 0.1-1 THz depending on their water content. These differences in water concentrations are a source of image contrast.

2.2 Skin Burns

2.2.1 Skin anatomy and physiology

Skin tissue comprises the outer external covering of the body forming the first line of defense against toxins, physical insult and radiations.

Fig 2.3: Skin layers

9
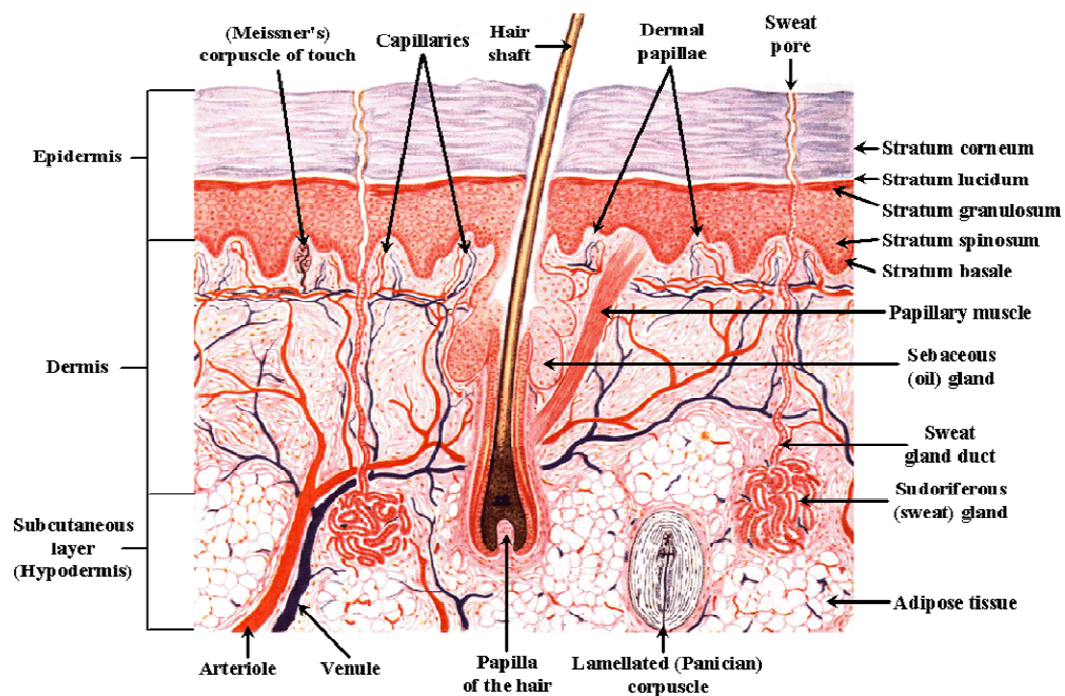
Skin consists of mainly two layers - the outer stratified epidermal layer and an inner dermal layer. Subcutaneous or hypodermis lies beneath the dermal layer. The components of epidermis are keratinocytes (95% of epidermis), melanocytes, langerhans cells, merkel cells, inflammatory cells and lipids. Dermis comprises of two fibrous proteins – collagen (making up the bulk of dermis) providing tensile strength and elastin, which provides elasticity. The proteins are embedded along with polysaccharides in a supporting matrix also called ground substance. Cellular components of dermis are mast cells, fibroblasts and macrophages.

The average thickness of human epidermal layer is ~0.1 mm. The epidermis can further be divided into four layers: stratum corneum, stratum granulosum, and stratum spinosum and stratum basale.

Fig 2.4: Hemotoxylin & Eosin stained longitudinal section of skin showing different layers

Stratum corneum, the topmost cornified layer of epidermis maintains the barrier function of skin. The thickness may vary from 10 μm in eyelids to 40 μm on the soles of feet. The composition of the stratum corneum is 10-25 layers of corneocytes embedded in a lipid matrix. Corneocytes are keratinocytes that have lost nuclei and cytoplasmic organelles upon their migration from stratum basale. Keratin filaments fill up these flattened cells. Lipid composition of stratum corneum is formed from ceramides, cholesterol and fatty acids. It is the combination of this unique lipid composition and keratin filaments that results in lower permeability to water making stratum corneum relatively dehydrated as compared to the deeper granular layers. A water gradient has been found to exist in the stratum corneum .The effectiveness of stratum corneum as a barrier is dependent on its water content, with healthy stratum corneum having water content above 10% weight/weight (w/w). Below this level, skin loses its flexibility and develops a rough scaly appearance. Hydration is therefore a key factor in determining the health of skin tissue. Burns, drug delivery, cosmetics, cancer, and edema are examples where the measurement of hydration levels is important. Skin burns result in loss of water from outer skin layers whereas skin cancers and edema are associated with local increases in hydration of the skin surface[5, 6]. Cutaneous wound repair is also influenced by hydration, with water content varying with the stage of repair and the type of wound[19]. Specifically, early acute wound scars are more hydrated than normal skin, while older chronic wounds have been found to be drier[20]. Finally, hydration is critical to the cosmetics industry in testing the efficacy of cosmetics, with many cosmetics intended to prevent and repair skin damage by moisturizing the outer layer.

Depth resolution scales of THz and sensitivity in detecting hydration changes make THz ideal for imaging and monitoring moisture levels of stratum corneum. Since many skin disorders result in a disruption of the barrier of stratum corneum, THz imaging can give an early lead in detection of diseased states.

2.2.2 Skin burns introduction

Despite the decline in incidence of burn injuries over the last few decades, 1.25 million patients are still treated for burns annually in the United States. Of these approximately 50,000 require hospitalization[21, 22]. Mortality associated with burn injuries is the fifth leading cause of unintentional injury-related deaths with the majority of injuries caused by flame/flash burns[23, 24]. Other causes of skin burns include contact with hot objects; scald burns chemical burns, electrical burns, and others. According to the National Burn Repository Report 2009, men constitute 71% of burn patients with a mean age of 32. Health care for patients suffering from skin burns is one of the most expensive aspects of our health care system, with burn related injuries accounting for almost 13% of all medical claim costs[25] and 31% burn patients having no medical insurance[26]. A direct correlation has been reported between severity of burns, length of hospital stay, and cost[27]. It has been reported that mean length of stay for patients suffering from thermal burns is nine days and average healthcare costs for a patient with thermal burns ranges from $30,000 to $118,000[28]. In addition to cost, burn injuries are associated with physical complications due to muscle weakness[29, 30], hypertrophic scarring[31-35], contractures[36], nervous system injury[37-39] and psychosocial problems. Burn wound

management and rehabilitation includes daily management of pain, posttraumatic stress, depression, and anxiety[40].

Clinically, burns are categorized by depth of tissue involvement. Superficial thickness burns involve only the epidermis. Partial thickness burns involve the dermis and are subdivided into superficial and deep partial thickness by their involvement of the papillary and reticular dermis. Finally, full thickness burns are those that have completely obliterated the dermis and involve underlying structures such as subcutaneous fat, fascia, and muscle.
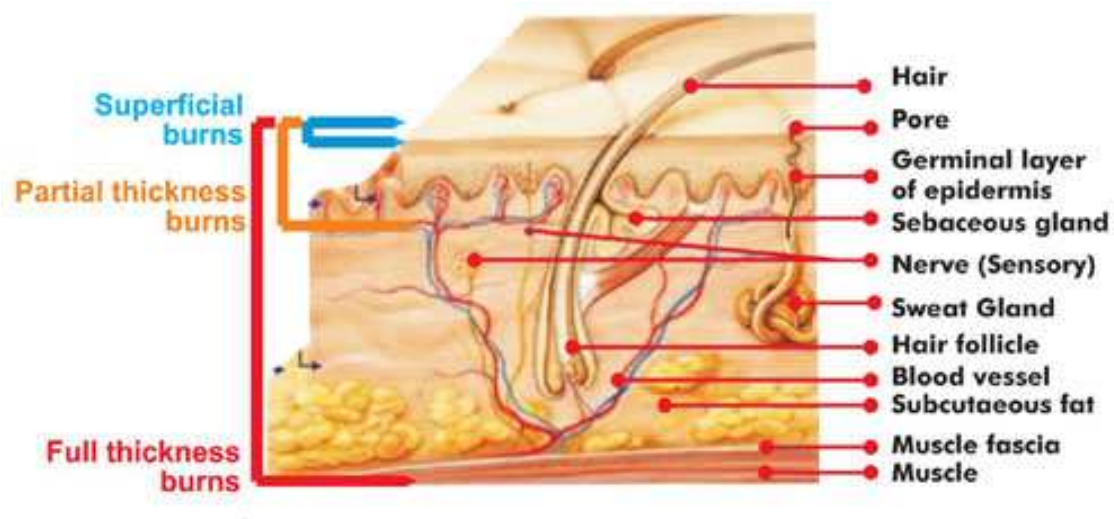
Fig 2.5: Skin burn classification

The burnt area usually comprises of three concentric zones – outer zone of hyperaemia, middle zone of stasis and inner zone of coagulation. The zone of hyperaemia appears red due to increased perfusion and is metabolically active. Zone of stasis is initially red but turns white between third and seventh day post injury because of the avascularity and necrosis of dermis and

hemolysis of red blood cells. The area of maximum and irreversible damage is the zone of coagulation characterized by a complete obliteration of vessels[41].
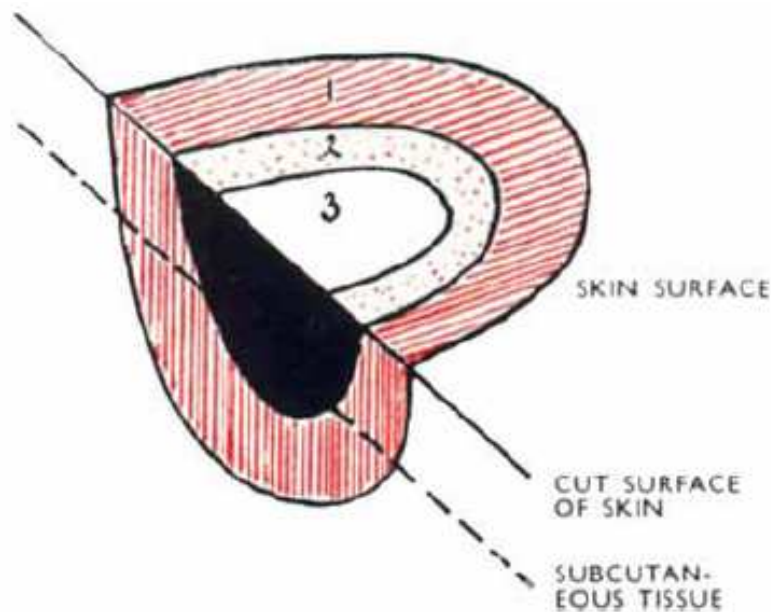
Fig 2.6: Burn zones (1) Zone of hyperaemia, (2) zone of stasis, (3) zone of coagulation[42]

Full thickness and deep partial thickness burns are generally treated by skin excision followed by skin grafting. It has been observed that within a week following surgery, the zone of stasis turns white in color making the zone of coagulation and stasis indistinguishable. At this stage both these zones may become necrotic and damage irreversible. Zone of stasis is the region of ischemia and vascular stasis. Upon reperfusion this area can be restored[43]. Early identification of the three burn zones can help in monitoring the zone of stasis. Further it can

14

help guide the surgical excision process where many a time's viable tissue is lost due to excision of a larger area. Terahertz imaging can be used both for the surgical treatment of burns and also monitoring wound healing.

2.2.3 Burn severities

Severity of a burn in defined in terms of burn depth, total surface area of the burned region (a percentage value), location of the burn and age. Burn depth is determined by the anatomic thickness of skin involved in thermal damage. Burns are classified as – superficial, partial thickness and full thickness. A superficial burn is confined to the outer layer of epidermis while a partial thickness burn involves epidermis and part of inner dermis. Full thickness burns involve damage to both epidermal and dermal layers.

Table 2.1: Burn severity, etiology and healing

Degree/dept	Etiology	Layer of skin involved	Appearance	Healing time
Superficial I°	Sun exposure, hot liquids with low viscosity and short exposure	Epidermis only	Pink to red, moist, no blisters	3–7 days
Superficial partial IIa°	Hot liquids, chemical burns with weak acid or alkali, flash	Superficial (papillary) dermis	Blister, red, moist, intact epidermal appendages, blanches of pressure	1–3 weeks, long-term pigment changes
Deep partial IIb°	Flame, chemical, electrical, hot liquids with high viscosity	Deeper layer (reticular) dermis	Dry, white, non-blanching, loss of all epidermal appendages	3–6 weeks, with scars
Deep III°	Flame, electrical, chemical, self immolation	Full thickness of skin to the subcutaneous fat or deeper	Leathery, dry, white or red with thrombosed vessels	Does not heal requires skin graft

Superficial thickness burns are not considered significant burns and heal within a week. Partial thickness and full thickness burns on the other hand require medical attention. The healing of these burns is highly dependent on treatment and wound management[44].

Partial thickness

Partial thickness burns involve destruction of the epidermis and part of dermal layers. Depending on the extent of damage partial thickness burns can be further sub classified as superficial partial thickness and deep partial thickness.

In superficial partial thickness burns entire epidermis and upper third of dermis is damaged. Capillaries perfusing the region are injured and become permeable leading to leakage of large amounts of plasma. The burnt region appears pink, wet and may have blister formation. Superficial partial thickness burns heal within 1 to 2 weeks with no scarring. Treatment involves cleansing the wound area and debridement of loose epidermis and removal of large blisters. Skin substitutes are rarely required but can be used for wound surface protection and healing.
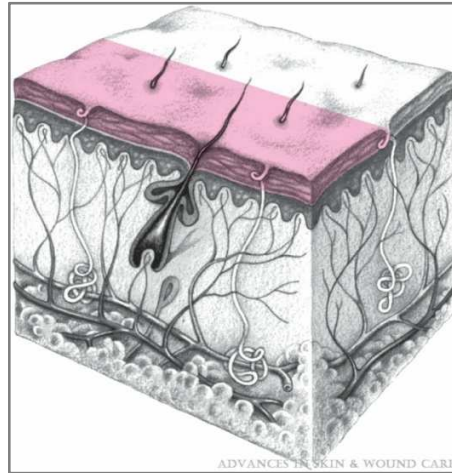
Fig 2.7: Representation of a superficial partial thickness burn

Deep partial thickness burns involve destruction of epidermis and most of the dermis. Vascular perfusion is diminished and nerve endings are destroyed. The burn wound is white and dry in appearance with no blister formation. Continued ischemia in the wound region can lead to wound progression and conversion to a full thickness burn. Healing of these wounds can take up to 10 weeks. Scar formation is common. Treatment involves eschar removal and debridement. Early excision and grafting can speed up the healing process and minimize scarring.
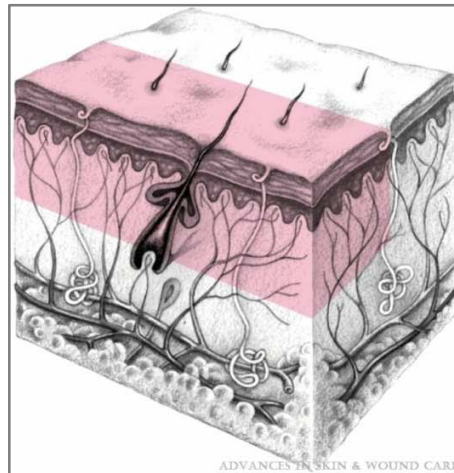
Fig 2.8: Representation of a deep partial thickness burn

Full thickness

Full thickness burns result in complete destruction of epidermis and dermis. Thermal insult leads to complete coagulation of blood vessels and sensory nerves. The wound appears waxy white but may have a brown leathery appearance if the wound extends into the subcutaneous tissue. Treatment includes early surgical debridement and wound closure with a skin graft or skin substitute.
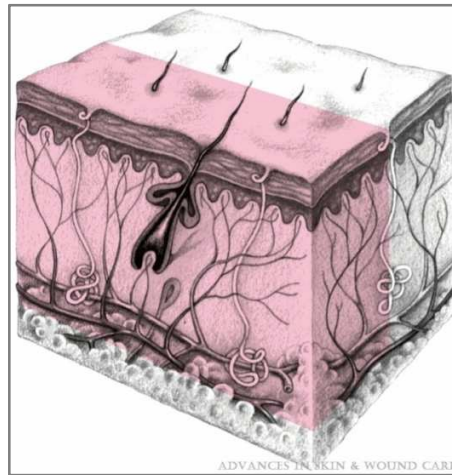
Fig 2.9: Representation of a full thickness burn

2.2.4 Pathophysiological response to thermal injury

Local changes in burn wound

Temperatures in excess of 40° C cause denaturation of cellular proteins and loss of plasma membrane. The resulting molecular structural alterations and cellular necrosis cause the burn wound. Toxic burn products; acidosis, poor tissue perfusion, fluid loss and shifts are some of the immediate local effects[45, 46]. Jackson first described the correlation of the surface appearance of the burn with the depth of necrosis. The burn wound can be divided in three zones as per the extent of damage – zone of hyperemia, zone of stasis and zone of coagulation. Local disturbances and fluid shifts across these zones define the extent of burn injury and further elicit inflammatory and systemic response. The outer zone of hyperaemia, area of least damage appears red characterized by increased circulation and high metabolism. This zone is characterized by the loss of epidermis but fully intact dermis. Usually this zone is fully healed within a week. The intermediate zone of stasis appears red initially but changes to white by day

19

three. Metabolism is diminished and superficial capillaries are dilated and packed with red cells. By day seven, superficial dermis is necrotic and dermal vasculature has collapsed. The central zone of coagulation takes the brunt of thermal injury. The region comprises of coagulated tissue and obliterated vasculature and is beyond healing. By the end of first week only two zones – coagulation and hyperaemia are visible. Continued ischemia in the zone of stasis leads to further tissue loss causing the region of stasis to coalesce with the zone of coagulation[42].

2.2.5 Edema formation

The response of vascular tissue to local injury is defined as inflammation. Thermal injury elicits a rapid inflammatory response that walls off the damaged area and kicks off a series of wound healing processes. One of the early and most prominent signs of inflammation is edema formation[47]. Edema is accumulation of fluid in interstitial spaces. Thermal insult not only causes physical injury to the capillaries but also releases mediators like histamine or globulins, which increase capillary permeability allowing for fluid leakage into interstitial spaces. This fluid is rich in protein [48-50]. The pathophysiological response to burn injury causing rapid edema formation are increased microvascular permeability, vasodilation, increased extravascular osmotic activity along with the release of local mediators like histamine, serotonin, bradykinin, nitric oxide, oxygen free radicals, prostaglandins, thromboxane, TNF, interleukin etc. Physiochemical alterations in the extravascular and extracellular matrix further increase wound edema by forming osmotic and hydrostatic gradients[46, 51]. Demling summarizes the different pathophysiologic changes in burn tissue that lead to edema[52].

- Marked immediate and sustained increase in rate of fluid and protein crossing from capillary to the interstitial space

- Early disruption of the integrity of the interstitial space with disruption of collagen and hyaluronic acid scaffolding

- Progressive increase in interstitial space compliance as edema forms

- Marked transient decrease in interstitial pressure caused by the release of osmotically active particles, causing a vacuum effect sucking in fluid from the plasma space

- Marked and sustained increase in capillary permeability in the burn wound

- Decrease in plasma proteins and oncotic pressure and increase in interstitial protein and oncotic pressure due to increased capillary permeability to protein

- Inability to maintain a plasma to interstitial oncotic gradient

- Likely a transient increase in capillary hydrostatic pressure in the burn capillaries

- Marked and sustained decrease in the surface area of the perfused capillaries and lymphatics

- Increase in the ease of fluid accumulation in the interstitium.

The rate and quantity of edema formation depends on burn severity. A critical temperature of 55° C has been identified below which no edema forms.

<u>Superficial thickness burns</u>

Superficial burns are associated with minimal necrosis. Vascular perfusion is high initially but decreases gradually. Edema formation is minimal.

Partial thickness burns

Because of better vascular perfusion the rate and quantity of edema is found to be higher in the partial thickness burns. Edema formation is rapid following partial thickness injuries with almost 80% increase in tissue water content as early as 10 min post injury[53]. Peak edema formation in a 10% partial thickness burn was noted at 3 hrs post injury in one study[54]. In another study maximal edema was found at 6 hrs post injury for a partial thickness burn[55]. The site of edema formation is the epidermal-dermal junction. Fluid resorption begins nearly 24 hrs after the burn and is nearly complete by day 4[52]. The rates of fluid resorption are also found to be faster after a partial thickness burn. Better vascular perfusion and intact lymphatics are thought to be responsible for this.
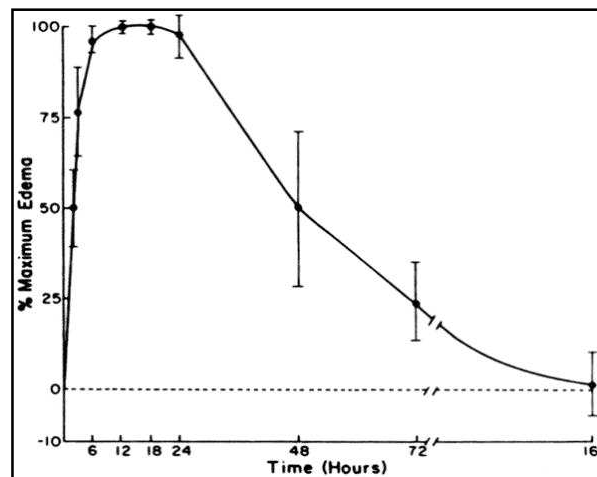
Fig 2.10: Edema formation in a partial-thickness burn. Edema is measured by photon scanning. Time course of edema formation and resorption in 10 hind limbs with a partial-thickness burn is shown, comparing mean +/- SD of percent fluid content over baseline against time after burn. Maximum edema is present between 12 and 18 hours, with 94% of edema present at 6 hours. Resorption began at 24 hours and is nearly complete by 4 days[52].

22

<u>Full thickness burns</u>

Full thickness burns involve necrosis and complete obliteration of dermal vasculature. Vascular perfusion is significantly decreased limiting edema formation[56]. Maximum edema was noted around 18 hrs following burn in one study [52]. The site of edema formation is dermis. Fluid is sequestered in the subdermal space with a deep burn and resorption is slower. Resorption begins at about 24 hrs. Dermal lymphatics are destroyed impairing resorption.
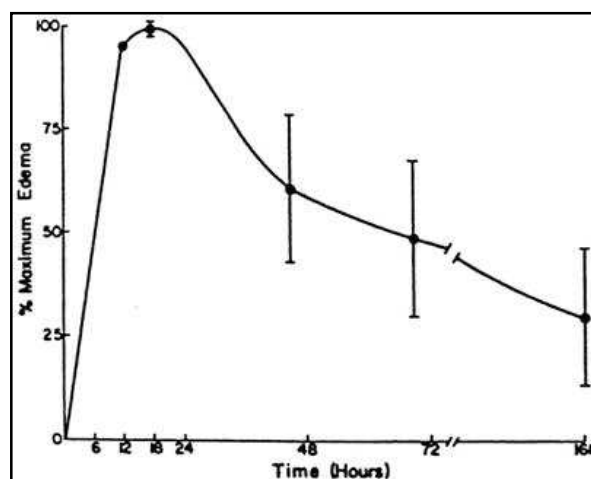
Fig 2.11: Edema formation in deep burn. Time course of edema formation and resorption in 10 hind limbs with a partial-thickness burn is shown, comparing mean +/- SD of percent fluid content over baseline against time after burn. Maximum edema is present 18 hours, after burn injury. Resorption began at 24 hours and but 25% still remained at 1 week [52].

2.2.6 Wound healing

The burn wound contains a variety of cell types including platelets, neutrophils, lymphocytes, macrophages and fibroblasts. The principal molecular regulators controlling the

23

evolution of burn wound include vascular endothelial growth factor (VEGF), platelet-derived growth factor (PDGF) and transforming growth factors[46]. The three phases of wound healing are –inflammation, tissue formation and tissue remodeling. Inflammation involves infiltration of neutrophils, macrophages and lymphocytes in the wound zone. Macrophages perform two major functions - initially they engulf and phagocytose wound debris, clearing the way for growth of new dermal matrix. Subsequently macrophages produce angiogenic and fibrogenic growth factors that promote the growth phase of repair. Inflammatory phase is followed by tissue repair and reepithelialization. The process involves migration and proliferation of epidermal cells, macrophages, fibroblasts and blood vessels in the wound space. Fibroblasts deposit the new extracellular matrix while macrophages produce necessary growth factors to induce fibroplasia and angiogenesis. This supports cell ingrowth and sustenance. Provisional extracellular matrix is gradually replaced with collagen matrix[57]. The newly formed granulation tissue further undergoes angiogenesis till the wound is completely filled with granulation tissue. The wound undergoes contraction and extracellular matrix reorganization whereby granulation tissue transitions into scar tissue.

2.2.7 Burn wound progression: Importance of early burns detection

Thermal injury triggers a series of pathophysiologic mechanisms that can result in deepening of the burn wound, a phenomenon called burn wound progression. A time frame of three to five days is estimated for the consolidation of burn depth. During this time the burn wound is in a dynamic state under the influence of primary and secondary mediators resulting from thermal injury causing more tissue loss[58].

At the molecular level, the direct effect of heat leads to disruption of cell membranes and denaturation of proteins. This is followed by activation of toxic inflammatory mediators and byproducts like superoxides, hydroxides, and hydrogen peroxide. Free radicals along with oxidants and proteases enhance ischemic tissue necrosis in the zones of stasis and hyperemia. Edema and altered perfusion play a major role in conversion of partial thickness to full thickness injuries. Prostaglandins, histamine and bradykinin all products of inflammatory response increase vascular permeability causing both local and systemic fluid shifts that aggravate hypoperfusion in the zones of stasis and hyperaemia[59]. Elevated bradykinin levels have been considered responsible for coagulation and stimulating microthrombosis in the zone of stasis contributing to the progression of partial thickness to full thickness burns. Presence of vasoactive and inflammatory mediators in higher than normal concentration in and around the wound causes vasoconstriction of microvasculature limiting perfusion in the partially burned tissue, advancing to full thickness necrosis[60]. Local hyperemia and desiccation decrease perfusion via shifts in intravascular and interstitial fluid volumes inhibiting oxidative metabolism in vulnerable zones. Finally nutritional and metabolic deficiencies, acidosis etc may contribute to ischemia of viable tissue causing eventual tissue death[58].

Burn depth and extent dictates treatment. Superficial thickness burns can be treated with topical therapy and do not often need supervision but partial thickness and full thickness burns require immediate medical attention. The confounding factor in treatment of severe burns is wound progression. Accurately assessing, which burns will convert, and determining how to prevent burn wound conversion remain a clinical challenge. The burn wound comprises of the outermost zone of hyperaemia, which heals spontaneously, and the intervening zone of stasis

where blood flow is reduced and skin suffers from ongoing hypoxia. This ischemic skin can readily convert to nonviable tissue without proper restoration of flow resulting in the conversion of a partial thickness burn to a full thickness burn and extension of burn size. As the extent of wound advancement increases, so does the likelihood of hypertrophic scarring, contractures, need for surgical excision and grafting, burn wound infection, sepsis, shock and possibly death. The goal of treating partial thickness burn wounds is thus to promote healing while minimize scarring and contracture. Current mainstays of the treatment of partial thickness wounds include adequate fluid resuscitation, nutritional support, and local wound care, with an emphasis on topical microbial agents and biosynthetic dressings. Deep partial thickness and full thickness burns on the other hand are treated via excision of eschar followed by skin grafting. Full thickness burns should be treated as soon after resuscitation as is feasible by excision of eschar and skin grafting since excision and skin grafting are bloody procedures if prolonged. Prompt burn eschar excision with immediate wound closure not only has better cosmetic outcome but also decreases mortality and shortens hospital stay. It is often easier to excise the entire area of burned skin and subcutaneous tissue to muscle fascia but that may sacrifice significant amounts of viable skin. To conserve surface and subjacent skin during surgery, areas of skin that will spontaneously must be differentiated from areas that will not heal within 2 weeks and therefore require surgical excision and grafting. Early detection and monitoring of vulnerable zones can help conserve tissue and speed the treatment process.

2.2.8 Current imaging modalities

Diagnostic techniques that have been applied to the detection and quantification of skin burns include green dye fluorescence, laser Doppler perfusion imaging (LDPI), polarization sensitive optical coherence tomography (PS-OCT), thermography, ultrasound and nuclear magnetic resonance (NMR)[61]. Among these existing techniques PS-OCT and LDI have shown the most promise[62]. Both techniques have the advantage that they are non-invasive and are non-contact measurement techniques, but suffer from various limitations. LDPI fails to provide a resolved depth resolution and is affected by tissue curvature, pathophysiological aspects of burns, and scanning distance. PS-OCT measures change in the optical polarization of tissues resulting from thermal destruction of collagen fibers by detecting only the direct-reflected photons. It suffers from strong optical scattering and is unable to distinguish between degrees of skin burns[63]. Therefore the clinical motivation to develop a non-invasive technique that would be able to detect and diagnose skin burns, monitor the healing process, and be user friendly and cost effective is tremendous.

Infrared (IR) imaging has also been explored as a non-invasive technique for burn imaging. One study reported the successful use of IR imaging in distinguishing between partial and full thickness burns on the basis of temperature difference on the surface of burn wounds[64]. Surface temperature of burn wounds was found to decrease with increasing burn depth as time progressed. Another study demonstrated the use of active-dynamic IR imaging in distinguishing between repairable and irreparable burn wounds. A preliminary clinical study using near infrared imaging (NIR) imaging with indocyanine green (ICG) as a contrast agent

demonstrated a correlation between IR detection of burn depth and histology[65]. However, IR imaging suffers from scattering effects, limited contrast between tissues and monitoring for long periods of time[66]. Moreover prior studies have had limited sample sizes and therefore have not yet clinically established the efficacy of the modality.

2.3 Terahertz skin interactions

2.3.1 Terahertz sensitivity to skin reflectivity

Dielectric properties of a tissue are described in terms of permittivity (ε) and conductivity (σ). For frequencies below 100 Hz relative permittivity of a tissue is in the order of 10^6 or 10^7. At frequencies higher than this, the relative permittivity decreases in three steps - α, β and γ dispersions. α and β dispersions are predominant at lower frequencies and are associated with ionic diffusion processes and polarizations at cell membrane boundaries. The γ dispersions are found in the GHz region and arise from the relaxation of water present in the tissue[67]. Since the dominant polarization mechanism in tissues at higher frequencies is due to dipolar relaxation of water molecules, the THz tissue interaction can be understood by exploring the dielectric behavior of water in the THz regime[68].

In the THz band, water is observed to fit a double Debye model with a slow relaxation time (τ_1) and a fast relaxation time (τ_2). Dielectric relaxation for water incorporates H-bond rearrangement, structural rearrangement and translational and rotational diffusion[69]. The slow relaxation mode can be attributed to structural and H-bond rearrangement that involves breakage of H-bonds and reformation while the fast relaxation may be due to reorientation.

The relaxation times and permittivity's can be calculated using the equation

$$\hat{\epsilon}(\omega) = \epsilon_\infty + \frac{\epsilon_s - \epsilon_2}{1 + i\omega\tau_1} + \frac{\epsilon_2 - \epsilon_\infty}{1 + i\omega\tau_2}$$

where ϵ_s isthe static dielectric constant, ϵ_2 is an intermediate frequency limit & ϵ_∞ is the limiting value at high frequency.

Several groups Ronne et al, Kindt and Schmuttenmaer, Smye et al etc have published the double Debye parameters for water. Relaxation times are calculated as τ_1 ~8.2 - 8.4 ps and τ_2 ~ 0.17 - 0.19 ps[11, 70, 71].

Water, which makes up 70% of skin by weight, is expected to dominate the dielectric properties of skin. Pickwell et al modeled skins response to THz radiation[69]. Forearm skin was chosen and treated as a homogenous layer. Similarly, Alekseev et al showed that forearm skin because of thinness of SC could be modeled as a homogenous layer[72]. The permittivity values obtained by their group were found to be similar to experimentally observed values. Pickwell et al used finite-difference-time-domain to calculate the Debye parameters for both water and skin at 298 K and correlated it with measured values. A good correlation was found (correlation coefficient 0.97) between the simulated and measured values. The relaxation times for water were τ_1 ~ 10.6 ps and τ_2 = 0.18 ps and for skin were τ_1 ~ 10 ps and τ_2 = 0.20 ps. The permittivity values of water and skin were ϵ_s= 78.8, ϵ_2= 6.6, ϵ_∞= 4.1 and ϵ_s = 60, ϵ_2= 3.6, ϵ_∞= 3 respectively.

This property can be exploited for diagnosing diseased states of skin where imbalances in water concentrations can generate contrast.

2.3.2 Primary contrast mechanism

Contrast in THz range is due to slight variations in water content. The refractive index of water is around 80 at 1 GHz but drops to 2 between 0.5 to 1 THz. Absorption coefficents for water are high in the THz range leading to significant dielectric losses[73]. Further because of variations in water content biological tissues are found to have different THz absorptivities[74].Absorption coefficents of tissues are highly dependent on their water content with lower attenuation coefficents for tissues with lower hydration levels. For instance adipose tissue has a lower attenuation coefficent than striated muscle. The water content of striated muscle ranges from 73 to 77.6 wt% while its between 5 to 20 wt% for adipose tissue. Fitzgerald et al explored optical properties of excised human tissues in the range 0.5-2.5 THz and discovered different refractive indices and absorption coefficents for skin, adipose tissue, striated muscle, vein and nerve. However because of very high absorption coefficent THz is unable to pennetrate deep into tissues making reflective imaging and spectroscopy more feasible than transmission mode.

Taylor et al defined a parameter noise equivalent delta water concentration (NEΔWC) for their reflective THz imaging system that was used for the experiments reported in this thesis[12]. This metric defines the minimum change in water concentration by volume that the imaging system is able to detect. This parameter defines the sensitivity of a THz imaging system to

variations in water concentrations and can be considered analogous to the noise equivalent temperature difference (NETD) for Infrared thermometric imaging[75].

The parameter was experimentally calculated by measuring change in THz reflectivity of fully saturated clean room wipes (polyester/cellulose blend) with time as their weight dropped with subsequent evaporation of water. The sample was dried over a span of 87 minutes with a drop in weight from 130 mg to 40 mg. A mean drop in weight of 1.42 mg between measurement points and a constant drop of 0.02% per min in reflectivity was observed during the 87 min time period between 4.65% and 2.85% reflectivity.
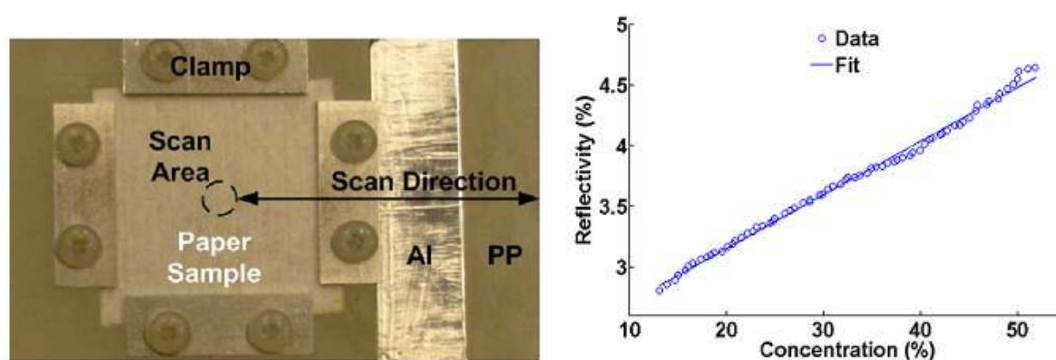
Fig 2.12: Change in THz reflectivity as a function of drop in water concentration

A near linear relationship was found between THz reflectivity and water concentration. From the reflectivity and weight data a noise equivalent delta water concentration (NEΔWC) was calculated to be 0.054%. This implies that the reflective THz imaging system would be able to

31

generate contrast between regions differing in water concentration by as little as 0.054% by volume.

2.3.3 Imaging skin abnormalities with THz waves

The growing popularity of THz imaging has led many research groups to venture into medical imaging. The properties of THz waves make it aptly suited for imaging skin. Cause and effect of skin abnormalities can be attributed to imbalances in water content, which can be captured by THz imaging.

Toshiba Research Europe Ltd at Cambridge did one of the initial in vivo skin imaging experiments. A reflective imaging system was used to take measurements off normal skin on the arm of a volunteer. The experiment involved taking measurements from the forearm before and after hydration to gauge the systems sensitivity to changes in water concentrations. The stratum corneum-epidermal junction was visualized for normal skin. Also stratum corneum water levels were deduced from the reflected THz waveforms. Woodward et al used Terahertz pulsed imaging to image in vitro basal cell carcinoma specimens and showed that they could be distinguished from normal skin. Tumors are associated with higher water content which translates to contrast in the THz range thereby allowing differentiation of normal regions from cancerous regions. Teraview Ltd reported contrast between normal skin and carcinomatous lesions both in vitro and in vivo.

The above results are very encouraging for early detection and monitoring of skin burns and cancer, conditions like psoriasis, eczema, dermatitis, evaluation of cosmetics etc for which hydration profiling of SC could provide an insight.

2.3.4 Promise of THz imaging in skin burn detection

The proficiency of reflective THz imaging in visualizing burns was first reported by Mittleman[76]. A contrast between burnt and unburnt regions was observed in chicken breast. A series of circular burns of increasing severity were induced in the chicken breast with an argon laser. The THz image resolved all zones of burn severities by generating a contrast between them. The contrast was attributed to variations in water contents between each circular region. Dougherty et al used chicken skin as a model for burn studies. A sever burn was inflicted by a branding tool heated to 350° C[77]. The burnt region was clearly visible in the THz image. Taylor et al employed porcine skin, a close mimic of human skin for imaging burns[10]. A brass brand heated to 315°C was pressed against ex-vivo pig skin for ~3 s to inflict a severe burn. A clear distinction between burned and surrounding unburned was apparent from the THz image. A 75% drop in reflectivity was recorded between the two regions giving a high SNR. The primary contrast mechanism was identified as local variations in water caused by burning.

2.3.5 Comparisons with other imaging techniques

Clinically established techniques like X-ray, MRI and ultrasound could never establish a foothold in skin imaging due to several reasons. X-ray is highly invasive with intensity levels nearly a million times as compared to terahertz. MRI has previously been used for detecting and determining the extent of malignant melanoma, lymphoderma and squamous cell carcinoma [78-80]. However because the thickness of skin is in the order of millimeters, current MRI systems sensitivity and resolution does not do justice in resolving different layers of skin. Especially disorders involving stratum corneum (thickness 15μ), MRI fails to provide any information due

33

to its inability to resolve this layer. High-resolution ultrasound imaging has been successful in evaluating epidermal thickness and resolving the different skin layers[81, 82]. Despite having a good penetration depth, the lack of chemical specificity and spatial resolution has prevented the use of ultrasound as a diagnostic tool for skin disorders.

1.25 million patients are still treated for burns annually in the United States. Of these approximately 50,000 require hospitalization[22, 83].Early detection of skin burns and estimation of extent and severity still remains a challenge in clinical settings. The most commonly used methods for estimating burn depth are visual and tactile assessment;[i] these methods are highly inaccurate despite being performed by experienced medical personnel with successful prognosis only in 50-70% of cases[8, 84]. Biopsy of wounds followed by histopathology is the gold standard, but not commonly performed because of being local and invasive[85].

Diagnostic techniques that have been applied to the detection and quantification of skin burns include green dye fluorescence, laser Doppler perfusion imaging (LDPI), polarization sensitive optical coherence tomography (PS-OCT), thermography, ultrasound and nuclear magnetic resonance (NMR)[86]. Among these existing techniques PS-OCT and LDI have shown the most promise[87]. Both techniques have the advantage that they are non-invasive and are non-contact measurement techniques, but suffer from various limitations. LDPI fails to provide a resolved depth resolution and is affected by tissue curvature, pathophysiological aspects of burns, and scanning distance. PS-OCT measures changes in the optical polarization of tissues resulting from thermal destruction of collagen fibers by detecting only the direct-reflected

34

photons[88]. It suffers from strong optical scattering and is unable to distinguish between degrees of skin burns[89].

Infrared (IR) imaging has also been explored as a non-invasive technique for burn imaging. One study reported the successful use of IR imaging in distinguishing between partial and full thickness burns on the basis of temperature difference on the surface of burn wounds[90]. Surface temperature of burn wounds was found to decrease with increasing burn depth as time progressed. Another study demonstrated the use of active-dynamic IR imaging in distinguishing between repairable and irreparable burn wounds[84].A preliminary clinical study using near-infrared imaging (NIR) imaging with indocyanine green (ICG) as a contrast agent demonstrated a correlation between IR detection of burn depth and histology[91]. However, IR imaging suffers from scattering effects, limited contrast between tissues and monitoring for long periods of time [84, 90, 92]. Moreover prior studies have had limited sample sizes and therefore have not yet clinically established the efficacy of the modality.

There exists a need for a non-invasive modality that is able to accurately quantify the extent or severity of burns. Such a technique may enable improved management of burn injuries by providing a highly accurate quantitative measure of burn severity and extent, therefore allowing for more accurate triage and improved monitoring of burn injuries. Cost effectiveness and ease of operation are additional clinical motivations.

Terahertz has the potential of becoming a clinical diagnostic tool for early detection and diagnosis of skin burns. Properties of THz waves as discussed earlier are conducive to the surface and sub surface skin imaging. Preliminary results obtained by other research groups and

our group have shown promise in the ability of reflective terahertz imaging in detecting burns via contrast. This thesis further explores the feasibility of THz imaging modality in not only detecting skin burns early on but also differentiating between superficial, partial and full thickness burns. Chapter 6reports the ex-vivo burn experiments on porcine skin using a reflective terahertz system. A large sample size was included for the reproducibility, repeatability and statistical significance of the data. The results were very encouraging in imaging different burn severities and the results were found to be statistically significant. Further chapter 7 discusses the in vivo skin burn experiments. Male SD rats were used for the study in line with previous burn models. We were successful in imaging and distinguishing between burn severities on live rats.

To our knowledge these were the first in vivo experiments that utilized terahertz imaging for visualization of burns. Also the potential of THz imaging in burn monitoring was explored by imaging burns over a time period of three days. The ex-vivo and in-vivo experiments have been instrumental in substantiating our claim about the capability and potential of our system in detecting and diagnosing skin burns and other skin disorders for the detection of which no standard techniques exist!

CHAPTER – 3: TERAHERTZ GENERATION AND DETECTION

3.1 THz generation and detection schemes

The THz region of the electromagnetic spectrum was considered evasive for a long time due to lack of efficient generation and detection mechanisms. With technological advancements, rapid progress has been made in THz generation and detection in the past decade.

3.1.1 THz sources

Broadband THz waves can be produced by either of the two schemes

I) Photoconductive emitters: This method of generation involves creating carriers (e-hole pairs) in a semiconductor material with an optical laser pulse. The photoconductive material instantly changes from being an insulator to a conductor. Under the influence of an electric field these carriers accelerate generating a photocurrent. The rapid rise and fall of photocurrent produces electromagnetic waves in the THz frequency range. GaAs, InP and InAs are popular materials of choice for photoconductive emitters. The construction of GaAs photoconductive switch is discussed in detail in the next section. Metal electrodes are patterned onto the semiconductor substrate in the form of an antenna with a few micrometers between them.The laser pulse excites the electrons across this band gap, which is under a bias voltage. The photon energy of the laser pulse has to be comparable to the band gap of the emitter for THz generation. Femtosecond lasers like mode locked pulsed Ti:sapphire lasers are most commonly used for excitation. These lasers have wavelengths short enough to accelerate the movement of electrons across the band gap, low average power and high repetition rate. THz pulse bandwidth depends on the fast and

efficient rise and fall of photoconductor. Drift velocity and breakdown field are other material properties that determine THz intensity and bandwidth. Bandwidths of 1 THz are easily achievable but may reach up to 4 THz.

II) Optical rectification: In optical rectification no bias voltage is applied. An ultrafast laser pulse from a Femtosecond laser passes through an optically non-linear material. The material undergoes polarization at high optical intensities. THz waves are produced as a result of these rapidly changing electrical polarizations in the material. $LiNbO_3$ and $LiTaO_3$ are non-linear crystal materials of choice. Phase matching between the laser pulse and THz pulse from the crystal, duration of laser pulse, non-linear coefficient and thickness of crystal dictate the efficiency and bandwidth of resultant THz waves. As compared to photoconductive generation, the THz waves generated via optical rectification have lower output powers. The conversion efficiency is also lower though the bandwidths are much larger reaching up to 50 THz.

3.1.2 Detection schemes

THz sensors range from superconductor bolometers to heterodyne sensors. Coherent detectors are best suited for biomedical imaging and spectroscopy. The two most commonly used schemes for coherent detection are photoconductive detection and electro-optical sampling. Both detection schemes involve mixing the THz pulse with a part of the original laser pulse. An optical delay line ensures the simultaneous arrival of both pulses.

I) Photoconductive detection: The mode of operation is antithesis to photoconductive emission and is generally used in conjunction with photoconductive sources. Photoconductive antennas are used for this detection scheme. Electric field of THz pulses generates a bias across the

38

antenna, giving rise to a transient current. This current is amplified and the detected current is representative of the THz field strength. It has been reported that photoconductive antennas based on low temperature grown GaAs are capable of ultrahigh bandwidth detection (frequencies in excess of 60 THz).

II) Electro-optical sampling: The principle behind electro-optical sampling is pockels effect. Bifringence is induced in a crystalline material (Zn:Te crystals) by the electric field of the THz pulses. The change in the optical polarization of the detection pulse caused by bifringence is proportional to the electric field strength of THz. Further amplitude and phase information can be derived from the polarization of the beam. Laser pulse duration and crystal thickness affect the bandwidth of detection with reported detections in excess of 100 THz when thin sensors are used.

3.2 Terahertz imaging systems

3.2.1 Pulsed systems

Terahertz pulsed imaging and spectroscopy has been used for biomedical applications like tissue differentiation, disease detection etc. Terahertz pulsed systems comprise of a Femtosecond laser, THz source, pair of optical transducers and a detector. The laser pulse is split in two components – pump and probe. The pump is used to excite the THz source, which could either be a photoconductive antenna or a non-linear crystal. Generally photoconductive antennas are used. The generated THz pulse after scanning the target is fed into a detector where it mixes

with the probe beam from the laser. Parabolic mirrors are used to focus and collimate the THz beam onto the target and then into the detector. The signal is amplified, down converted to radio frequency range and detected. Pulsed THz systems have high bandwidths, high signal to noise ratios (SNR's) and can provide depth information.
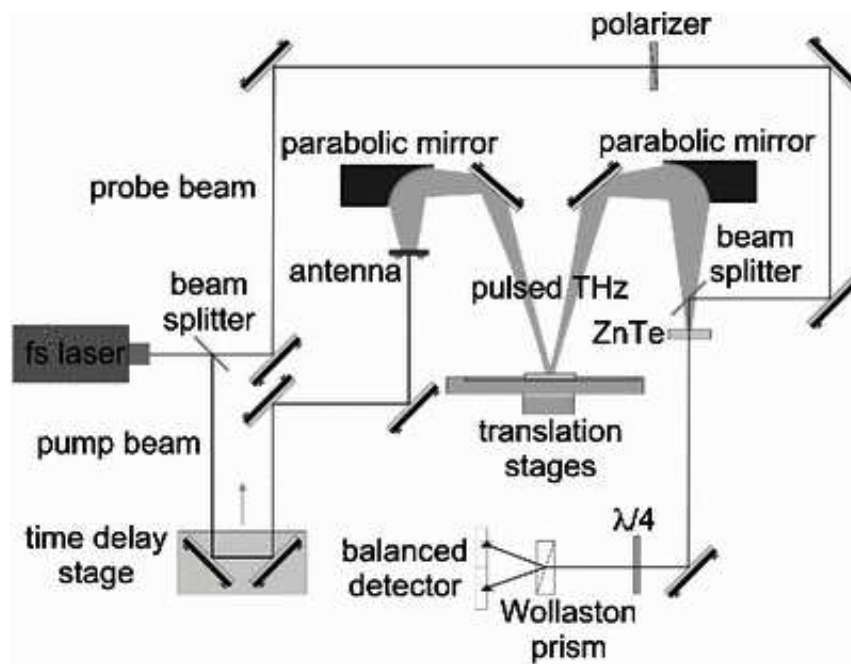
Fig 3.1: Pulsed Terahertz imaging system[93]

3.2.2 Continuous wave systems (CW)

Unlike pulsed imaging systems, continuous wave imaging systems do not require complicated optical arrangements making them simpler and cheaper as compared to the pulsed systems. Two tunable laser sources operating at different wavelengths are photomixed to generate THz radiation. By selecting the operating wavelengths and line widths of the two lasers,

desired frequency in the THz range can be produced. Narrow frequency ranges or even monochromatic THz waves can be generated with this set up. The resultant THz waves have a higher spectral power density at a particular frequency as compared to the pulsed generated waves. Both photoconductive and electro-optic detection has been demonstrated. A major requirement for continuous wave THz generation and detection is that the two laser sources have to be coherent. Ti:sapphire lasers are most commonly used as laser sources. LT-GaAs is the popular photomixer though some continuous wave generation schemes do not require emitters. As mentioned earlier, CW systems are much less complicated and cheaper. Image formation is fast due to lack of long delay lines. For applications requiring resolution of narrow spectral details like molecular signatures, CW imaging and spectroscopy is suited. However for biomedical imaging, pulsed systems are preferred since they can provide depth information and broadspectral details.
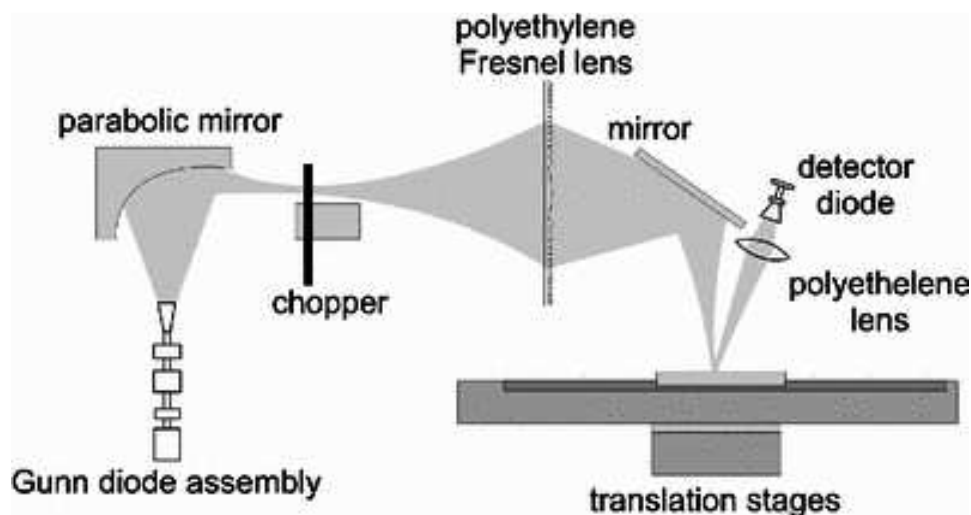
Fig 3.2: Continuous wave THz imaging system[93]

3.3 Pulsed THz imaging systems:

Pulsed terahertz imaging systems can be operated either in reflection or transmission mode. The construction varies in the placement of the detector.

3.3.1 Transmission THz imaging

In transmission mode the detector is placed beneath the sample under investigation. The radiation propagates through the material and the transmitted THz waveform is measured. Phase as well as amplitude information is captured and either or both can be used to generate images. Transmission mode has been used to determine absorption coefficients, refractive indices of materials including tissues. Applications of systems operating in transmission mode have also been in security like detecting explosives and quality control. Transmission of THz radiation through a material is dependent on absorption as well as attenuation characteristics of the material. Crawley et al used pulsed terahertz imaging in transmission mode for detecting carious lesions in teeth. THz attenuation spectra of teeth showed a higher absorption for caries as compared to healthy enamel[94]. Contrast between healthy and carious regions was apparent in the images generated from the absorption data.

Transmission set ups are limited by the thickness of the specimen. Materials that are absorptive to THz radiation also attenuate it thereby rendering them less meaningful to reflective imaging. This is particularly relevant in case of biomedical imaging. Transmission imaging requires preparation of very thin specimens in order to obtain transmitted waveforms. This could be done for investigating biopsied or ex-vivo specimens but is not possible for in vivo imaging.

a)
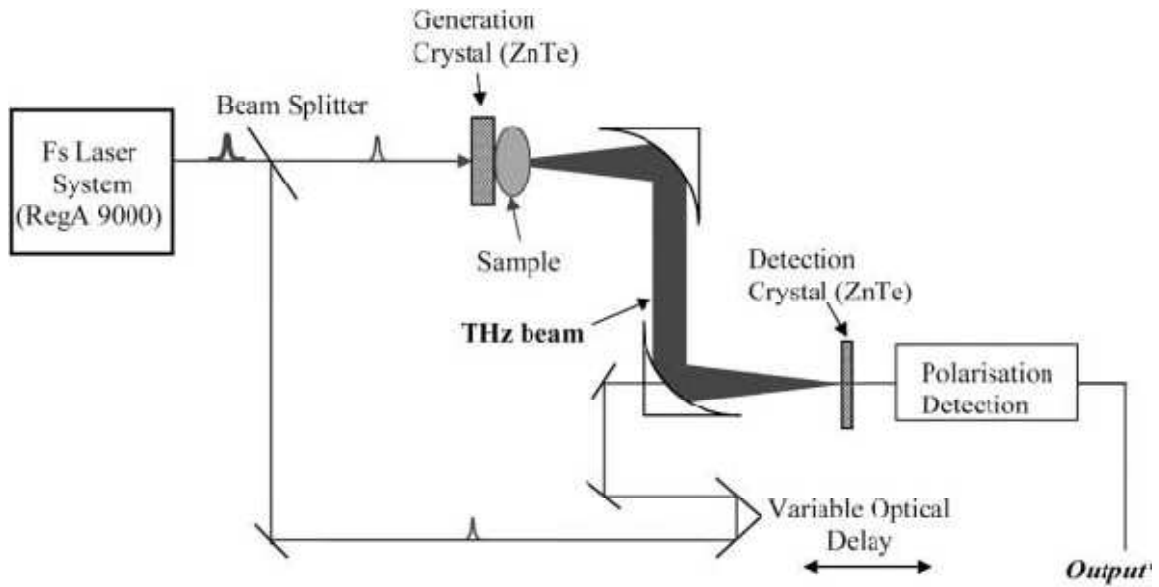
b)
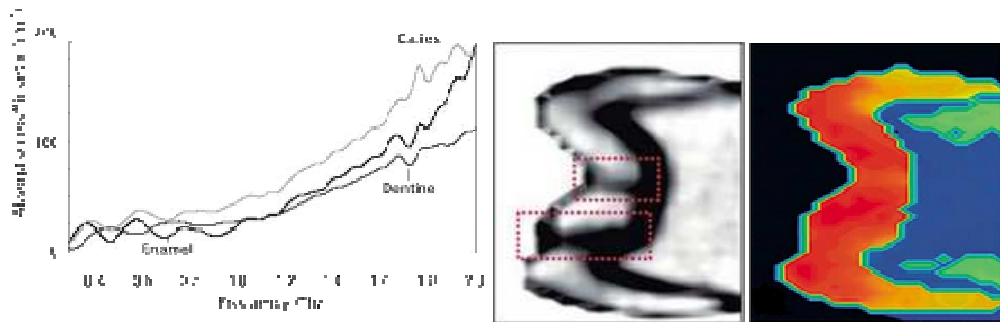
Fig 3.3: (a) Transmission THz imaging system (b) An image of tooth generated by plotting the change in intensity of the terahertz pulse as it passes through the sample at different x and y values, corresponding to a map of terahertz absorption in the sample. Note that the caries lesions are easily detected. A false color image generated by plot- ting the change in time of flight of the principal terahertz peak as it passes through the sample at different x and y values. This corresponds to refractive index changes[95].

43

3.3.2 Reflective THz imaging

The detector is positioned on the same side of the material under investigation so as to capture reflections off the sample. A pair of parabolic mirrors is used to focus the reflected THz radiation into the detector. The reflected waveform contains both amplitude and phase information and can be used to generate images. Reflectance depends on index of refraction, surface roughness, polarization and other geometric factors. Even though clearer images can be obtained in transmission mode reflective systems are more popular. Bulky samples are impossible to image with transmission systems. Reflective THz imaging has gained popularity in security screenings because they are more applicable and practical for standoff detection. By studying reflected waveforms it is possible to visualize several layers in an object and also predict thickness of each layer. This has implications in security screenings where detection of explosives or weapons beneath several layers of clothing is desirable. Materials that are highly absorptive to THz radiation cannot be imaged with transmission set ups due to high attenuation. These include biological tissues. Human body is about 70% water. Tissues have been found to have different THz absorption characteristics mainly due to differences in water concentrations. These characteristics are captured in reflection mode where a contrast is created between areas differing in water contents. Reflective THz imaging systems are thus more practical for biomedical imaging.

Crawley et al[95] also imaged teeth in reflection mode. THz pulses reflected from the surface of the teeth were used to generate an image. It was observed that enamel was more

reflective than dentine due to a higher refractive index appearing lighter in the image. This led to differentiation between enamel and dentin.

a)
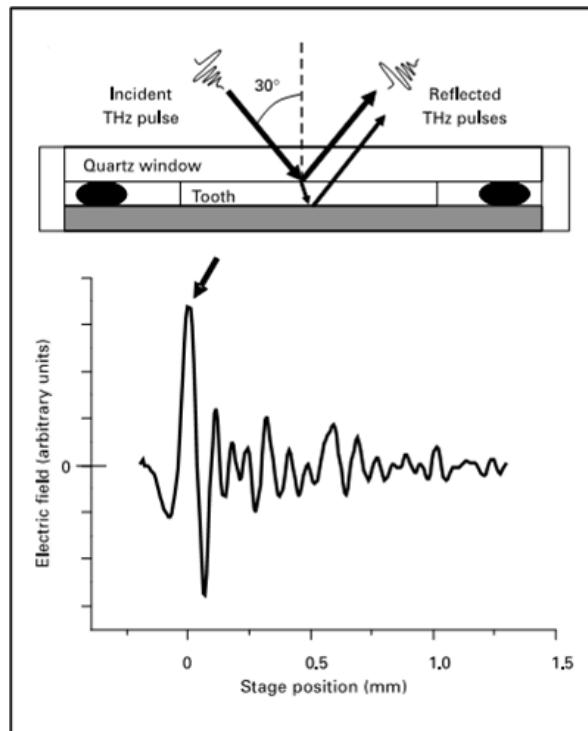
b)
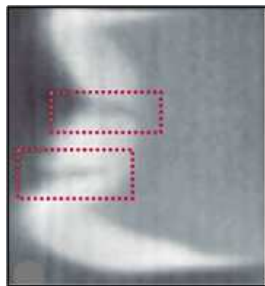
Fig 3.4: a) Mounting of the samples for reflection imaging b) An example pulse in reflection. The strongest feature (indicated by the arrow) would dictate the time delay used to plot reflection images. The height of the pulse at this chosen time delay would be used to make up the reflection image[95].

The work presented in this thesis is with the use of a reflective pulsed THz imaging system developed in our lab. The potential of the technology and our system is in early detection of skin burns is demonstrated through a series of experiments. The construction and working of the system is described in the next section.

3.4 System design

Reflective THz imaging system comprises of a Femtosecond laser, source, off axis parabolic mirrors and a detector.

3.4.1 Photoconductive switch

Our reflective THz imaging system employs a photoconductive switch for the generation of terahertz. Since the development of photoconductive switch by Austin in 1984, these have been used for the broadband generation of terahertz. It has been shown that GaAs is the popular material of choice for photoconductors due to high resistivity, high carrier mobility and high breakdown field. The addition of ErAs nanoparticles to GaAs further increases the breakdown voltage and decreases the carrier lifetime. The short pulses arising in the semiconductor-nanoparticle assembly give rise to broadband THz pulses.

The construction of our photoconductive switch is as follows. A layer of GaAs serves as the substrate and is overlaid with an AlAs:AlGaAs layer acting as a reflector. The heat spreader layer of AlAs is laid on top of the reflector. A thin layer of GaAs:ErAs with patterned metal follows this. ErAs nanoparticles are introduced through molecular beam epitaxy leading to the

46

formation of single crystal ErAs islands in GaAs. A thin layer of silicon nitride caps off this assembly. Silicon nitride prevents oxidation and provides anti reflection coating.
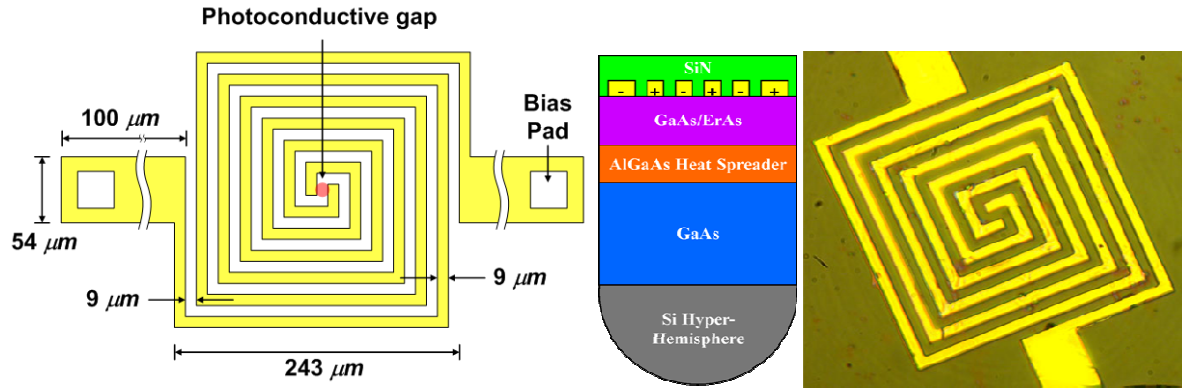
Fig 3.5: Schematic (left) and picture of the Austin switch used for THz generation. GaAs:ErAs is the photoconductive active layer. Gold is patterned onto this layer in the shape of a planar antenna. The antenna is a three-turn square spiral at the end of which extend two bias lines that are used for electrical biasing and bonding. The THz pulse emitted from the switch is nearly collimated with a divergence FWHM of ~8°.

The performance of the photoconductive switch was measured using a Golay cell (NEP ~2x10-10 W Hz-1/2, responsivity = 10 mV/μW). The average THz output power was found to be 103 μW while achieving an optical-to-electrical conversion efficiency of 1.3%. The peak power was calculated at 2.2 W for a limited pulse width of 2.2 ps. The spectrum was measured with a Michelson interferometer using a 50 μm Mylar beam splitter and a He-cooled, composite bolometer. Water lines are observed at 557 GHz and 752 GHz in the measured spectra. The broadband output is the result of short electron-hole recombination time (~0.25 ps) and efficient radiative coupling through the lens mounted spiral antenna.

47

3.4.2 Construction and working of Reflective THz imaging system

The active imaging system developed in our lab operates in reflection mode at 0.5 THz with ~125 GHz bandwidth. A 780 nm mode locked laser pumps the photoconductive switch at a repetition frequency of 20 MHz to generate THz radiation. The photoconductive switch is coupled to a silicone hyperhemisphere for producing a nearly collimated beam with a FWHM of ~8. This directive beam is collimated and focused by a set of parabolic mirrors to strike the target at 45°. The target is raster scanned in both horizontal and vertical directions using stepper motors at a defined step size. The reflected beam is collimated and focused by another set of mirrors into the feed horn of a zero-bias Schottky detector. A gated microwave receiver comprising of a double balanced mixer and an integrator follows the Schottky detector. The reflected THz beam is rectified, amplified (BW=10 GHz, G=+40 dB) and fed (passed) into a double balanced mixer where it interferes with the reference pulse from the laser. To synchronize the two pulses, the reference pulse is passed through a RF delay line. Following the mixer, a digital voltmeter (DVM) with a 16 ms time constant and an integration factor of ~3.2 x 10^5 discretizes the signal to a digital output with 40 dB post detection SNR. It is ensured that the target remains at a 45° incidence with respect to incident and reflected wave. Image acquisition time depends on the dimensions of pixels that can vary from 0.1 mm to 1 mm.
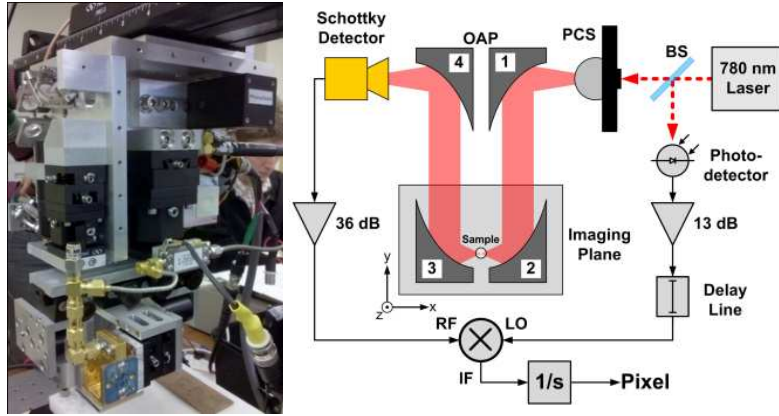
Fig 3.6: Visible pic (left) of the imaging head and (right) schematic of reflective THz imaging system

An effective center frequency of 525 GHz (0.5 THz) with bandwidth of 125 GHz is calculated by superimposing the spectral responsivity of Schottky diode detector with power spectrum of the photoconductive switch. This bandwidth is sufficient to overcome speckle from standing waves between source and detector and its cut on frequency is high enough to still provide good spatial resolution.
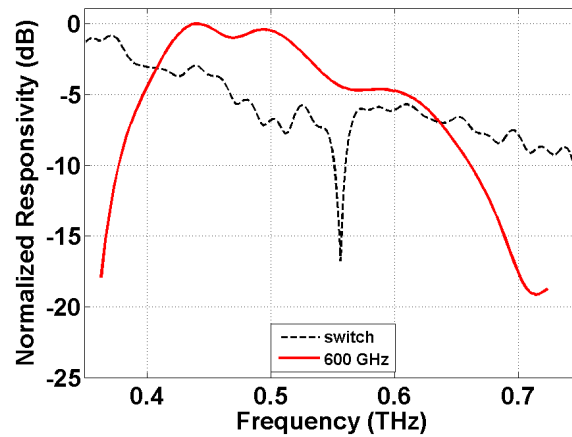
Fig 3.7: Normalized power spectral responsivity of zero-bias Schottky detector superimposed on the power spectrum of photoconductive switch

Even though information lies in the phase of the reflected signal, the system receiver must be considerably more complex to extract these additional spectral features. In our system and the applications under consideration we have determined that the additional information embedded in the phase does not justify the added receiver complexity hence we do not acquire the phase with our system. Though details of a target are contained in the phase of the reflected radiation, it is complicated to retrieve this information. For complex morphologies like skin, a reference reflector would be required at the same positions for a precise measurement. Thus for biomedical imaging applications for which our system has been designed we only take amplitude information into account.

3.4.3 Why 0.5 THz?

Bennett et al have identified the 400 GHz - 700 GHz range as the optimal band for effective system operation[96]. Key factors that were taken into consideration were sensitivity to water concentration, scattering and spatial resolution.

a)   b)   c)
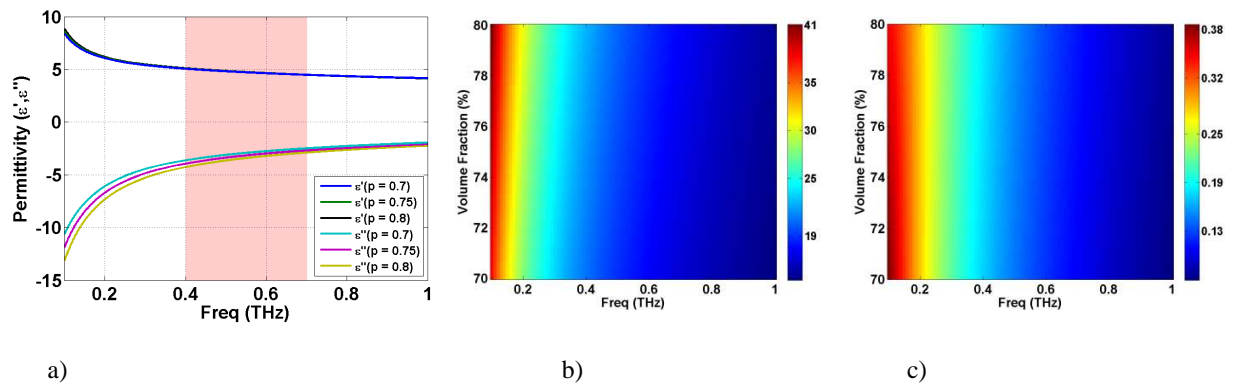
Fig 3.8: a) Approximate skin dielectric constant as calculated with Bruggeman effective media theory and stratified media theory. b.) Power percent reflectivity of skin as a function of water concentration and frequency assuming a specular surface. c.) Hydration sensitivity calculated as a % change in power reflectivity per % change in water concentration by volume.

50

Skin is 70 to 80 % water. Dielectric properties of skin are dominated by that of water. This was shown by using double Debye relaxation model and Bruggeman dielectric theory. Skin with thin SC can be modeled as a homogenous layer. The effective complex dielectric constant of skin was calculated for water volume concentrations of 70%, 75%, and 80%. The frequency and water concentration dependent skin reflectivity is shown with a 100 GHz to 1 THz frequency range on the x-axis, a 70% to 80% water concentration by volume range on the y-axis, and the power reflectivity in % represented by the colorbar where blue corresponds to lower reflectivity and red corresponds to higher. As is expected by the dielectric properties of water, skin displays a higher reflectivity at lower frequencies. Taking derivative of the figure performed a sensitivity calculation. The calculation shows a clear advantage of operating at lower frequencies.
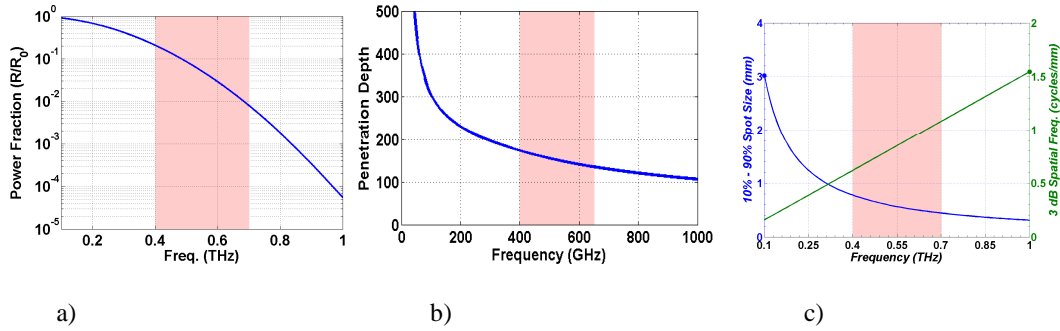

Fig: 3.9: a) Scattering simulation using typical values measured for skin. The figure shows the decreasing specularity for increasing frequency b.) Penetration depth in the cornea c) Spatial resolution assuming a gaussian beam profile and a 25 mm focal length, 25 mm diameter primary objective lens.

51

Surface roughness and curvature lead to scatter in THz images. Bennett et al modeled skin roughness as a Gaussian distribution of heights and slopes. The received power dropped 4 orders of magnitude from 100 GHz to 1 THz.

In single pixel whiskbroom imaging systems, spatial resolution is dictated by the spot size on target. Bennett et al explored this concept by computing a spot size on target using a high numerical aperture, 25 mm effective focal length off-axis parabolic mirror with a 25 mm clear aperture 90% filled by the THz beam. The results are displayed in (blue) and represent a practical bound on THz beam focusing assuming an aberration free mirror and perfect THz beam gaussianity. As expected, higher frequencies produce smaller spot size for a given optic with 100 GHz illumination providing a 3mm spot size and 1 THz providing ~ 350 um a spot size.

Considering the pros and cons of both, we can conclude that for biomedical imaging operating frequency of 0.5 THz is optimum.

3.5 Calibration results

3.5.1 Spot size characterization and depth of focus

It has been shown that if the exciting laser pulse has a Gaussian intensity profile, the emitted THz pulse in the far field follows a similar Gaussian beam pattern. The beam waist is dependent on the spot size of the pump laser pulse[97, 98].

Gurtler et al confirmed this Gaussian behavior of the propagating THz beam by fitting the frequency dependent experimental spot size with the spot size of an ideal Gaussian beam[99]. The ideal spot size of the THz beam was calculated as

$$w_{focused}(\nu) = fc/\nu\pi w_o$$

w is the frequency dependent spot size, f is the focal length of the lens used to focus the beam, and w_o is the spot size of the laser pulse at beam waist[99].

For our reflective imaging system, spot size was calculated experimentally using the knife-edge method and fit to a TEM_{00}Gaussian beam profile. Knife-edge scanning is a popular method of choice for experimentally determining spot size of a Gaussian beam. In this method, beam is swept perpendicular to the knife-edge and the beam intensity is measured. Since the spatial profile of the THz beam is Gaussian, differentiating the signal gives the beam diameter[100]. \

The irradiance function of a Gaussian beam hitting the target at an incidence angle θ with respect to optical axis is described by

$$\frac{E^2(x,y,z,\theta)}{E_0^2} = \frac{\omega_0^2}{\omega^2(z - x\cos\theta)} \exp\left(\frac{-2x^2\sin^2\theta - 2y^2}{\omega^2(z - x\cos\theta)}\right)$$

The beam hits the target at 45° incidence for our system so we substitute $\theta = 45$ and z=0 (location of Gaussian waist) in the above equation.

$$\frac{E^2(x, y, z, \theta)}{E_0^2} = \frac{\omega_0^2}{\omega^2(-x/\sqrt{2})} \exp\left(\frac{-x^2 - 2y^2}{\omega^2(-x/\sqrt{2})}\right)$$

The above expression describes the detectors dependence on electric field.

A metal edge target was translated in a direction perpendicular to the THz beam and reflected power as a function of distance d was monitored.

$$P(d) = \int\limits_{-\infty}^{d} \int\limits_{-\infty}^{\infty} E^2(x, y, z, \theta) \cdot \cos\theta \cdot dydx.$$

y being >> than the spot size permits the integration of the variable resulting in

$$P(d) = \alpha \int\limits_{-\infty}^{d} \frac{1}{\omega(-x/\sqrt{2})} \exp\left(\frac{x^2}{\omega^2(-x/\sqrt{2})}\right) dx$$

where $\alpha = 0.5\eta_o^{-1} E_o^2 \omega_o^2 \sqrt{\Pi}\cos\theta$

The experimental data was fit to the above expression and spot size (10%-90% power points) for 1", 2" and 3" mirrors was calculated.
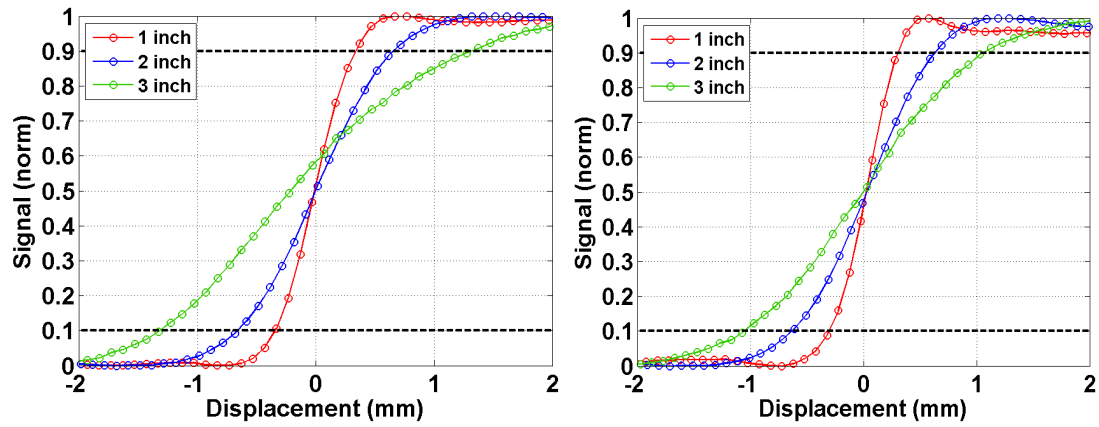
Fig 3.10: Knife edge response of the system for spot size determination in long axis (left) and short axis (right) for 1", 2" and 3" focal length mirrors

Table 3.1: Characteristics of 1", 2" and 3" mirrors

OAP EFL (mm)	w_d (mm)	q (deg)	10%-90% (mm)	DOF (mm)
25.4	9.3	30	0.61 x 0.69	0.8
50.8	36.5	14	1.2 x 1.3	4.0
76.2	62.4	9	2.1 x 2.6	11.7

The depth of focus is evaluated by reconstructing the original Gaussian profile.
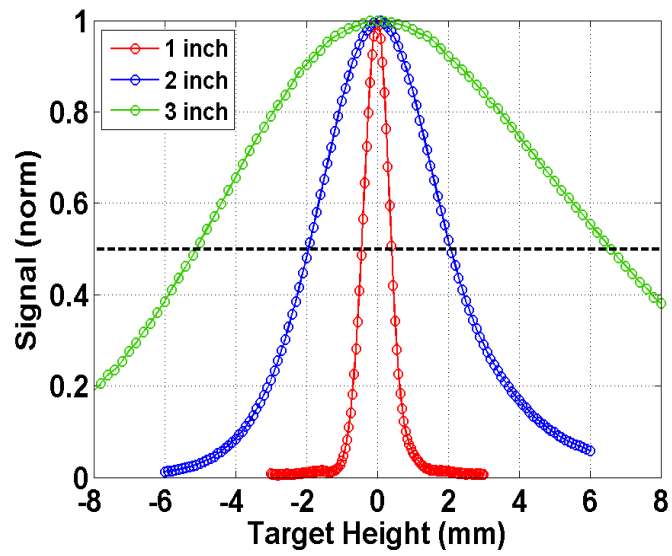
Fig 3.11: Depth of focus evaluation by reconstruction of original profile

3.5.2 Spatial resolution
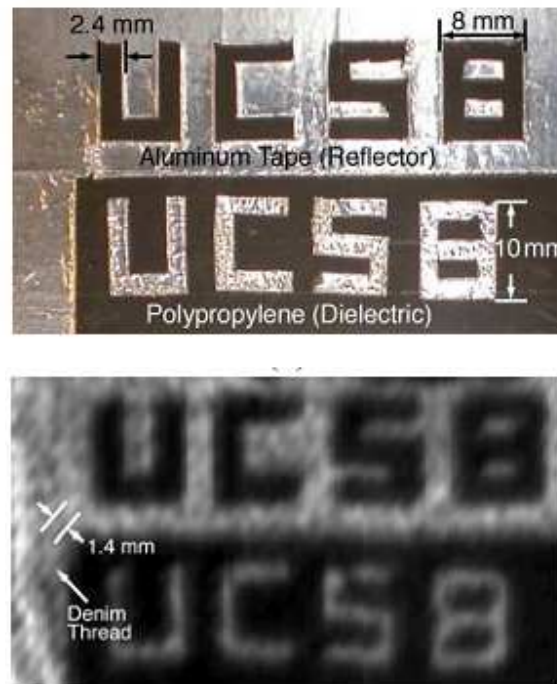
Fig 3.12: Letters U,C,S,B in both metal and dielectric (top) and THz image of the target under a layer of denim

The practical spatial resolution of the system was determined by scanning a metal on dielectric target covered with denim. The target has letters 'U', 'C', 'S', 'B' written both in dielectric and metal. Polypropylene is the dielectric of choice because of its transparency to THz radiation. The target was covered with a 1 mm thick denim cloth having fiber pitch of 1.4 mm. The metal part being highly reflective to THz is easily visualized in the image. The fiber pattern of denim can be resolved in the top part of the THz image. The above image was taken with 2"

57

focal length mirrors having a spot size of 1.2 mm. This experiment affirms that the resolution of our system is around 1.2 mm.

3.5.3 Signal to noise and signal to noise clutter ratios

SNR of the system was estimated by another metal dielectric target. Letters "U','C','S','B' in dielectric were etched in a 2 mm thick copper clad G10 printed circuit board 2.0 cm x 5.5 cm. Each letter covered approximately 0.8 cm x 1.0 cm area. SNR was calculated as ~47 dB for 1" focal length, 42 dB for 2" focal length and 34 for 3" focal length mirrors

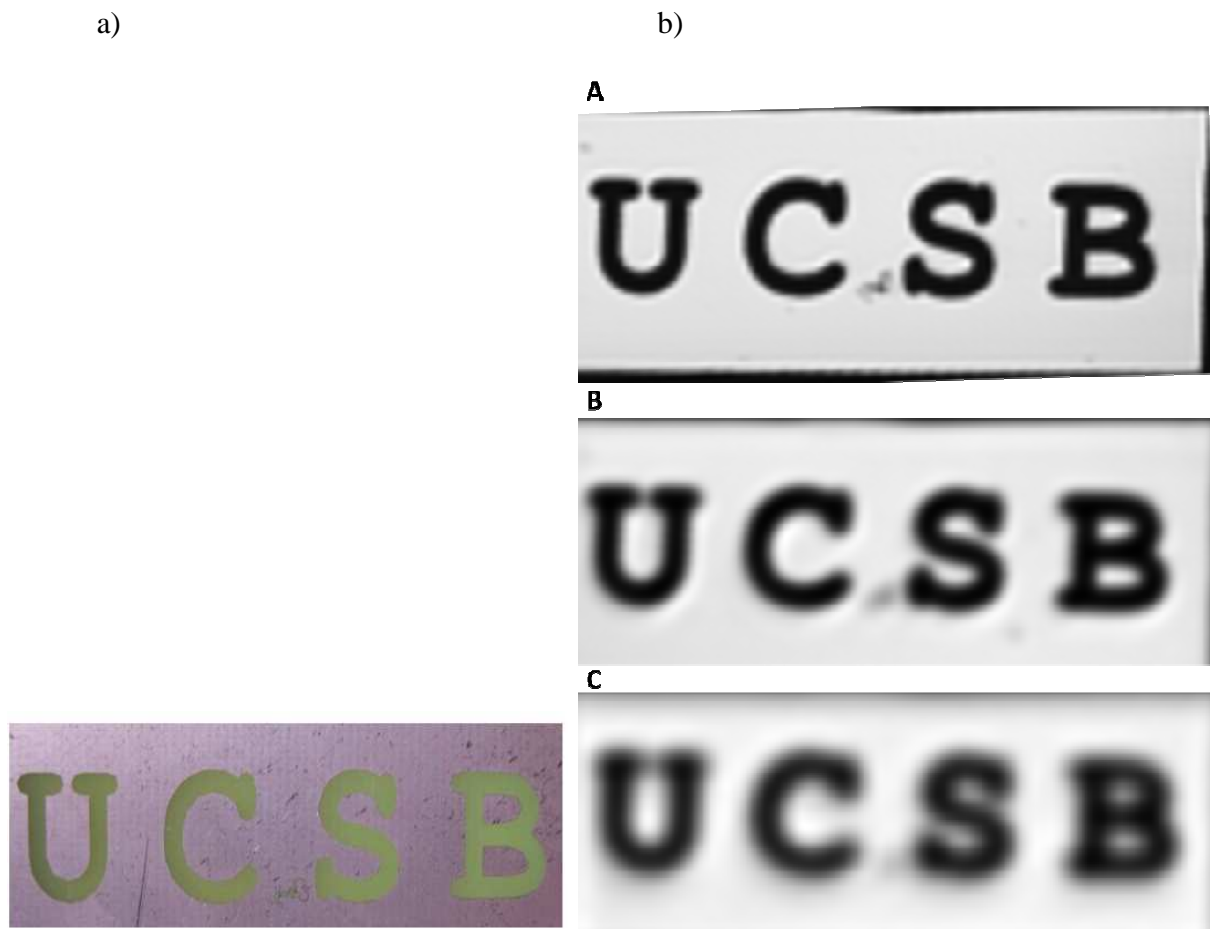a)   b)

Fig 3.13: a) U, C, S, B metal dielectric target, b) UCSB target imaged with A) 1", B) 2" and C) 3" focal length mirrors

Table 3.2: Signal to noise ratio calculations for three mirrors

OAP EFL (mm)	w_d (mm)	~SNR(dB)
25.4	9.3	47
50.8	36.5	42
76.2	62.4	34

Another advantage of imaging with THz waves is their inherent transparency to non polar and non metallic mediums[101]. It has been reported that in the frequency range 100 to 500 GHz, THz waves readily pass through clothing with little attenuation [102]. This has led to the development of active and passive THz imaging systems for security applications, detection of chemical impurities and biological hazards[103].

USCB target was covered with a layer of gauze and scanned with the three focal length mirrors consecutively. The thread pattern was fully resolved in the image taken with   1" focal length mirrors. The image was observed to be devoid of speckle, clutter, and other detrimental effects characteristic of narrow-band imaging systems. The letters were clearly visible in all three images affirming the previous reports.

Signal to noise clutter ratio was calculated for all the three images.
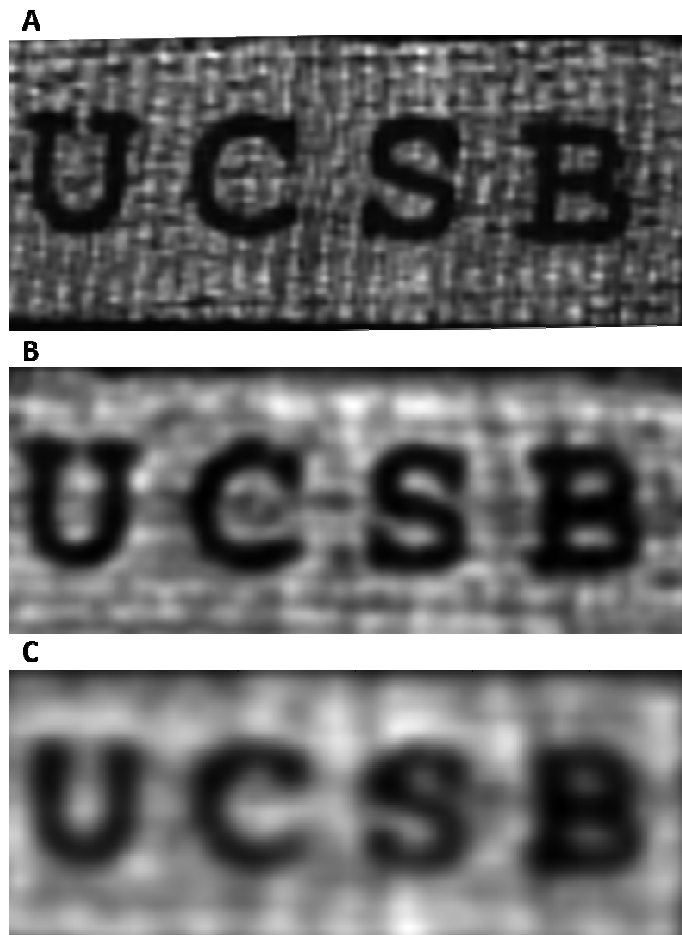
Fig 3.14: UCSB target under layer of gauze imaged with A) 1", B) 2" and C) 3" focal length mirrors

Table 3.3: Signal to noise clutter ratio calculation for the three mirrors

OAP EFL (mm)	w_d (mm)	~SNCR(dB)
25.4	9.3	29
50.8	36.5	25
76.2	62.4	20

This opens up the possible application of THz imaging systems in wound healing monitoring and management. We have explored this prospect by imaging burned porcine skin through layers of gauze. The results of the experiment are discussed in later chapters.

CHAPTER-4: PRELIMINARY BIOLOGICAL TISSUE IMAGING RESULTS

The sensitivity of Reflective THz imaging to surface hydration was explored by imaging biological tissues.

4.1 Deli meats

Our first step towards skin surface imaging was imaging deli meats – salami and prosciutto. Both these deli meats are high in fat content and are composed of lean and fat meat. Fat content of salami is 38-39%[104, 105]and that of prosciutto is about 23%.

a)
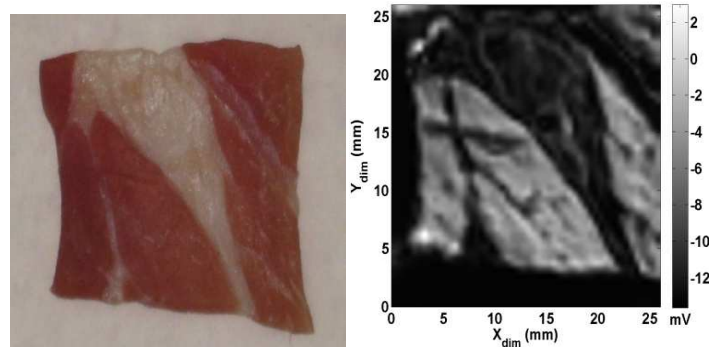
b)

Fig 4.1: (a) Visible pic (left) and THz image of salami (b) Visible pic (left) and THz image of proscuitto

A contrast between muscle and fatty tissue is observed in the THz images of deli meats where lighter areas are representative of muscle and dark areas correspond to adipose tissue. Water content of adipose tissue is around 15%[106] and that of muscle tissue is 76%[107] The response of biological tissues to terahertz frequencies is 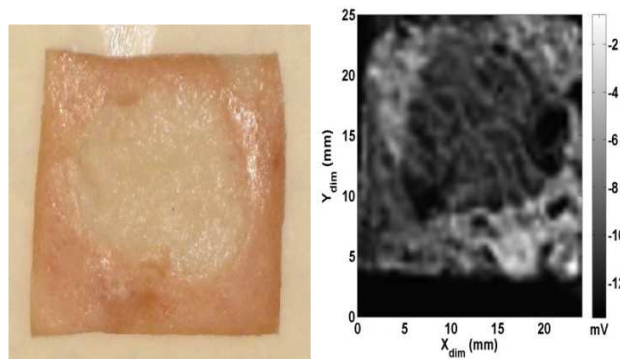largely dominated by water. Higher content of water in muscle hence the regions corresponding to muscle appear lighter than the surrounding fatty areas. Arnone et al (1999) previously found different THz signals from muscle, fat and kidney in pork specimens[16]. At terahertz frequencies, areas of higher water content tend to be more reflective due to a high effective dielectric constant. The difference in water content of muscle and adipose tissue translated to contrast in the THz range allowing visualization of each in deli meat slices. These results indicate that our reflective THz imaging system can distinguish between regions differing in water concentrations. Further the above results can be extrapolated in identifying diseased states in biological tissues resulting from hydration imbalances.

4.2 Tooth

The ability to discern changes in hydration in biological tissues was extended to ex-vivo tooth and cornea specimens.

Adult human beings have 32 permanent teeth that are classified into three categories--- molars, canines and incisors. The structure of a tooth consists of an outer layer of highly mineralized enamel covering dentine followed by cementum and the soft pulp cavity in the center. Dental caries is a disease in which the mineralized layers enamel; dentine and cementum

undergo demineralization and decay leading to pain, infection and tooth loss. According to statistics, dental caries is the most common disease of childhood[108]. About 80% people by the age of 18 years are found to have dental caries. Early detection of caries can be very useful in preventing and treating tooth decay. Visual inspection and x-ray bitewing radiography are most commonly used for detecting caries[109]. Since during early stages of enamel erosion no visible signs are apparent, visual inspection is not an accurate way for identification and quantification of caries. X-ray radiography on the other hand is more sensitive and is also able to detect buried lesions [110-114]. However because of the ionizing nature of x-rays and inability to accurately detect demineralization at primary stages; it is not a preferred method of choice. For evaluating lesion depths and demineralization of enamel, transmission microradiography is considered to be a gold standard[115]. But TMR is suited only for in vitro studies as it requires cutting teeth into thin sections prior to microradiography[116].

Terahertz imaging has shown promising results in the field of dentistry [16, 94, 117-119]. Enamel and dentine have different refractive indices. This difference in refractive indices has been able to generate contrast between enamel and dentine both in reflection and transmission mode [16, 94, 118]. Enamel-dentin junction was identified in 91% of cases in one study[120]. Enamel thickness was accurately calculated which predicted the rate of enamel erosion. Dental caries have been successfully detected in various sections of human teeth[121]. Size and location of dental cavities, composition of tooth, internal pulp cavity and external cavities were visualized using terahertz imaging[120].Another advantage of using THz for in vivo detection of caries and tooth decay is that it is non-ionizing. This gives THz a strong edge over radiography for in vivo detection of demineralization.

A tooth sample investigated was a horizontal cross-section of a molar with a ring of enamel encircling dentin. An island of enamel was present within the dentin as well as two very thin areas of dentin where two pulp horns are close to the imaged surface. The tooth was prepared hydrated and encased in epoxy resin and imaged tooth.
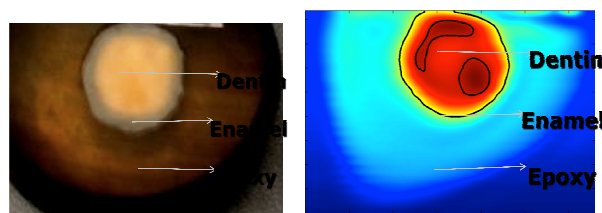

Fig 4.2: (Left) Tooth sample encased in epoxy, and (Right) corresponding THz image

A contrast between enamel and dentin is evident from the imaging results. The yellow region in the 2-D image corresponds to the thin ring of enamel surrounding the dentine. Darker regions within the red area can be mapped to enamel island with thin areas of dentine. Even though the pulp horn shape in the tooth sample is not exactly replicated in the image, enamel and dentine regions in the sample can be differentiated. Studies have shown that THz is able to generate a contrast between enamel and dentine by virtue of difference in refractive indices. Higher THz reflectivity is obtained from enamel (3.1), which is found to have a higher refractive index than dentine (2.6) [14].

The THz image obtained delineates enamel from dentin suggesting that our system can be used to image enamel-dentine junctions. Previously most of THz imaging results have been

65

obtained from dry samples. The tooth sample was hydrated at the time of encasing to account for the moistness of teeth in vivo.

4.3 Cornea

Cornea is the transparent outermost layer of the eye responsible for most of its focusing power. The five layers of cornea are epithelium, bowman's layer, stroma, descements membrane and endothelium. A hydration profile exists in cornea with hydration increasing from the anterior to the posterior region of cornea[122]. Corneal health and function is highly dependent on its hydration state. Normally cornea contains 76.2% water by weight[123]. Maintenance of this constant hydration level is important for corneal transparency[124, 125]. There exists a correlation between corneal hydration and corneal thickness. Corneal edema leads to the opacification of cornea thereby causing loss of vision[126].In case of glaucoma, evaluation of intraocular pressure can help in early diagnosis of the disease and prevent its progression[127]. Corneal hydration is also found to influence the laser ablation rate during refractive surgery[128]. An inverse relationship exists between corneal hydration and tissue ablation. Monitoring of corneal hydration can provide insights into corneal health in cases of trauma, inflammation, dystrophy, diabetes, glaucoma, surgery etc.

Among the various techniques explored for the quantification of corneal thickness, Confocal Raman spectroscopy and optical computed tomography have shown some promise. The disadvantage with Raman spectroscopy is that it uses high doses of green light, which are

beyond the safety thresholds for cornea and retina[129, 130]. OCT on the other hand is not sensitive to slight variations in thickness of cornea[131, 132].

A non-invasive imaging modality that can be used to measure corneal hydration would be very useful in early detection of diseases and feedback during surgery. Due to its non-ionizing nature and acute sensitivity to water, THz imaging may be a useful tool in the evaluation and quantification of corneal hydration.

The following experiment was done to see whether THz imaging could play a role in hydration detection and monitoring in cornea.

Pig eyes were obtained and corneal flaps ~ 130 µm were sliced from the eyes using a microkeratome. Flaps were placed on the polypropylene mount with an Al strip on one side to calibrate the system. The height of stage was adjusted to point of maximum reflectance on the top surface. Setting the maximum as the origin, line scans were taken across the corneal flaps with a step size of 0.5 mm at a bias of 30 V. Each line scan crossed over polypropylene, porcine cornea, and aluminum.
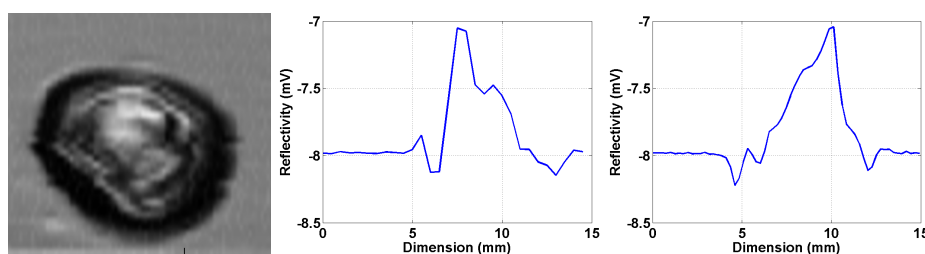

Fig 4.3: (Left) 2-D image of cornea, (Middle) horizontal cut, and (Right) vertical cut through middle of cornea

A radially varying hydration profile is evident from line scans of the corneal flap. The point of maximum reflectance was found to be coincident with the center of cornea. Reflectance decreased from the origin to the edges, suggesting that center of cornea was more hydrated than the edges. The edges were found to have similar reflectivities, indicating symmetry in the corneal structure[133]. Though the results are obtained by forcing a curved corneal flap onto a flat scanning surface they are promising, and in concert with previous experimental observations. We expect improved accuracy with the development of systems for imaging curved surfaces.

CHAPTER 5: SKIN HYDRATION

5.1 Importance of assessing skin hydration

Hydration is a key factor in determining the health of skin tissue. Burns, drug delivery, cosmetics, cancer, and edema are examples where the measurement of hydration levels is important. Skin burns result in loss of water from outer skin layers[134], whereas skin cancers and edema are associated with local increases in hydration of the skin surface[135-137].Diffusion of drugs has been observed to increase through the stratum corneum with increasing hydration[138]. Cutaneous wound repair is also influenced by hydration with water content varying with the stage of repair and the type of wound. Specifically, early acute wound scars are more hydrated than normal skin, while older chronic wounds have been found to be drier[139]. Finally, hydration is critical to the cosmetics industry in testing the efficacy of cosmetics, with many cosmetics intended to prevent and repair skin damage by moisturizing the outer layer [140-142]. Clearly, accurate sensing of hydration levels in the skin, and specifically the stratum corneum, may have broad impact not only to diseased states of the skin, but in monitoring wound healing, trans-dermal drug delivery, planning treatment, and evaluation of cosmetics[2, 4, 143].

The health of skin tissue is maintained by a network of tightly packed cells, namely corneocytes, in the stratum corneum, the 10-40 μm thick outermost layer of skin. Corneocytes

contain within them hygroscopic compounds known as Natural moisturizing factor (NMF) that retain moisture and keep corneocytes hydrated. The intercellular lipid bilayer matrix provides the other line of barrier. The SC lipid composition comprises of ceramides, cholesterol and frees fatty acids and is organized in a series of parallel lamellar membranes with no free water between the lamellae [144-146]. The hydrophobicity and arrangement of lipids not only prevents trans-epidermal water loss but also entry of external substances into skin. A water gradient has been found to exist in the stratum corneum with an inner cell layer that is more hydrated than the outer cell layer. The effectiveness of stratum corneum as a barrier is dependent on its water content, with healthy stratum corneum having water content above 10% weight/weight (w/w)[147, 148]. Below this level, skin loses its flexibility and develops a rough scaly appearance[149].

5.2 Porcine skin model

5.2.1 Similarities to human skin

Porcine skin is one of the closest mimics to human skin. The two share many anatomical similarities. It has been observed that the thickness of human and porcine epidermis is comparable. The stratum corneum of porcine skin like human skin displays sex and age variability. Further the epidermal-dermal ratio of pig skin is close to that in human skin[150].Porcine dermis and human dermis both comprise of a well-defined papillary dermis with delicate collagen fibers and a dense reticular dermis. Even though pig skin has a lower elastic fiber content than human skin, it still ranks highest amongst other mammalian

species[151]. The vasculature – size, orientation and distribution of blood vessels in pig skin is also similar to human skin. Both human and porcine skins bear a lower, a mid-dermal and sub-epidermal vascular plexus[152]. The subcutaneous fat layer is responsible for insulation in both humans and pigs unlike fur in other animal species. The hair follicular pattern arrangement on porcine skin is very similar to human skin in being sparse and progresses through a hair cycle independent of neighboring follicles[150, 151, 153].

Biochemical and functional semblance has been found between porcine and human skin. Oxidative enzyme activity and endogenous epidermal lipase activity is found to be high in porcine epidermis like human epidermis. Surface lipids in porcine skin are composed mainly of triglycerides and free fatty acids[154].Epidermal proliferation and turnover in pigs follows a similar trend as compared to humans. The epidermal turnover is 30 days which is close to 28 days in humans[155]. Pigs have been recognized as excellent human wound healing models because of much physiological likeness between the two. Wound healing is achieved in both through reepithelialization. Antigens like keratins 16 & 10, collagen IV, fibronectin; vimentin and filaggrin have been found in porcine skin. Additionally organ functionality and physiology of humans and pigs is also similar[156]. Based on the above listed similarities, cost, availability and ease of handling porcine skin is a good in vivo and in vitro model for dermatologic and wound healing studies.

5.2.2 Ex-vivo porcine skin model

Ex vivo and in vitro models are generally used for prototypes and preliminary studies. Models are easily available, less expensive and adaptable to experimental conditions. Porcine

skin is a well-established model for human skin and has been used in both in vivo and in vitro settings. A good correlation of biophysical properties like SC barrier function, diffusivity, water permeability, skin impedance has been observed between in vitro porcine skin and in vivo human skin[157, 158].Stratum corneum thickness and lipid composition of human skin and porcine skin is comparable. Porcine and human skins have also been found to have similar water permeabilities [159, 160]. The barrier functionality of a full thickness ex-vivo porcine skin is comparable to in vivo human skin. Ex-vivo porcine skin has been widely used for absorption, penetration and topical distribution studies of pharmaceuticals[157]. The barrier function of skin is compromised in many disorders like eczema, dermatitis, burns etc. For exploring the applicability of THz radiation in imaging these conditions ex vivo porcine skin model is a good choice. It has been demonstrated that ex vivo porcine skin model is vital up to 24 hrs. Besides availability and cost, large sample studies can be carried out under controlled conditions giving experimental consistency and uniformity.

5.3 Current modalities for measuring skin hydration

Electric properties of skin like conductance and capacitance have been shown to vary with the hydration state of skin. Non-invasive measurement of these electrical properties and correlation to water content in the stratum corneum forms the basis of commercial devices that

are being used to determine hydration levels in skin. Corneometer 820-825, a capacitance measuring device; Nova DPM 900, an impedance measuring and Skicon 200, conductance measuring are some of the popular commercial devices in use. All these devices require a probe in contact with the skin and give a hydration value output. Though inexpensive and easy to use, there are disadvantages that have restricted their application as diagnostic tools. Electrical properties of skin are susceptible to changes in skin temperature, presence of other polar molecules, surface roughness, and contact pressure of probes. Therefore electric approaches to quantifying water content are not an absolute measure of hydration and cannot be used in identification of diseased states.

Infrared spectroscopy has shown some promise in non-ionizing and non-contact quantification of skin hydration. Infrared waves are primarily absorbed by water in tissue and this absorption can be linearly correlated to the concentration of water in the tissue. Reflectance spectra of skin are recorded across few wavelength bands and at multiple locations. Mapping these absorption bands across several points gives hydration with respect to location. Studies have reported the feasibility of IR spectroscopy and imaging in determining skin hydration both in vitro and in vivo. In vivo studies have reported on the sensitivity of IR spectroscopic imaging in differentiating between varying hydration states of skin. The hydration states were varied with topical application of a moisturizer and a cleanser. Despite the encouraging results, limited in vivo sample size and effect of electrolytes, temperature, composition and other environmental

factors on water spectrum have hampered the progress of IR in becoming a standard hydration measuring tool.

5.4 Experimental set up

5.4.1 Skin grafts

Porcine skin was obtained (Sierra for Medical Sciences, Whittier, CA) and the subcutaneous tissue layer was removed. Skin specimens of different thickness were cut using the automated dermatomal depth gauged blade (Padgett, Integra Life Sciences Corp., Plainsboro, NJ). The thicknesses of the grafts were as follows: 65 μm, 130 μm, 250 μm, 380 μm, 640 μm and 760 μm. The skin specimens were immediately placed and stored in normal saline to prevent degradation and osmotic intumescence of samples.

Prior to scanning, the specimens were placed onto a polypropylene sample mount, with the outer epidermis of the skin placed face-down on the mount. This arrangement allowed the inner layers of the skin to be scanned directly, with layer depths corresponding to the graft thicknesses. The difference in heights of the skin grafts was accounted by placing the specimens on glass microscopic slides covers of varying thickness so as to bring all the samples at the same level relative to the THz beam.

The specimens were divided into two groups, with each group scanned separately. Group A included specimens of thickness 65 μm, 250 μm and 640 μm, and Group B included the 130 μm, 380 μm and 760 μm samples. 11 line scans each were taken of Group A and Group B. In some cases, duplicate line scans were taken along the same line. Within Group A and Group B, each line scan was taken an average of 15 s apart, with a maximum time of 12 min taken between the first and last line scan to minimize evaporation effects during the experiment.
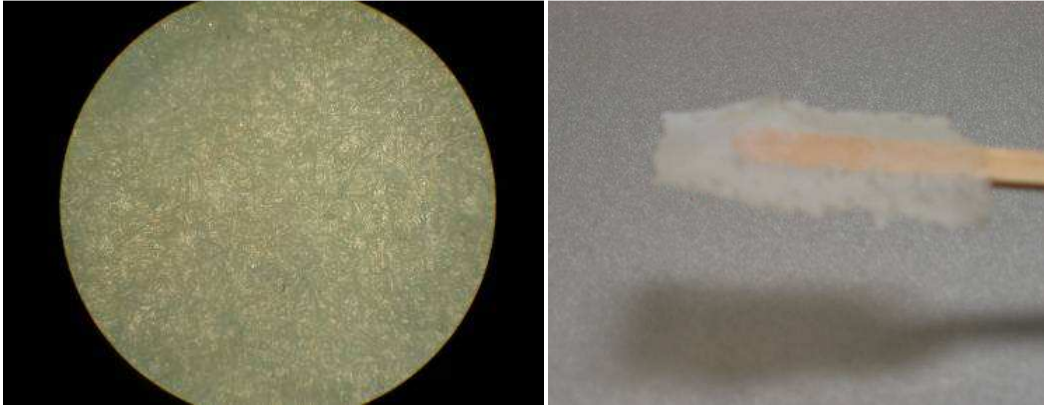
Fig 5.1: Micrograph of bottom side of 65 μm skin graft specimen at 10X magnification (left), and (right) image of the 65 μm sample prior to placement on the sample mount.
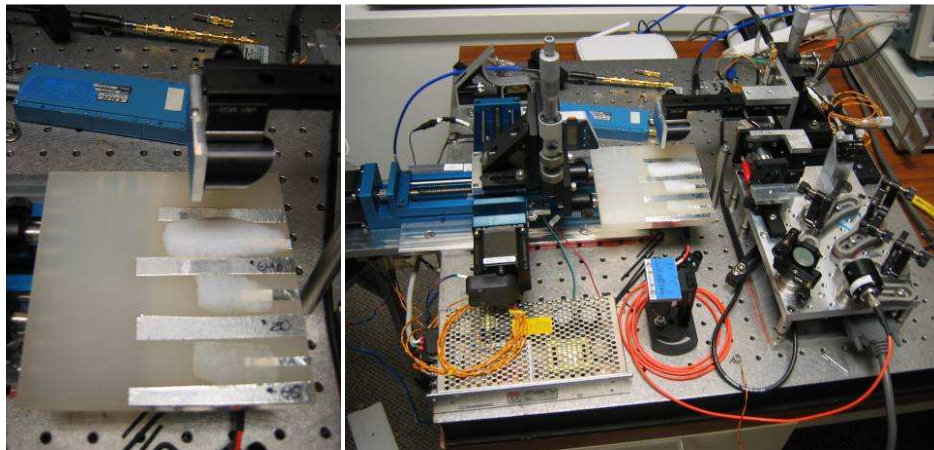

Fig 5.2: Sample mount with Group A skin graft specimens (65 μm, 250 μm, and 640 μm)placed on microscope cover slides and separated by aluminum tape, and (right) THz system during scanning of Group A specimens.

5.4.2 Hydrated and Dehydrated states

Porcine skin, a good mimic of the human skin, was used for the hydration experiments and was acquired from Sierra for Medical Science, Inc.[161] 24 specimens were prepared by sectioning the skin into 2" × 2" pieces and removing the subcutaneous fatty layer from each specimen with a blade. Three different dehydration levels, 3 samples per level, were prepared by

immersion in each of a series of graded alcohol concentrations (30%, 50%, 70%, 90%, 100% alcohol) for 30 min (fully dehydrated), 15 min, and 5 min (i.e. for the fully dehydrated state, samples were immersed in each of the five alcoholic solutions for 30 min each). Five different hydrated levels were prepared by placing the samples in 0.1 M phosphate buffer saline solution (Sigma-Aldrich), for durations of 30 min, 2 hr, 6 hr, and 12 hr (fully hydrated). Unprocessed skin was used as the normal samples. All of the samples of differing hydrations were stored in a refrigerator except during preparation and imaging. Eight representative samples are shown in Fig 5.3
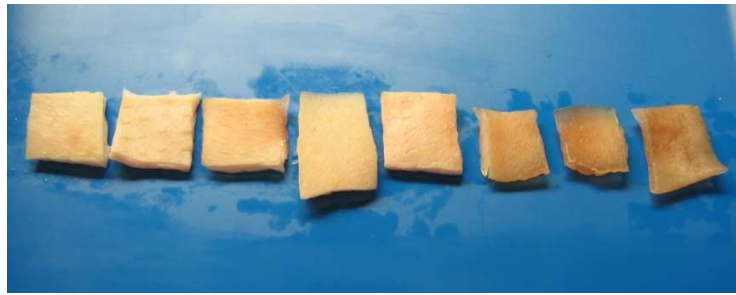
Fig 5.3: Representative porcine skin specimens from each of the eight hydration levels,
with hydration decreasing from left to right.

To measure hydration levels using the THz system, the samples were placed on a flat polypropylene stage that was attached to an XYZ translation stage. The translation stage featured two high-speed screw driver slides (Thomson Mechanical, Inc), allowing XY translation up to 10 cm × 20 cm and a manual Z stage (Zaber Technologies) with up to 6 cm of travel. A piece of aluminum tape was placed in the center of each sample, and the system was calibrated prior to each scan by setting the maximum reflectivity to aluminum and minimum reflectivity to

polypropylene using the Z stage. Multiple line scans (at least 5 per sample) were taken across the specimens, in both the X and Y directions, with each scan crossing over polypropylene, porcine skin, and aluminum. The scan time for each scan was 30 s, and the sampling rate was 75 samples/second. The THz reflectivity was normalized such that 0 referred to full absorption and 1 corresponded to the maximum reflectivity from the metal strips. The average THz reflectivity of each state was calculated by taking a mean of reflectivities for all three samples per hydration level.

A conductance measuring device (Moisture Meter, DermaLab) was used to verify the hydration level of each sample prior to imaging, with skin conductance values expected to increase exponentially with increases in water content[162, 163] Three measurements were taken from each sample by lightly pressing the Moisture Meter probe against the skin samples, and a numerical reading corresponding to electrical conductance were recorded. The device operates at a single frequency (100 kHz) with a measurement range 0-9999 μS (Siemens) and a resolution of 1 μS.

5.5 Results

5.5.1 Skin Grafts:
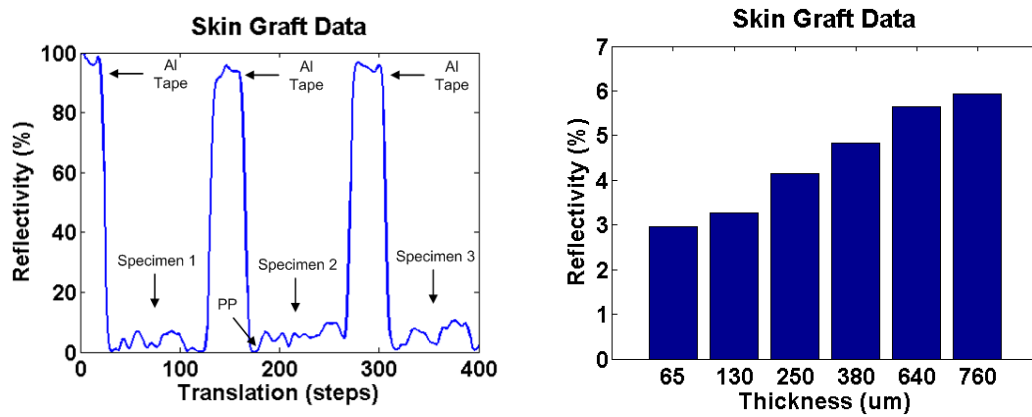
Fig 5.4: Line scans across skin grafts (left), and (right) mean reflectivities plotted against graft thickness

A representative scan of the skin graft specimens is shown in Fig 5.4. The scans were taken with the samples upside-down. Thinner grafts correspond to epidermis while the two thicker samples 640 μm and 760 μm represent dermis. The maximum reflectivity results from the 3 mm wide aluminum tape between samples (Fig.), and the minimum reflectivity results from the 1 mm wide polypropylene surface between the tape and skin graft specimens. The skin graft samples had non-uniform reflectivity primarily due to the variable surface topography, likely due to rete pegs in the subsurface skin layers being unevenly sectioned (Fig. 1a). The average reflectivity for each specimen was plotted in Fig., and showed that the reflectivity increased with increasing skin graft thickness (and skin depth).

78

5.5.2 Hydrated and Dehydrated states:
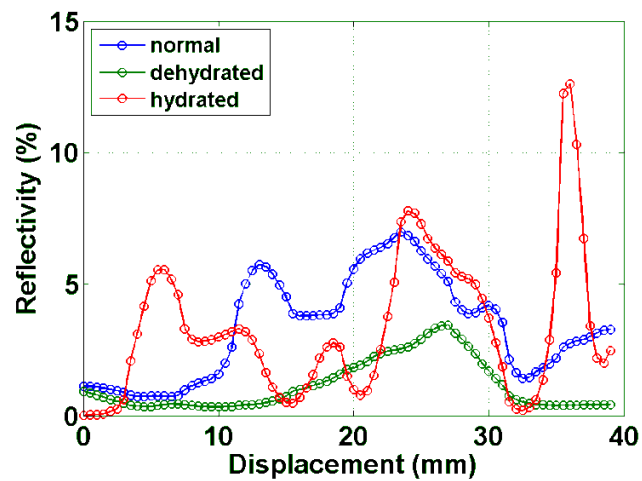
Fig 5.5: Representative line scans from the THz system for a fully dehydrated specimen, a normal specimen, and a fully hydrated specimen

The average reflectivity across three samples for every level was calculated to give a mean reflectivity for each hydration state. Moisture Meter measurements resulted in a range of conductance's between 15 and 17,000 µS. The moisture meter values increased with hydration of skin. On the basis of these conductance measurements, we confirmed the hydration states of our prepared samples.
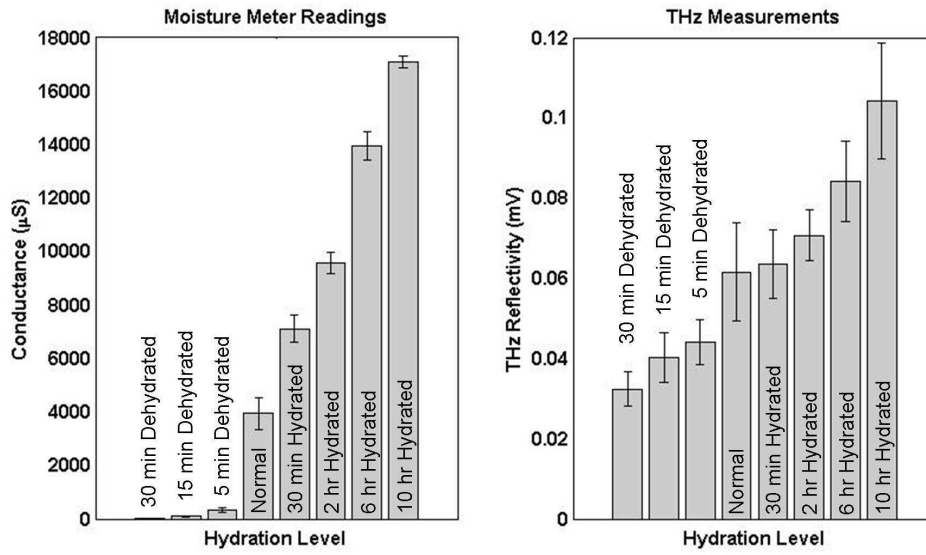
Fig 5.6: Aggregate average terahertz reflectivity (right), with error bars corresponding to the standard deviation.

The aggregate average THz reflectivity for each hydration level is provided in Fig 5.6, with error bars corresponding to the standard deviation of each data set, with an average standard deviation of 3.93 %. A t-test revealed that there was a significant difference (p<0.05) between each combination of hydration levels, with the exception of the normal/30 min hydrated levels (p=0.36).The system accurately measured hydration levels of the skin samples over a relatively small area, with a spot size of 1.2 mm. This results in a much finer sampling of hydration levels over a given area.

5.6 Discussion

The above two hydration sensing experiments demonstrate the sensitivity of our Reflective THz system to changes in water content in skin.In the case of skin grafts, THz reflectivity was found to increase as the thickness of the skin graft increased, despite the uniform

80

height of the samples relative to the THz beam. The exposed skin on the thinner grafts corresponds to upper layers of the epidermis, while thicker grafts represent the dermis. Previous findings have indicated the presence of more water in the deeper layers of skin[164].Under normal conditions, the stratum corneum remains relatively dehydrated while deeper layers are associated with more water. Stratum corneum has a unique lipid composition of ceramides, cholesterol and fatty acids that results in its lower permeability to water, making it relatively less hydrated than the deeper layers[165, 166]. The majority of water in the stratum corneum exists as bound water[167] (energetically bound pool of water) and the water below the stratum corneum's free water (bulk water)[168].Deeper layers of skin like dermis exhibit the free water behavior due to the nature of water association with its constituents. The most visible component of skin in reflective THz imaging is free water[169]. Components like bound water, keratin, lipids, collagen etc have a less frequency dependent effect on THz signal compared with free water. This allows us to sense more reflectivity from deeper layers as opposed to the top layers. Our experiment has corroborated the existing literary findings and shown that we can qualitatively distinguish between layers of skin on the basis of their THz reflectivities.

In the second experiment hydration states of ex vivo skin were artificially altered to exploit the surface hydration sensitivity of the system. The average THz reflectivity was found to increase in accordance with the hydration levels of the specimens.

Stratum corneum can be considered to be a mixture of water and organic molecules like polysaccharides, lipids and proteins. The polarity of water molecules far exceeds the polarity of the other constituents in skin[170].The THz dielectric constant of water is larger than those of the

remaining components. For dry stratum corneum the dielectric constant has been measured to be 2.4[171] and for water it has been measured to be ~ 10+j10[172].The combined sensitivity of THz reflectivity measurements due to changes in bulk water concentration and refractive index ultimately results in a dependence of the net THz reflectivity on hydration state. Therefore, THz imaging involves the direct sensing of water molecules, thereby occluding interference from factors like pH and solute concentration that affect other measurement methods. This allows us to distinguish between ranges of surface hydrations by virtue of their water content alone.

The Moisture Meter, arguably one of the most popular skin hydration measurement devices, in contrast measures the conductance and the dielectric properties of the skin, which in part is dependent on the hydration state[148, 173, 174].The conductance of skin has been found to increase with an increase in moisture content of skin, though the relationship is complicated[148].The low-frequency electrical characteristics (conductance) of skin depend on the mobility of electrons and the concentration of ions in the sample. Specifically, in water, ions create the electron mobility that is necessary for electrical conduction. This is illustrated by the fact that pure water does not conduct. Therefore, the conductivity of skin samples is a function of both the water concentration, and the types and concentration of dissolved ionic compounds. In addition, the conductance measurements are coupled with a model of the dielectric properties of hydrated skin, in order to produce a more accurate reading. Factors such as temperature, salt content, and contact pressure also affect the moisture readings[148, 172]. Moreover, conductance measuring devices seem to be more sensitive to hydrated skin rather than dry skin[148]. Our experimental data has indicated that the Moisture Meter has limited sensitivity in distinguishing

between different dehydration states THz imaging on the other hand is sensitive to the entire range of hydration levels.

The ability of our system to detect variations in hydration states is promising in early detection of diseased skin states. Though the experiments were conducted in vitro, literary evidence suggests a similarity of response behavior between in-vivo and in-vitro skin samples thereby justifying our assumption.[175]The next step would be in exploring a diseased state resulting from or in changes in hydration and evaluating the reflective Terahertz systems capability in detecting such a condition.

CHAPTER-6: EX VIVO SKIN BURN IMAGING

6.1 Ex vivo porcine skin

An ex vivo porcine skin model was used for the initial burn studies. Porcine skin is a well-established model for human skin and has been used in both in vivo and in vitro settings. Ex-vivo porcine skin has been widely used for absorption, penetration and topical distribution studies of pharmaceuticals [157]. The barrier function of skin is compromised in many disorders like eczema, dermatitis, burns etc. For exploring the applicability of THz radiation in imaging these conditions ex vivo porcine skin model is a good choice. It has been demonstrated that ex vivo porcine skin model is vital up to 24 hrs. Besides availability and cost, large sample studies can be carried out under controlled conditions giving experimental consistency and uniformity.

6.2 Experimental design

Fresh porcine abdomen was obtained from Sierra for Medicals (Whittier, CA) and apportioned into 40 mm x 40 mm pieces. The specimens were stored in the refrigerator in a plastic bag for minimum alteration of structure and composition. A polypropylene substrate with a 25 mm x 50 mm grid of 1.6 mm diameter nails was used as a mount for these experiments. The skin specimen was affixed using this arrangement of nails giving a flat imaging plane.

Four temperatures 350° C, 300° C, 250° C & 200° C were explored for inducing burns of varying severities. The rationale for choosing these temperatures was that they produced visible burns of different intensity on ex vivo samples. Previously we have successfully imaged burns inflicted at 315° C with our reflective THz imaging system, hence the choice of this temperature range. A brass brand with a cross protruding from a square base (2 cm x 2cm) was used to inflict the burns after the specimen was mounted on the polypropylene holder. The burnt area along with the surrounding normal area (35 mm x 35 mm) was raster scanned and corresponding images generated using 256 gray levels where lighter shades represent higher reflectivity and darker shades less reflectivity.

The samples were submitted for Histopathological analysis. One slide from each category was digitally scanned with Aperio XT. The depth of tissue damage was measured using the ruler tool in Image Scope.

6.3 Results

The burnt region appeared darker than the surrounding unburnt region allowing for clear visualization of cross in all the images. THz images of porcine skin burns along with their visible pictures and H&E stained sections at 2X from each category are displayed. Some images were discarded due to poor quality of porcine skin giving an unequal sample size across the categories. 14 images for 350° C, 18 for 300° C and 10 each for 250° C & 200° C were analyzed.

a)
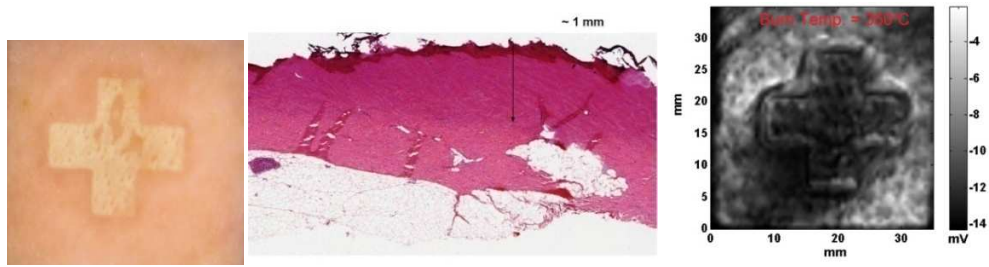
b)
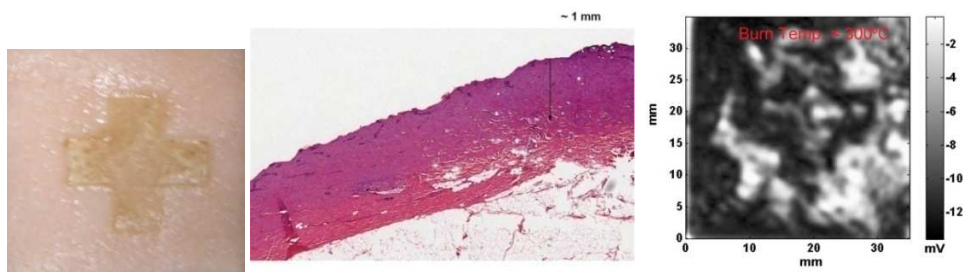
c)
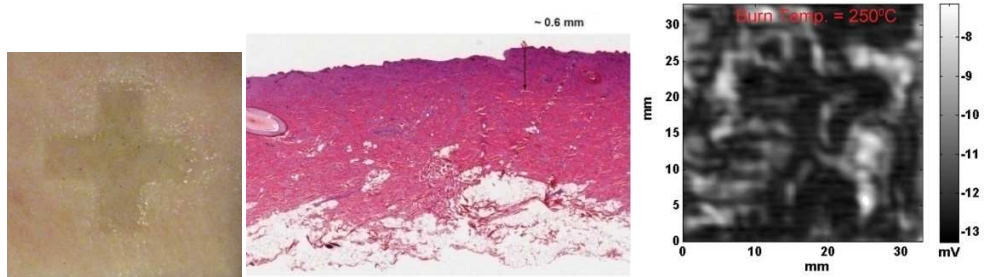
d)
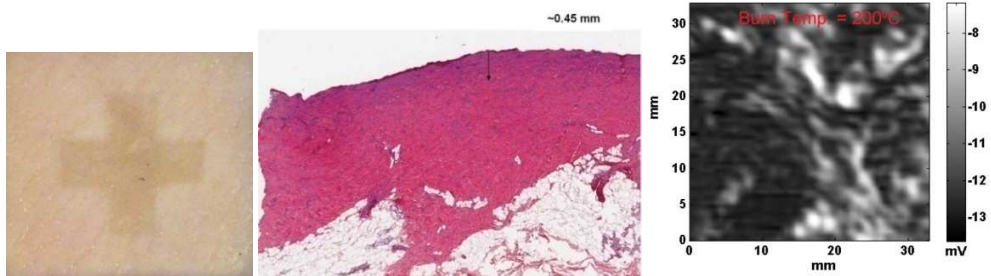
Fig 6.1: Visible pictures (left), H&E stained section (middle) and THz image (right) of a) 350° C, b) 300° C, c) 250° C and d) 200° C

The burnt region appears darker making it clearly distinguishable from the surrounding unburnt area in the THz images. Visually, the contrast between burnt area and normal area is observed to be the highest for 350° C burns in the THz image.

One slide from each category was digitally scanned with Aperio XT. The depth of tissue damage was measured using the ruler tool in Image Scope. This depth was calculated as the vertical distance of magenta/bluish discoloration from the top cutaneous basement membrane. Blue discoloration in H&E stain is a maker for damage to collagen in dermis resulting from thermal insult.

For image analysis, SNR's were compared across the burn categories. Contrast in a THz image is driven by differences in reflectivity's, which can be correlated, directly to SNR of that image. Therefore SNR is a good measure of image quality as these differences are clearer in higher than in lower SNR. Higher SNR would signify better image giving a clear demarcation of the burnt from the normal areas. Based on this logic image quality and comparisons were made on SNR's. SNR was calculated for every image by dividing the square of the difference in the mean reflectivities of burnt and unburnt regions by the square root of their variances. The burnt and unburnt regions were selected at random. Further SNR's were averaged to obtain a mean SNR for every category.

Table 6.1: Results for statistical significance between SNR's of different burn temperatures

Burn Category (C)	N	Mean ± SD	95% Confidence Interval	
			lower bound	upper bound
350°	14	39.208±12.813	31.809	46.606
300°	18	23.615±5.130	21.064	26.166
250°	10	3.117±0.929	2.453	3.782
200°	10	2.419±1.817	1.119	3.719

Mean SNR was found to be highest for the 350°C category followed by 300°C, 250°C & 200°C. Statistical analysis software SPSS was employed for data analysis in both parametric and non-parametric modes. One-way ANOVA, Welch and Brown-Forsythe tests were performed. Because of unequal sample size and variance, post hoc test Tamhane was finally used to determine the statistical relevance of the data.

p values for multiple intergroup comparisons were obtained. The level of significance was set at 0.05 %. p values ≤ 0.05 signify a statistically significant difference in mean SNR's. Significant differences are observed between burn categories except for 250° C and 200° C burn temperatures. This is in accordance with our visual observation.

6.4 Discussion

Porcine skin is an established burn model because of its anatomical and physiological similarities to human skin. Partial thickness and full thickness contact burns have been successfully created in pigs and analyzed ex-vivo for a better understanding of the burn process by researchers previously. For our prototype involving a large sample size, freshly excised porcine skin was an excellent choice because of similar morphology and physiology to human skin, cost considerations, controlled experimental environment, reproducibility and easier translation to in vivo settings.

Barrier function of the topmost layer of skin is disrupted by thermal insult. This leads to evaporative water loss from the surface of the affected area. The degree of damage is dependent on temperature, time & force of contact and the thermal conductivity of the medium. For our experiment all factors except the temperature were kept constant. Therefore level of injury can be expected to increase with increasing temperature. This is confirmed by the histological results. The basal epidermal layer appears to be coagulated in the H&E stained section of 350° C burn. The depth of damage is comparable for the 350° C and 300° C burns and lesser for the other two categories. Since the specimens were ex vivo, viability and necrosis of tissue components ensuing burn cannot be taken into account while predicting the burn degree but from the top surface and longitudinal extent of discoloration, it can be inferred that the 350° C temperature inflicted the most severe burn followed by 300° C, 250° C and 200° C.

The sensitivity of our imaging system to water concentration can be reported in terms of noise equivalent delta water concentration (NEΔWC) metric. A drop in water concentration by

0.054% by volume in the sample is detected by the system with a SNR of unity. It has been recognized that the normal areas surrounding the burnt region do not undergo insensible water loss following burn. The relatively dehydrated burnt region gave reduced THz reflectivity yielding a contrast between the burnt and unburnt area in the specimen as apparent from the THz image. The burns are most distinctly visible with a clear defined boundary for the 350° C category. Corresponding SNR values are found to be highest. Less severe burns gave a low SNR as is seen for the 200° C burns. The burn region boundary seems to be blurry in this case.

An interesting trend seen in most of the images is a relatively bright thin region enveloping the burnt area. Typically a burn wound comprises of three zones: central coagulated zone, zone of stasis and peripheral region of hyperemia. Hyperemic zone results from the loss of epidermis but intact dermis with patent subcapillary plexus and capillary loops. Hemostasis, hemorrhage and hyperemia occur as a result of thermal damage to blood vessels. This area marks the outer boundary of the burnt region. Though these effects are noticeable in living systems with normal circulation but the coagulated epidermal components and intact dermal regions might be responsible for the visibility of this zone in our image. A previous experiment involving imaging burns ex-vivo in rat with photoacoustic microscopy reported the presence of hyperemic bowl in their images. However in vivo imaging is required to confirm this phenomenon.

In conclusion, burns of differing severity on ex-vivo porcine skin were imaged with our reflective THz imaging system. A large sample size was incorporated to test the reproducibility and repeatability of the experiment. The results obtained were reproducible and statistically significant demonstrating the potential of the imaging modality in not only imaging burns but

90

also in distinguishing between burn severities. In clinical settings where diagnosis of burn extent and depth still relies on invasive methods, this could have notable implications. The next step would be to perform similar experiments in vivo to confirm and substantiate the results.

CHAPTER-7: *IN VIVO* BURN IMAGING

7.1 *In vivo* rat model

In vitro and ex vivo models are good for preliminary studies but are unable to replicate the physiological and metabolic response, hence have limited applications. Various animal models have been explored for skin burn studies. The ideal animal model should able to reproduce the physiopathological response to burn injury, be easily available, relatively inexpensive and easily manageable. Although pig skin is the closest to human skin, because of the cost factor and difficulty in anesthetizing the species is generally not the first choice. Experimental rat is found to be a good model for burns studies[176]. The two most commonly used strains for research purposes are – Wistar and Sprague Dawley. Both the strains are albino. Rats fall under the category of loose skinned animals whereby healing occurs through wound contraction. This does not parallel the wound healing process in human skin. However the immediate response following thermal injury - cell death, inflammation and ischemia has been found to occur in rodent models. Rodents have been found to respond to thermal trauma with the secretion of various proinflammatory and anti-inflammatory cytokines that mimic the inflammatory postburn response in humans. Hyper metabolism caused by extensive burns in rats follows a time course similar to that in humans. Vascular and microcirculatory changes that are indicative of tissue damage and healing have been visualized in rat models previously. Because

of these similarities rats have been extensively used for studying and visualizing both the immediate and long-term response to thermal injury.

Rats are considered suitable for metabolic research and a great deal of literary knowledge on their genetic makeup and immune response exists[177]. Further rats are large enough to induce burns either on dorsum or abdomen. Male rats have been more frequently used than female rats for research and majority studies use weight range 250 – 300 g; age newborn to 36 months. There is no physiological preference for the gender but male rats are cheaper than female rats in general hence are more widely used. Young rats are preferred over older ones because they have better dermal perfusion and sensory nerve function.

Two most common thermal burns are scald and contact burns. Scald burns are induced by dipping an exposed area of the animal in hot water (over 90° C) while contact with hot conductive material produces contact burns. The burn severity depends on time of exposure in both cases. Lead, copper, aluminum and brass because of high heat capacity are the materials of choice for inducing contact burns. Studies have reported heating the materials by immersing in hot water, heating on a hotplate or through resistive heating[178]. Regas et al report a "comb" burn injury model for studying vascular changes following burn injury in rats. A contact burn was inflicted by pressing a comb shaped brass brand heated in water for 20 seconds on the backs of Sprague Dawley rats. The weight of the probe provided the contact pressure required in inducing uniform full thickness burns. The burn wound was in the shape of a comb with four full thickness 10 x 19 mm rectangular rows separated by 5 mm bands of 5 x 19 mm uninjured skin. The interspaces corresponded to the zones of stasis interspaced between burned regions. The

93

model allowed for the fabrication of full thickness burn zones with uniform zones of stasis in between. Vascular changes in the zone of stasis ensuing injury, which are indicative of ischemia and wound progression, were visualized.

A similar protocol was followed for induction of partial thickness and full thickness burns in Sprague Dawley rats for our experiments.

7.2 Initial feasibility study: Experimental Design

7.2.1 Animals

Male Sprague Dawley rats age 4 to 5 months weighing 200-300 gm, were selected for the in vivo study. Animals were procured from Harlan laboratories, Hayward CA and allowed to acclimatize for a week before the experiment. The animals were housed in the UCLA vivarium and fed food and water ad libidum.

The animal was prepared for the surgery as per Animal Research committee, UCLA requirements. A flat ~ 4 cm x 4 cm area on the lower abdomen was selected and shaved with electric clippers to reduce skin irritation. Three alternating preparations of germicidal scrub and rinse were performed - scrubbing with a povidone-iodine scrub (e.g., Betadine®, Nolvasan®), from the center of the site toward the periphery followed by rinsing with 70% alcohol. Prior to burning, the animal was subcutaneously injected with buprenorphine (an analgesic) (0.05 mg/kg). The rat was then placed on its back on a Plexiglas mount and its arms and legs secured

to the Plexiglas with electrical tape. A nose cone connected to the 1.5% isofluorane induction was placed over the snout and left for the remainder of the experiment.

7.2.2 Rat mount

A Plexiglass stage 0.5 "thick 5" x 10" was used for holding the rat during the experiment. Four ¼-20 counterbore holes were drilled in the center of the mount for affixing to Lab jack (ThorLabs L200). The stage height was adjusted manually using the Lab Jack. Mylar window was suspended from a dovetail rail attached to one of the edges of the mount. A water circulation pad was placed on top of the mount for keeping the rat warm during the experiment. The pad was connected to the water circulation pump for maintaining the temperatureat37° C. The rat was placed on its back with arms and legs stretched out and restrained with surgical tape.
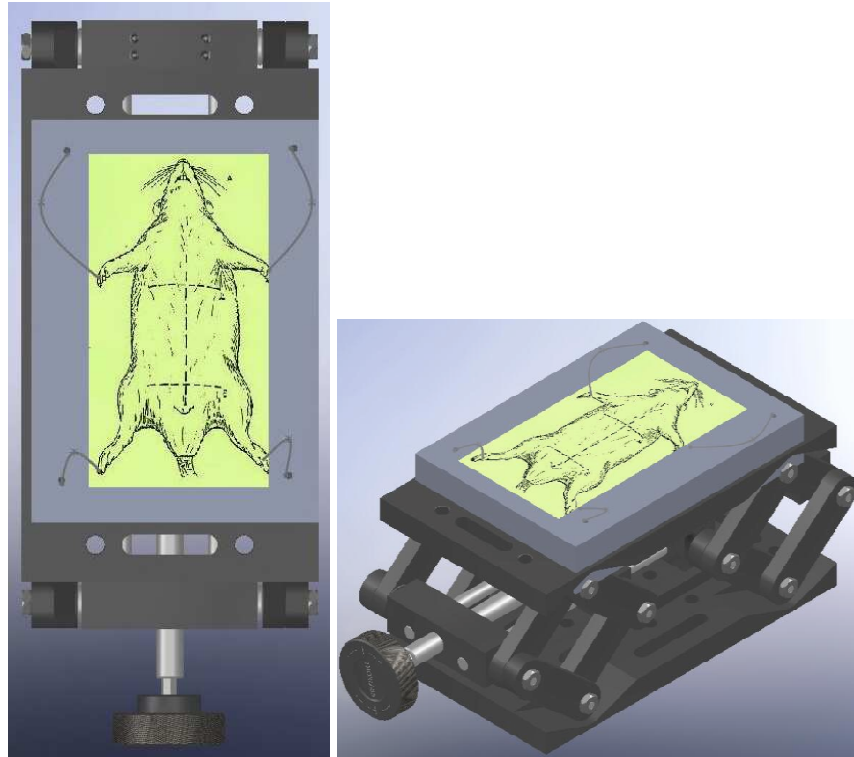
Fig 7.1: Schematic of rat placed on the mount on the Labjack.

Gas anesthetic isofluorane was used for anesthetizing the rat. Advantages over injectable agents like minimal animal handling, large margin of safety, ease of anesthetic control, low cost of anesthetic agent, no controlled drugs, and quick recovery times make it the anesthetic of choice.

A nose cone was constructed by cutting the thumb partition off a latex glove. Two criss cross slits were made for creating an opening and the other end was fixed onto the tube attached to the anesthesia machine. The opening was hooked beneath the incisors and masked over the snout.

Fig 7.2 Nose cone made from a glove

The anesthesia system was set up and checked for adequate supply of oxygen and isofluorane. System was set to flow to nose cone. The flowmeter was turned between 100 – 200 ml/min. The vaporizer was set between 2 – 3 % initially and reduced to 1.5% for the remainder of the experiment.

7.2.3 Burn brand and induction

A brass brand in the shape of a cross protruding from a rectangular base (20 mm x 20 mm x 20 mm) was used for inducing burns on rat's abdomen. Each arm measured ~20 mm.

Fig 7.3 'Cross shaped' brass brand used for burn induction

An 8-32 hole was drilled in the back of the brand and was used to screw the brand to an Aluminum rod (` in). The brand was heated up to the desired temperature using a ceramic hotplate (Fischer scientific). The temperature of the brand was checked using an industrial thermometer.

7.2.4 Partial and full thickness burn induction

Burn severity depends on temperature, pressure and time of contact. For induction of partial thickness and full thickness burns, pressure and time were kept constant while the temperature was varied. A temperature of 180° C was found requisite to induce partial thickness burns and 220° C for full thickness burns.

A flat ~ 4 cm x 4 cm area on the lower abdomen was selected and shaved with electric clippers to reduce skin irritation. The brand was gently pressed against the abdomen for 6 to 8 seconds with contact being the only pressure applied.

7.2.5 Mylar windows

In order to reduce signal interference from surface topology and curvature, the imaging area was covered with a Mylar window. Mylar is thick enough to flatten the field of view but still sufficiently thin to conform to the skin sample roughness. 12.7 μm Mylar/PET film was stretched using linear micrometer stages. 2" type 316 stainless steel washers were laced with a thin layer of super glue and placed on the Mylar film and left to dry overnight. The steel washer was fitted in a fixed optic mount with the Mylar film side down. The window was mounted onto

a dove tail rail carrier through an 8-32 screw. The assembly was snapped on a 3 "rail and tightened at the desired distance off the imaging head using locking thumbscrew.

Fig 7.4 Mylar window placed flush against the animal's abdomen

7.3 8 hr terminal study

Two burn severities were imaged over a span of 8 hours. Images were taken every 15 min for the first hour and every 30 min for the next 7 hours. At the end of 8 hours the rat was euthanized.

Fig 7.5 (Left) Shaved control area on the abdomen and (right) appearance of skin after burning at 180⁰ C

Images were generated in MATLAB in 256 gray and color scale. The resolution was increased by upsampling the images by a factor of 8. Minimum and maximum values were specified and linearly mapped to the 256 colormap for image enhancement.

Pseudo code

Load all image files(*load([curr_dir '\data\' fn])*)

For each image

    Upsample by a factor of 8

    colormap jet (256) or color (256)(*colormap jet(256);else;colormap gray(256)*))

    Set lower threshold at -12.0 (ca_min =-12)and upper to -8.0 (ca_max=-8)

    Generate image (*imagesc*)

    Label image using X and resave in PNG format
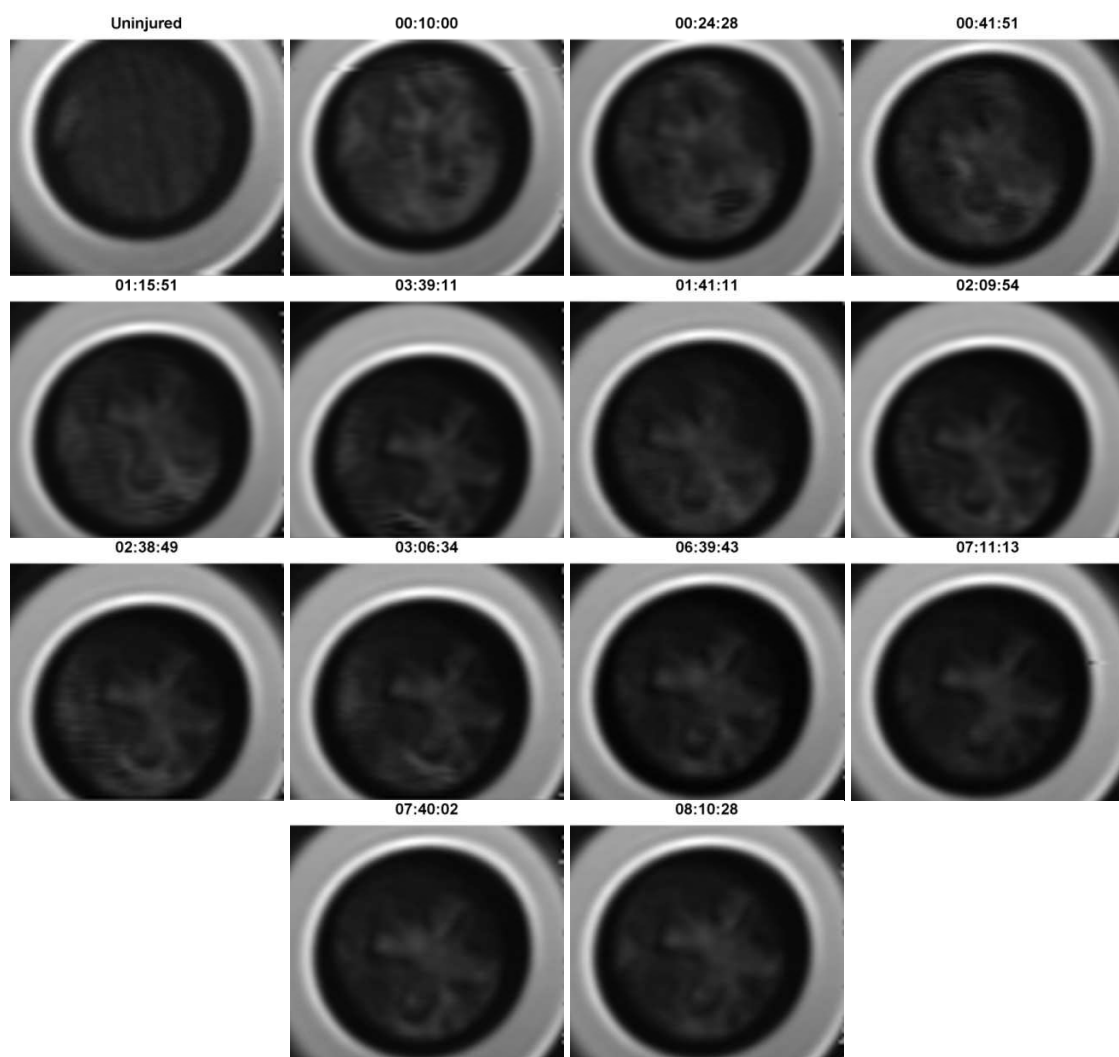
Fig 7.6 Raw THz images showing the evolution of burn induced at 180⁰ C over 8 hours
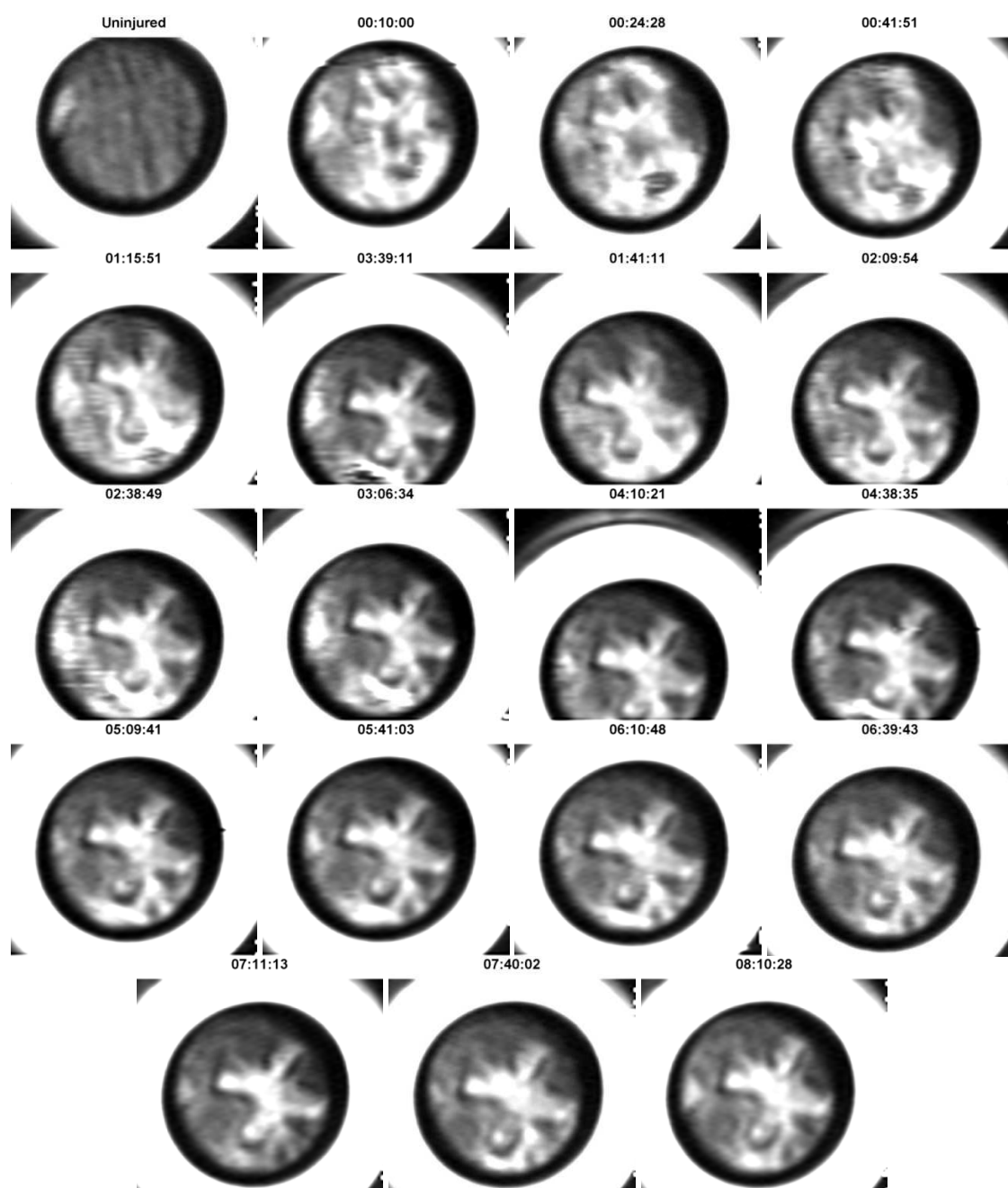
Fig 7.7 THz images showing the evolution of burn induced at 180⁰ C over 8 hours in grayscale

102
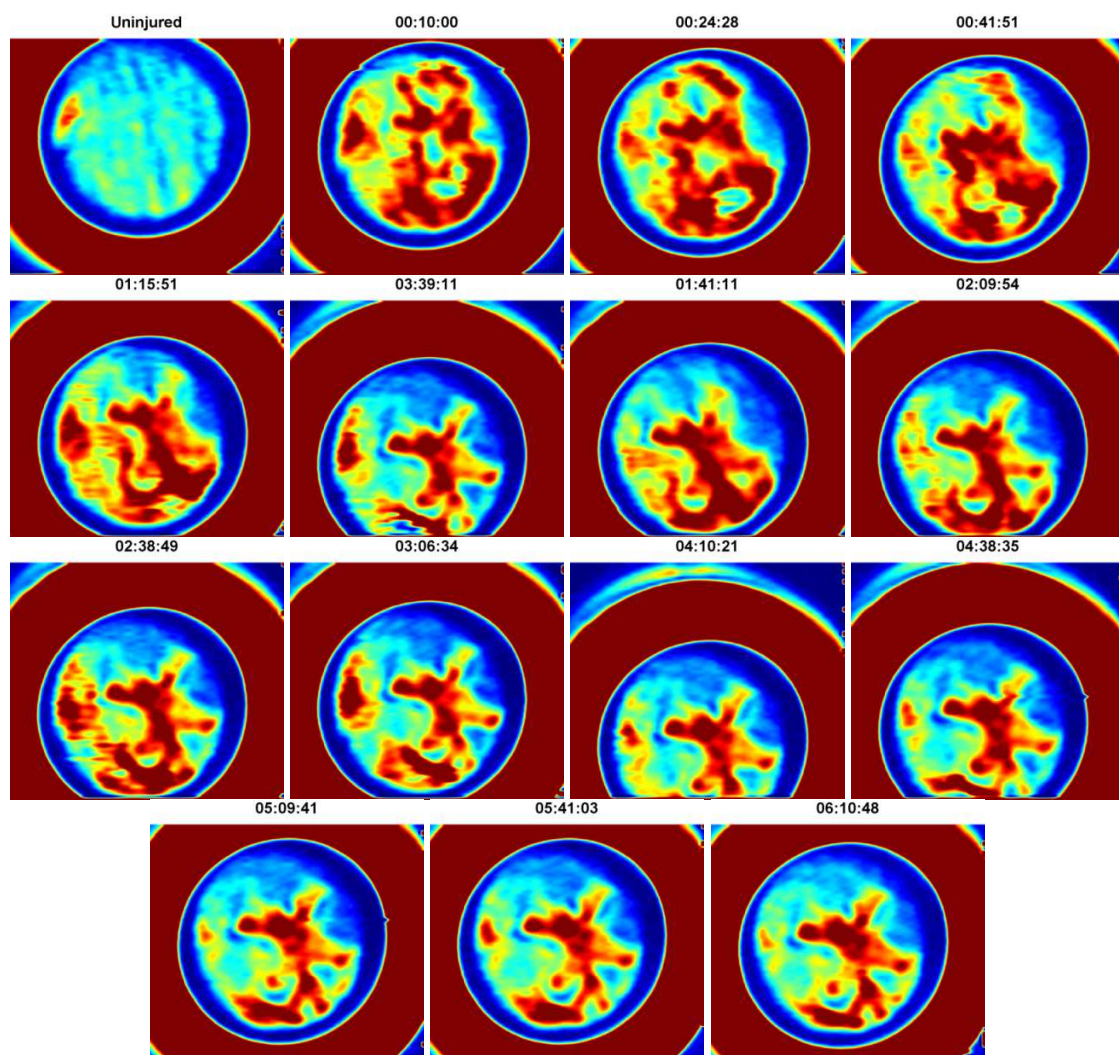
Fig 7.8 THz images showing the evolution of burn induced at 180⁰ C over 8 hours in color
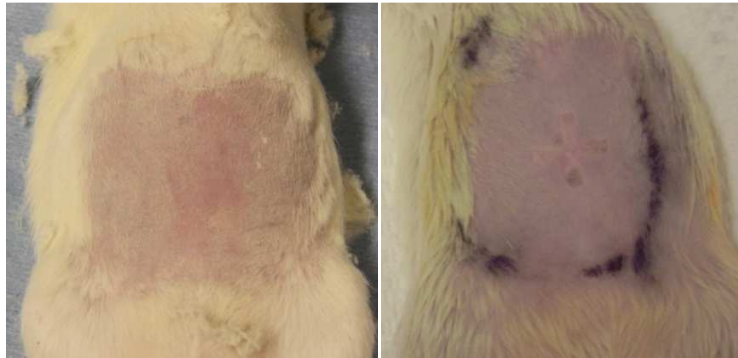
Fig 7.9 (Left) Shaved control area on the abdomen and (right) appearance of skin after burning at 220⁰ C
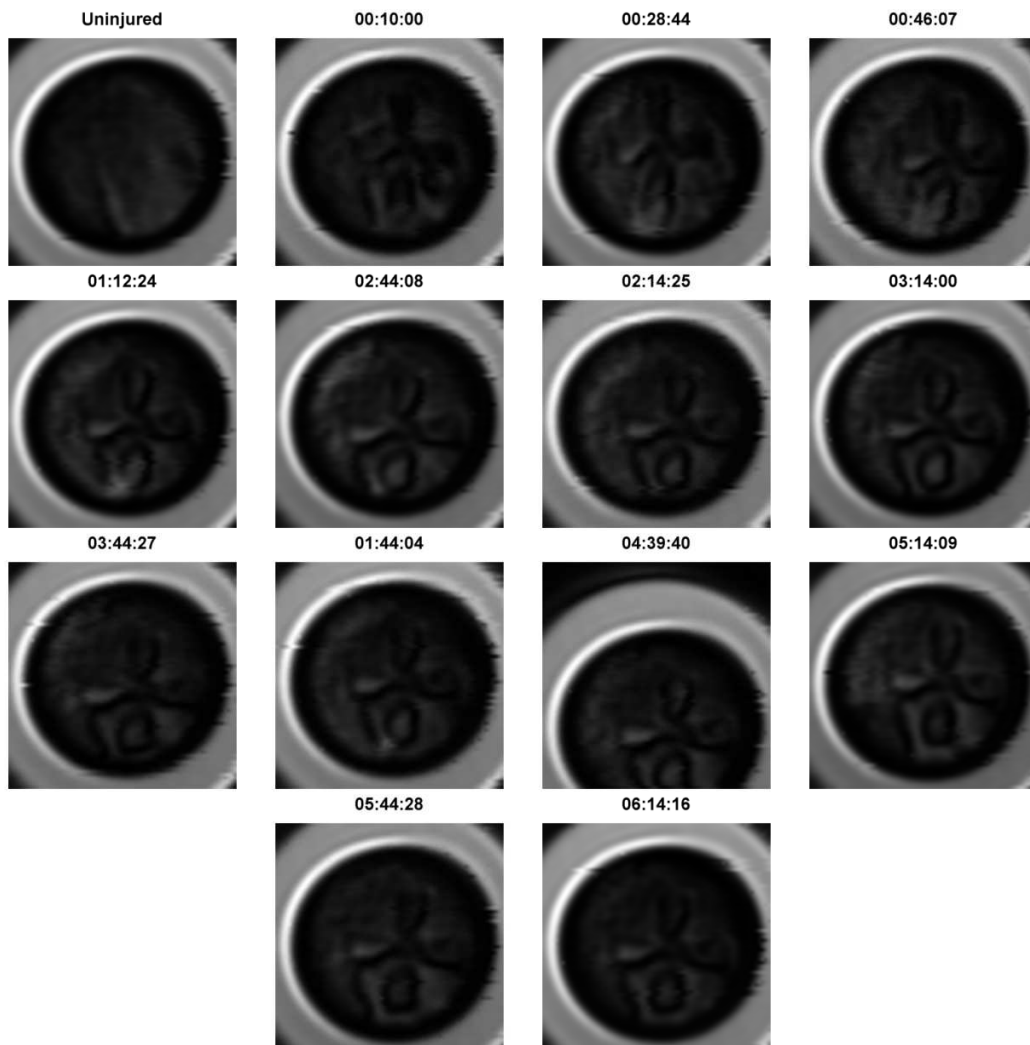
Fig 7.10 Raw THz images showing the evolution of burn induced at 220⁰ C over 8 hours

Uninjured	00:10:00	00:28:44	00:46:07
01:12:24	02:44:08	02:14:25	03:14:00
03:44:27	01:44:04	04:39:40	05:14:09
05:44:28	06:14:16		
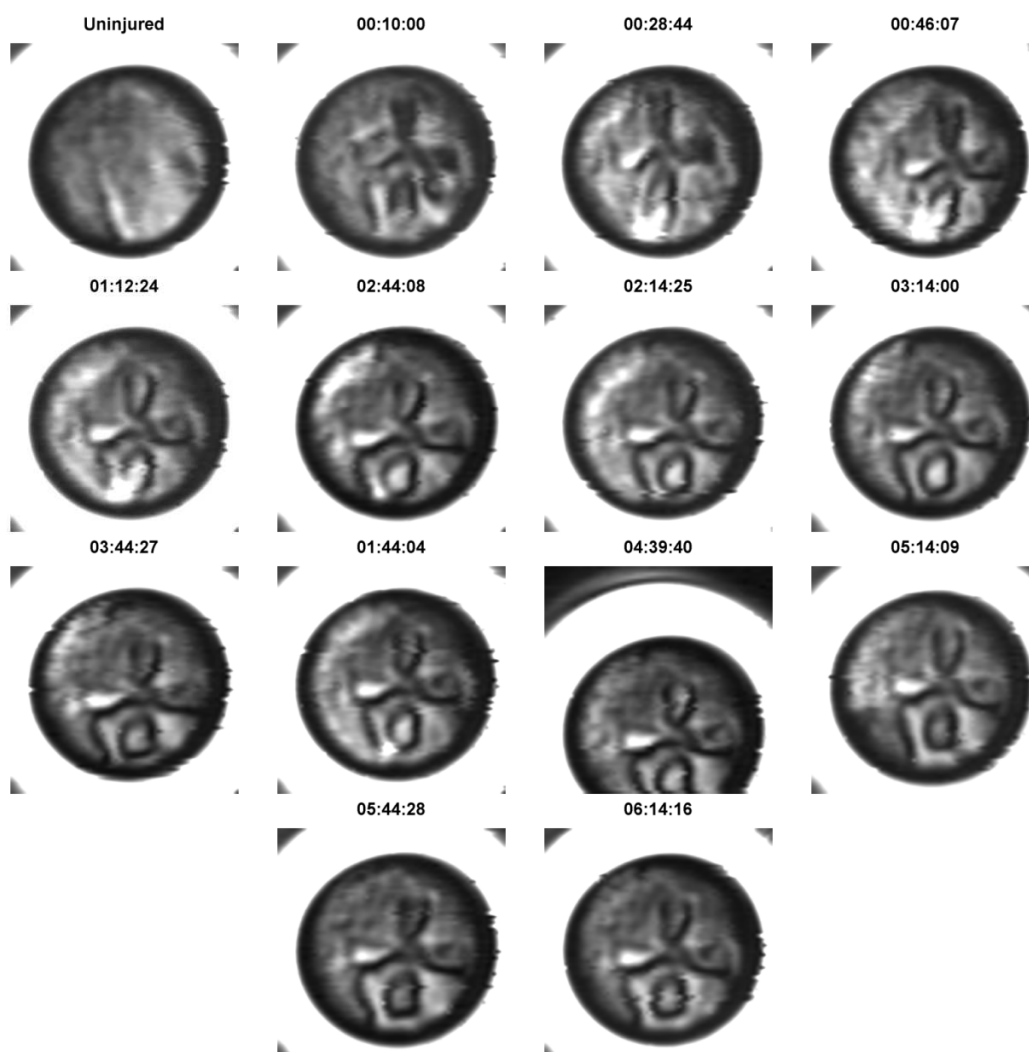
Fig 7.11 THz images showing the evolution of burn induced at 220^{0} C over 8 hours in grayscale
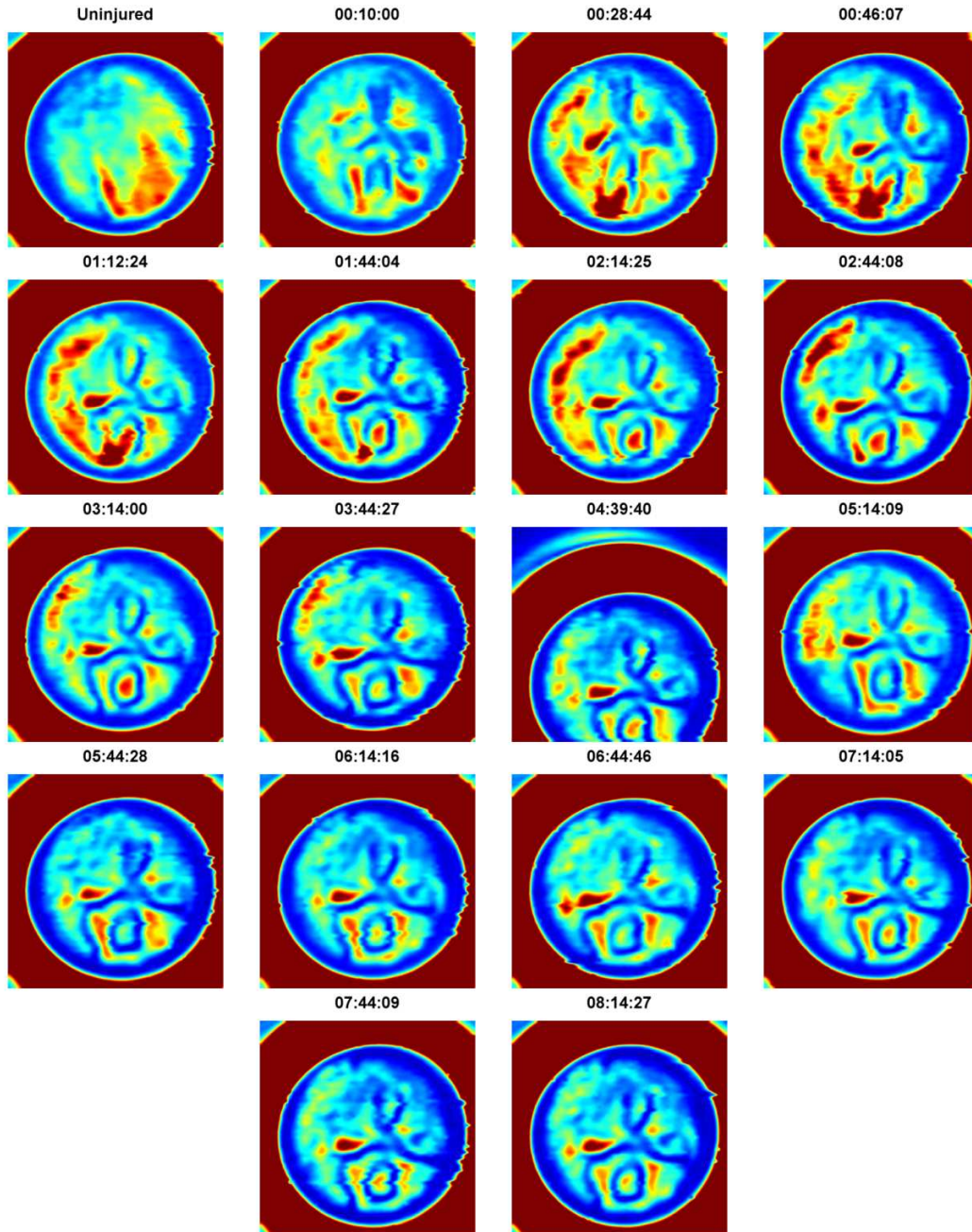
Fig 7.12 THz images showing the evolution of burn induced at 220⁰ C over 8 hours in color

Terahertz images were taken for a period of 7 hours. In the case of the lower temperature we see an immediate rush of fluid to the site of injury resulting in both the burn and surrounding area to becoming edematous. For the images acquired in the first hour ensuing burn, the entire field of view appears reflective indicating an acute influx of water throughout the region. At 1 hour postburn, the response has organized, and the zone of increased water concentration begins to localize to the region where the brand contacted the skin. Finally, after 7 hours the edema has localized completely to the brand contact area and the surrounding skin has returned to normal, non-burned reflectivity. Additionally a dark, low reflectivity ring of tissue is seen along the periphery of the hyperhydrated brand contact area.

A different response is seen in case of the higher temperature burn. The brand shape is discernible as early as the post burn THz image. The burn appears relatively more dehydrated than the surrounding normal tissue. It is plausible that greater thermal insult severed blood vessels blocking the inrush of edema to the site of injury. A dark ring of tissue enveloping the brand area is also visualized in the THz images of the higher temperature burn. The dark region corresponding to hypohydrated zone appears darker and wider in case of higher temperature burn.

Burn wound pathophysiology is divided into three concentric regions [134]. These are the zones of coagulation, stasis, and hyperemia. The zone of coagulation (hyper-perfused) is at the center of the burn and contains irreversibly damaged cells and denatured protein. The zone of stasis surrounds the zone of coagulation and contains hypo-perfused tissue. The zone of hyperemia forms the outer ring and is characterized by edematous, hyper-perfused tissues. Burn wound progression is the process by which potentially salvageable tissues in the zones of stasis

and hyperemia necrose, resulting in larger and deeper burns than were present upon initial presentation [127], [134].Concomitant with the appearance of these three zones are large fluid shifts both locally and systemically. Investigations into these fluid shifts have concluded that local water concentration can increase by as much as 80% within 10minutes of injury, and that this response is proportional to the depth of injury [135],[136].Given the large shifts in location and intensity of the observed THz reflectivity, we believe that we are observing the formation and evolution of the zone of coagulation (high reflectivity center of the burn) and zone of stasis (ring of low reflecting tissue surrounding the highly reflective center).

7.4 3-day survival studies

The first set of feasibility studies did not involve histopathological confirmation of burn severity. In order to test the repeatability of the above experiment another similar experiment was performed. The brand, burn temperature and time of contact were kept same. Burn wounds are in a dynamic state with burn depth and severity consolidating in about 72 hrs. Necrosis in zone of stasis, oxidative damage and cytokine mediated response are the main factors that confound early histopathologic assessment of burn severity. It was therefore decided to keep the animals alive for 3 days for a meaningful histological evaluation.

The rat was scanned every 15 min for the first hour and every half an hour for the remaining 11 hours. After continuous scanning for 12 hours, the animal was woken and put in a cage with care fresh bedding. Follow up scans were taken every 12 hours for a period of 3 days. The animal was sacrificed at the end of three days, the skin resected and submitted for histology.
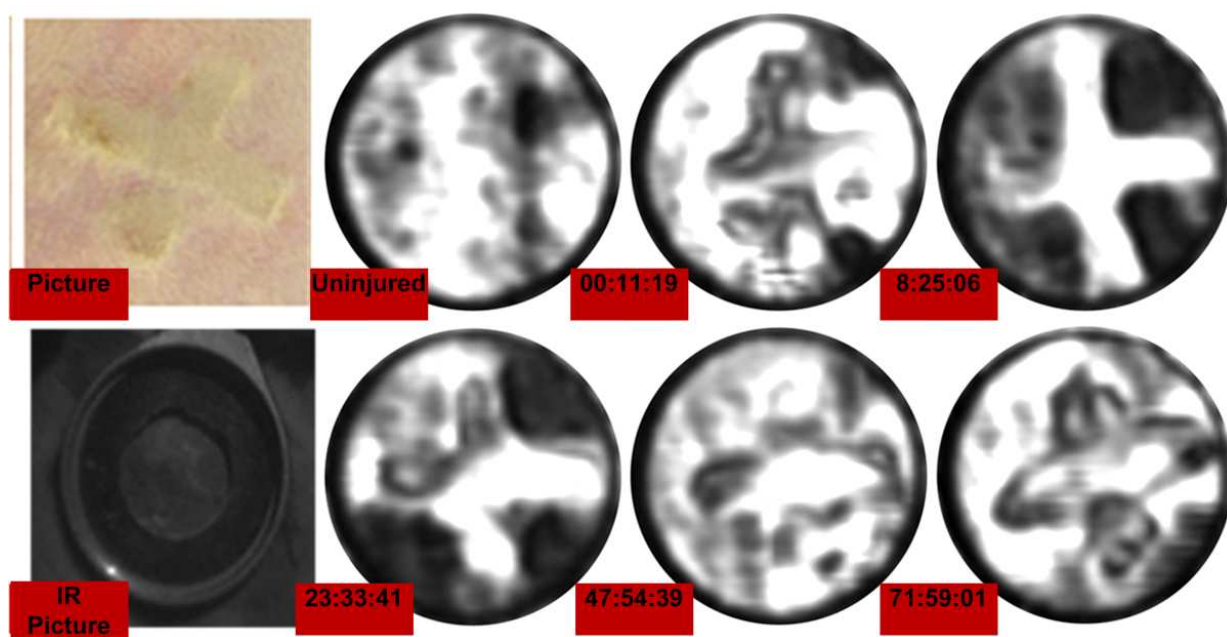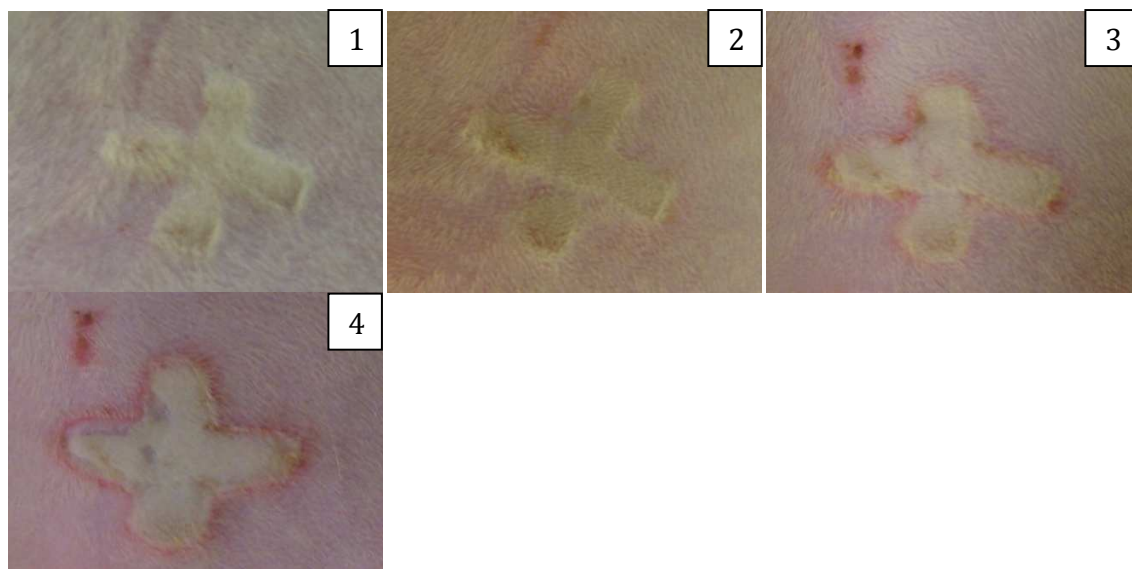
Fig 7.13 Visible pictures of a partial thickness burn on day 1, 2 & 3 and THz images depicting burn wound evolution over 72 hrs.
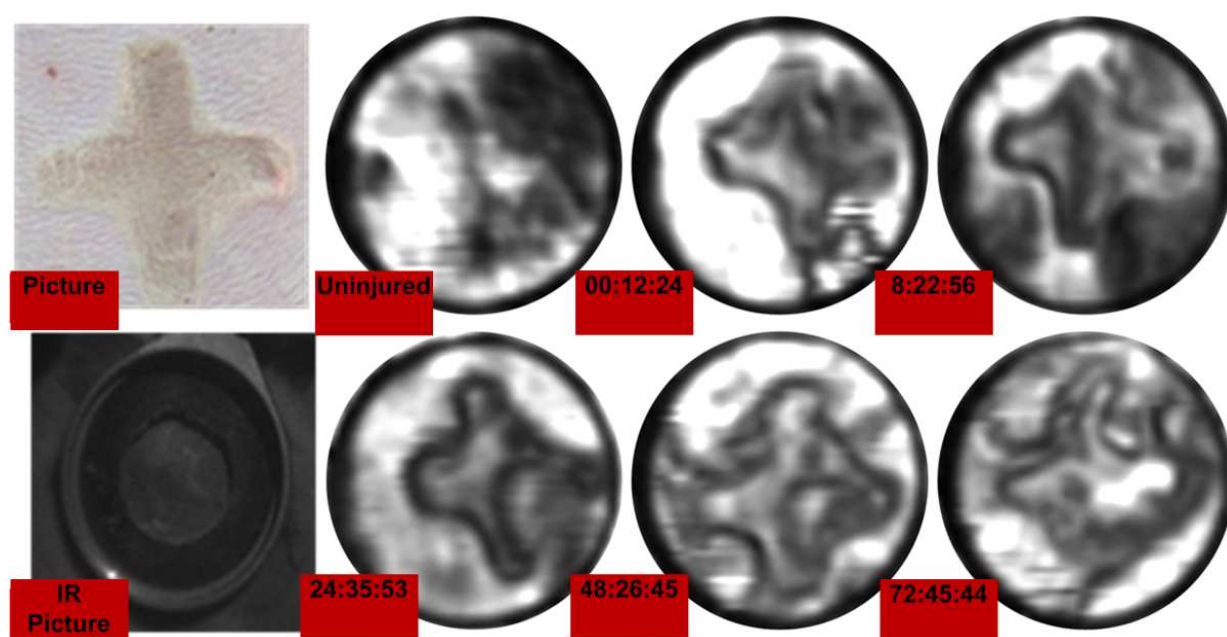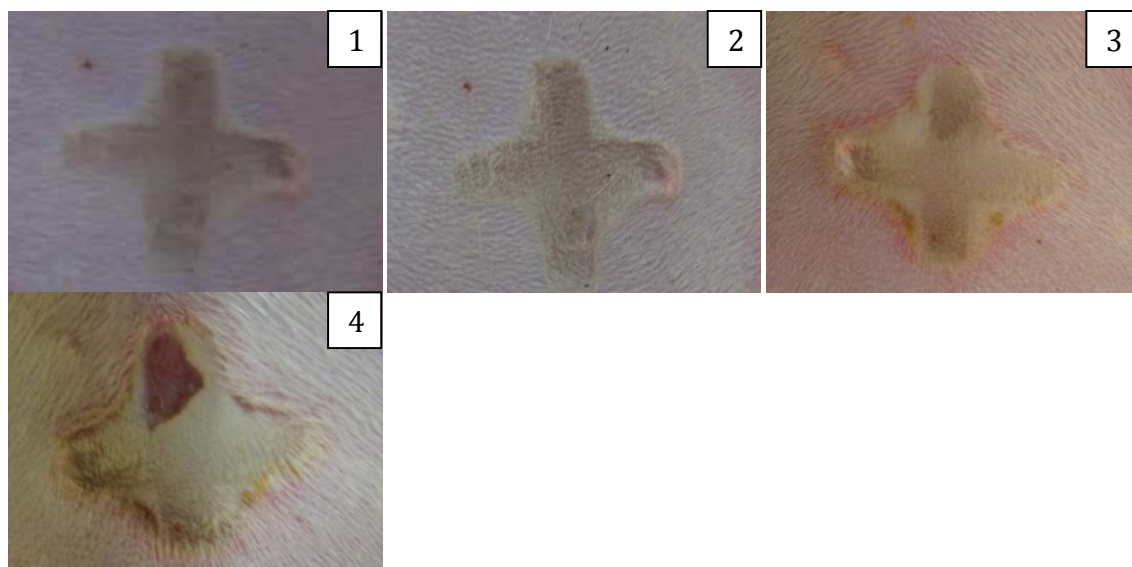
Fig 7.14 Visible pictures of a full thickness burn on day 1, 2 & 3 and THz images depicting burn wound evolution over 72 hrs.

Histology was used for burn depth assessment. A cut from one of the arms of the cross containing burnt and surrounding unburnt area was submitted for histology. Burn induced at 180º C was confirmed to be of partial thickness severity while 200º C resulted in a full thickness burn. The physiologic response of the partial thickness burn was seen as an in rush of fluid to the site of injury immediate post burn. The edematous fluid reorganized at about 8 hrs post burn with the wound area appearing hyperhydrated. Images of the burn wound at 24 hr, 48 hr, and 72 hr show the evolution of edema throughout the wound in the surrounding area. Hyperhydrated and hypohydrated areas are visible and observed to change in location and intensity throughout the 72 hour period.

The full thickness burn appears to be relatively dehydrated as opposed to its partial thickness counterpart. The edematous response following full thickness injury is observed to be low. It could be argued that the thermal injury blocks off the flow of fluid in and around the injury site. The 24 hr, 48 hr, and 72 hr images show significant changes in perfusion. In both the burns the reduced perfusion ring of tissue surrounding the burn which we hypothesize is the zone of stasis is clearly visible.

7.5 Preliminary data analysis

7.5.1 GUI

A graphical user interface (GUI) was created for analyzing the data. The data file was input and corresponding image generated. The image can be generated in black and white or color map (256). The analysis tool allows taking a line segment or a polygonal segment across the image. Line segments across the wound produced line curves off which reflectivity values

111

were noted. The GUI allowed the user to visualize and place the cursor at the desired location in the image. Placing the cursor at one point and clicking and then double clicking at the second point drew a line segment. A line curve was automatically generated off which the reflectivity values were noted.
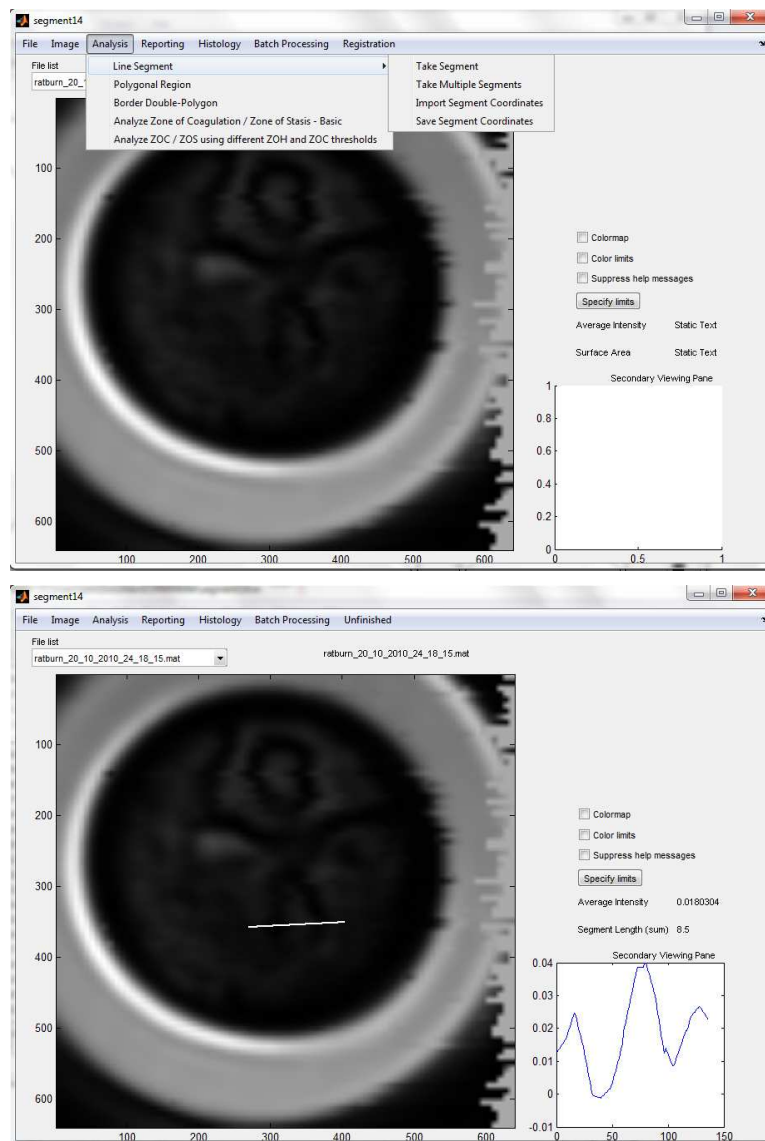
Fig 7.15: Graphical user interface used for generating burn wound curves

7.5.2 Burn zone curves

A line segment cut through one of the crosses was taken for both the burn categories for the 8-hour and 3-day study. The data was normalized with reflectivites between 0 and 1 using the equation for a straight line

$$y = (y_{max}-y_{min})[x_v]/(x_{max}-x_{min}) + c$$

where y_{max} & y_{min} are 1 and 0 respectively. x_v is the matrix of raw reflectivity values and x_{max} is the maximum reflectivity noted off Aluminum & x_{min} is the minimum reflectivity noted off air. The constant c was calculated by setting y to 1.
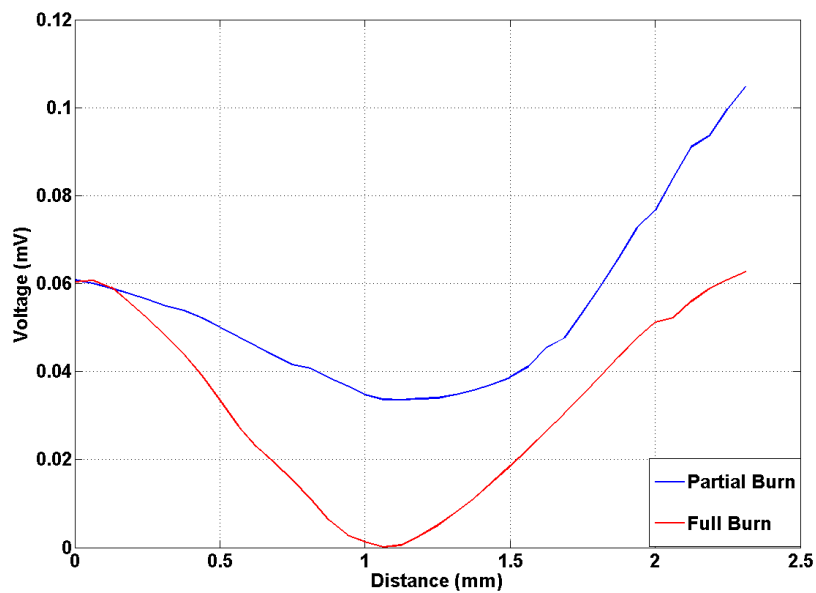
Fig 7.16: Burn zone curves from one of the arms of the cross at 8 hrs post burn from the 8 hour study

113
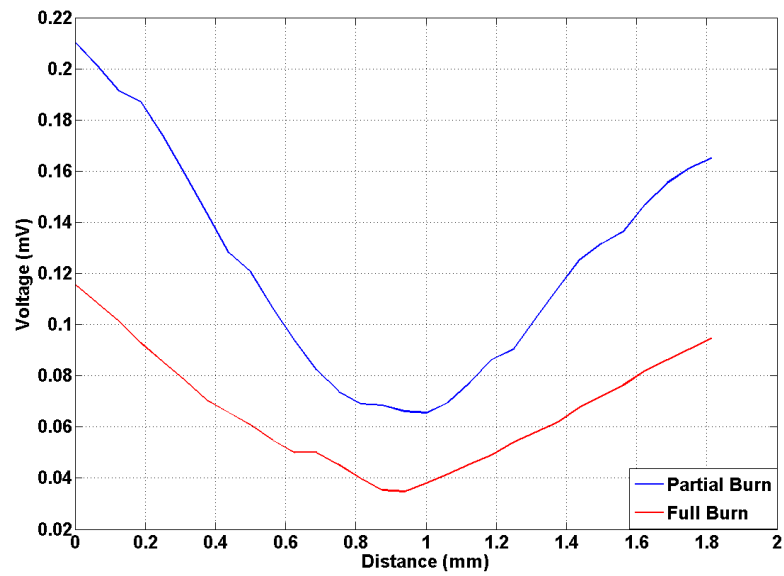
Fig 7.17: Burn zone curves from one of the arms of the cross at 8 hrs post burn from the three day survival hour study
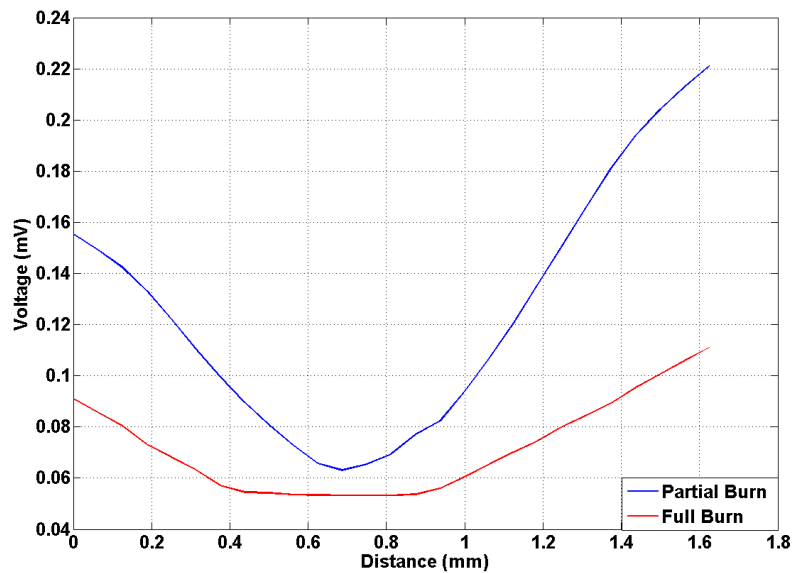
Fig 7.18: Burn zone curves from one of the arms of the cross at 72 hrs post burn from the three day survival hour study

114

As evident from the images, partial thickness appears to be more hydrated than the corresponding full thickness burn. The curve starts from hydrated zone of hyperaemia and dips as it goes through the zone of stasis and hits the trough with the zone of coagulation. A similar trend is seen on both sides of the wound. Further, the reflectivity values for the different zones in the full thickness burn are much lower than the partial thickness burn.

7.5.3 Average reflectivity's and thickness of zone of stasis

The average reflectivity of the zone of coagulation for the partial thickness burns was ~33% higher than the full thickness burn. These values were calculated using images at time points 15 min, 30 min, 45 min, 1 hr, 1 hr 15min, 3 hr 15 min, 7 hr 30 min, 24 hr, 48 hr and 72 hr following burns. The intensity and thickness of zone of stasis were two other parameters used for distinguishing the partial thickness from full thickness burns. On an average, partial thickness burns had a zone of stasis ~21% brighter than corresponding full thickness burns. Partial thickness burns were found to have a thicker zone of stasis enveloping the central zone. Due to anunevenzone of stasis border we were unable to quantify the thickness of the zone. Modifications to the GUI are necessary to take into account the non-uniformity of the zone.

7.6 Study limitations

7.6.1 THz system

The above experiments were done in the rat surgical suite, UCLA vivarium. Prior to the experiment the system was moved to the surgery room and re-aligned. The system was calibrated

every morning before the experiment. The THz scanner sits on an optic table that adds to the overall bulkiness of the system. During transportation the scanner had to be disassembled from the table to make the move easier. Not only was the process tedious but also increased the probability of system getting misaligned. The 8 hr and 3-day study were done on different days several months apart. Even though the data has been normalized using maximum and minimum reflectivites on the individual days, comparison between the two experiments is not entirely equitable. The THz system is prone to drift

7.6.2 Experimental set up

The rat was restrained using electrical tape. The arrangement was adequate for the first few hours. It was noticed that the tape lost elasticity and stickiness after couple of hours making the set up less robust for the long survival studies.
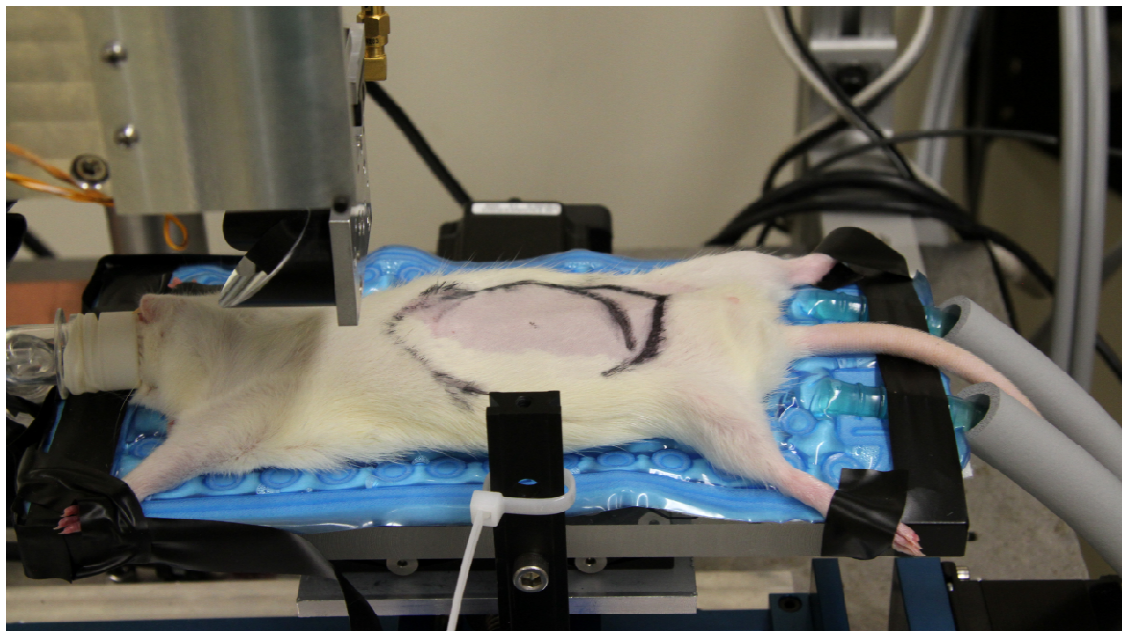
Fig 7.19: Rat restrained during the experiment

The rat was kept under anesthesia for the entire time course of the experiment. The nose cone was fixed on the animal's snout by affixing the glove under the rat's incisor. The nose cone was then taped to the imaging mount. The tubing was taped to the side of the optic table with some slack for allowing movement during the raster scan. With repeated scanning, the nose cone arrangement became loose and came off the rat's nose several times during the experiment.

7.6.3 Data Analysis: Lack of image registration:

The feasibility experiments lacked image registration. The visible pictures were not taken at the same time points as the THz images thereby preventing the translation of pixels acquired by the imager to the surface features at different time points. The Mylar window was removed between every scan. Due to lack of external fiducial markers and height settings, the window placement on the rat cannot be assumed to be same for every scan. This changes the region of interest between every image rendering the intrapatient scans incomparable for any quantitative analysis. Further the two rats under the same study had no interpatient registration and thus could not be compared.

Despite the above mentioned drawbacks in the experimental design, reflectivity values calculated from normalized 8 hour and 3 day studies were used as a reference for the future set of experiments.

7.7 Controlled rat study

7.7.1 Sample size calculation

Average reflectivity values for the full thickness and partial thickness categories from the

3-day study was used for estimating the sample size for the controlled rat study. The images at time points 15 min, 30 min, 45 min, 1 hr, 1 hr 15min, 3 hr 15 min, 7 hr 30 min, 24 hr, 48 hr and 72 hr following burns were used for the calculations. The curves were analyzed to find the mean, the variance, and the Standard deviation for each image.

$$m = \frac{\left(\sigma_1^2 + \sigma_2^2\right)\left(z_{1-\alpha/2} + z_{1-\beta}\right)^2}{\left(\mu_1 - \mu_2\right)^2}$$

m= number of animals required per group

σ^2=Variance of the first group (σ_1^2) + variance of the second group (σ_2^2)

z=the different percentiles we are looking for; The first z gives 97.5th percentile while the second z gives 80th percentile

μ= the estimates of the means for the two groups

It is found that m=5 give94% efficiency. Therefore sample size 5 per category is required.

7.7.2 Modifications

Anesthesia set up:

The area designated for doing a controlled rat study was inspected by Animal research committee (ARC) at UCLA and classified as a study area.

118

Fig 7.20: Rodent anesthesia machine

A portable rodent anesthesia machine was purchased from Highland Medical and installed. Oxygen gas from the cylinder is mixed with isofluorane from the vaporizer and enters the breathing circuit through the gas outlet. Corrugated breathing tubing delivers the mixture to the nose cone through one end attached onto the rat's snout and the other to the F-air canister. The oxygen pressure is kept at 0.8 ml/min and isofluorane at 2% for maintenance of animal under anesthesia.

Brand

Brass was the material of choice for the new brand. The shape was simplified to a rectangle 19 mm x 5 mm x 19 mm protruding from a square base (19 mm x 19 mm x 19 mm). An 8-32 tapped hole was drilled at the base of the square base to attach it to the aluminum

holder. A teflon piece was used as a spacer between the brand and holder to ensure minimum heat loss.

For precise temperature monitoring, a thermocouple (Omega Engineering, Inc.) was used. The thermocouple was placed inside the fin of the brand close to the edge through a hole and situated in place using a screw. A small diameter (0.005") was chosen to ensure precision in monitoring temperature.
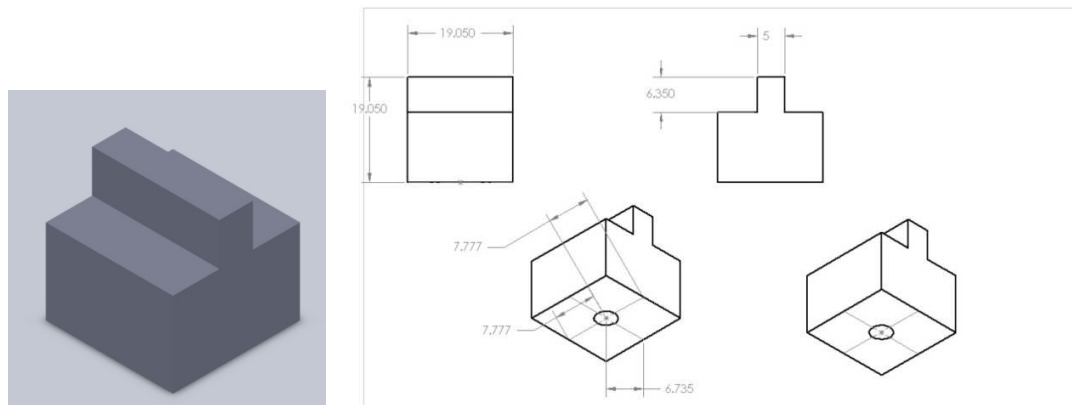
Fig 7.21: 3-D drawing of the brass brand used for controlled rat study. The sketches on the right show the dimensions of the brand

Base plate:

The old arrangement involved anchoring the THz optomechanic and electronic components on to an optic table. This made the whole set up bulky and space consuming rendering it difficult to move. Further it was hard to clean the optic table. A new base plate was designed to overcome these drawbacks. The plate was designed in Solidworks with four ¼-20

holes for fixing the translation stages. Two grids of four holes each were drilled for the imaging head and camera mount. Aluminum was the material of choice due to its lightweight and inexpensiveness. The plate was anodized for surface corrosion protection.

a)
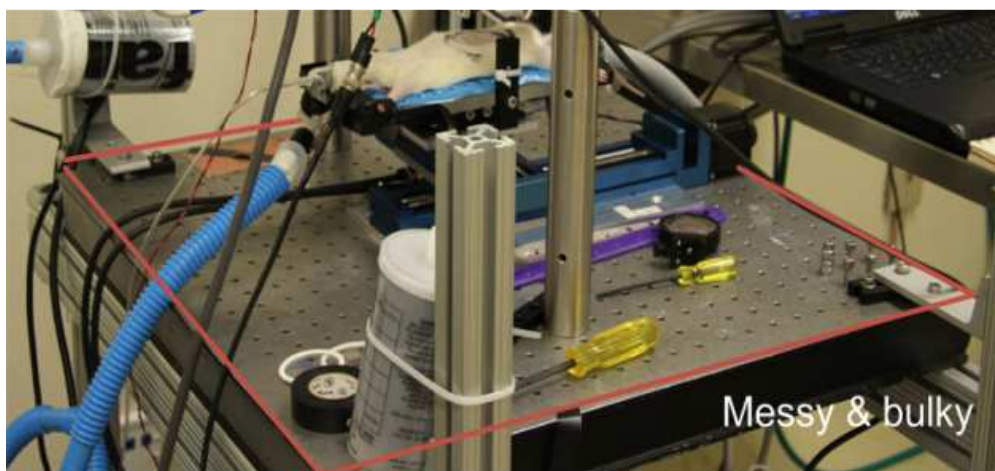
b)
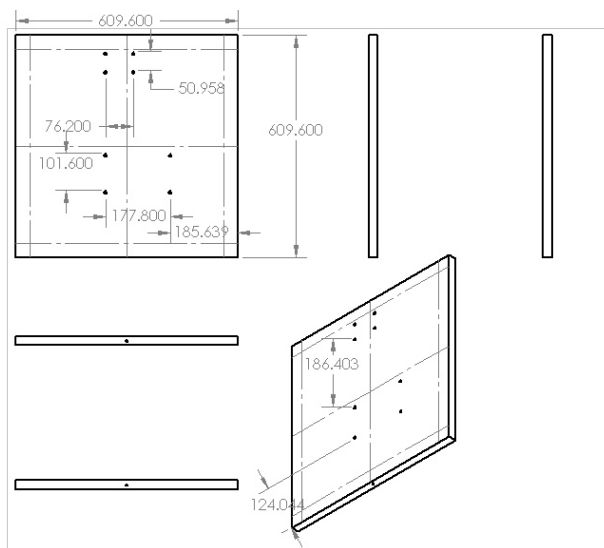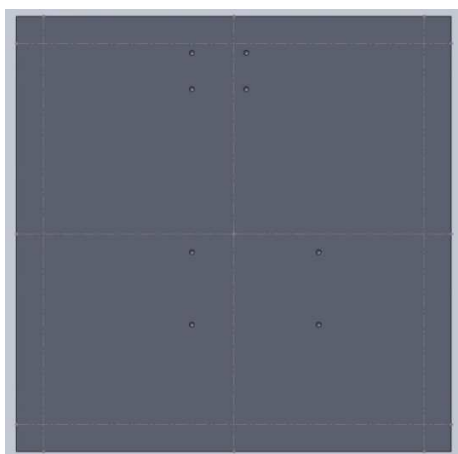
c)
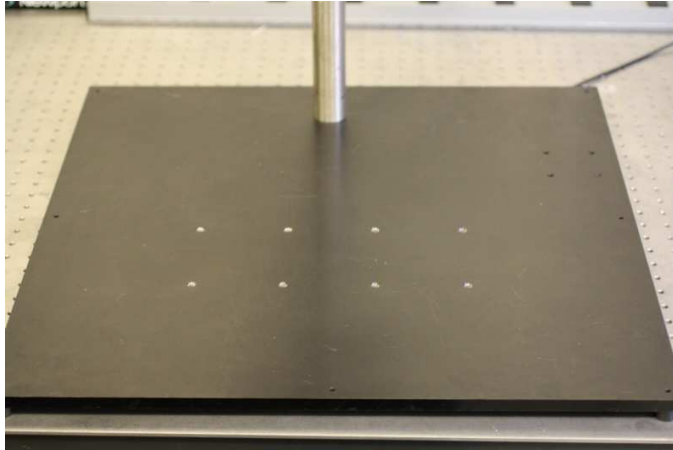
Fig 7.22: a) Old base plate, b) 3-D drawing of the new base plate and c) visible picture

Camera mount:

Fig 7.23: Visible picture of the camera mount used to hold the digital camera during the experiment

A digital SLR camera was used to take visible pictures for comparison with the corresponding THz images. The camera was mounted on an aluminum rod mount with clamps and adjustable rods for flexibility along the x, y and z direction. The camera position was kept fixed for the entire duration of the experiment.

Rat mount:

A rectangular mount (5" x 10") made out of polypropylene was used to stage the rat for the experiment. The rat was secured to the mount in a supine position by tapping the feet and arms with an electrical tape. Though the arrangement proved adequate the tape had tobe adjusted several times during the experiment.
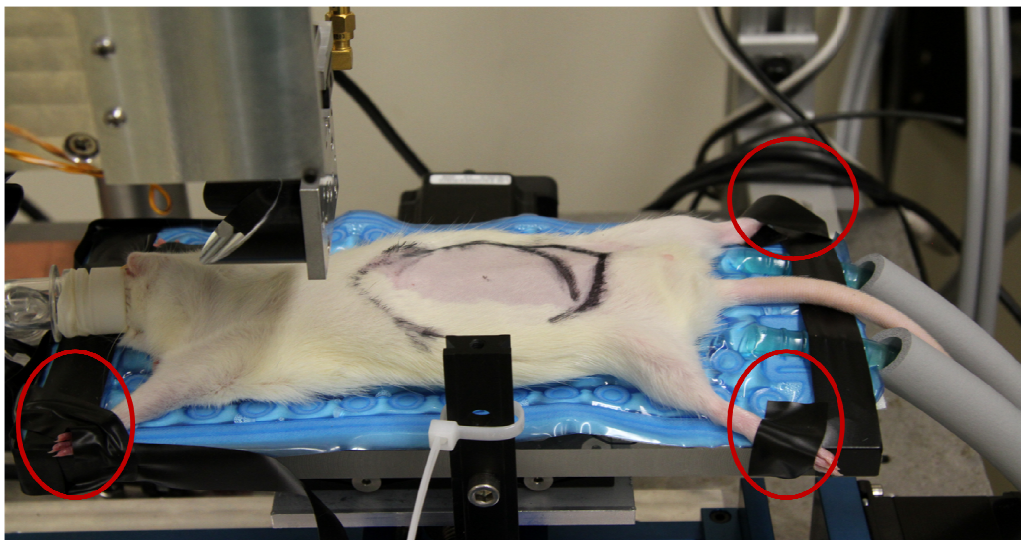
Fig 7.24: Rat restrained with electrical tape

The solution was found by designing a thin copper piece with 5/16" slits. The piece was taped to the water circulation pad and the animal secured to the piece with gauze strips. The

strips were passed through the slit and tightened using plastic stoppers restraining the rat's arms and legs.
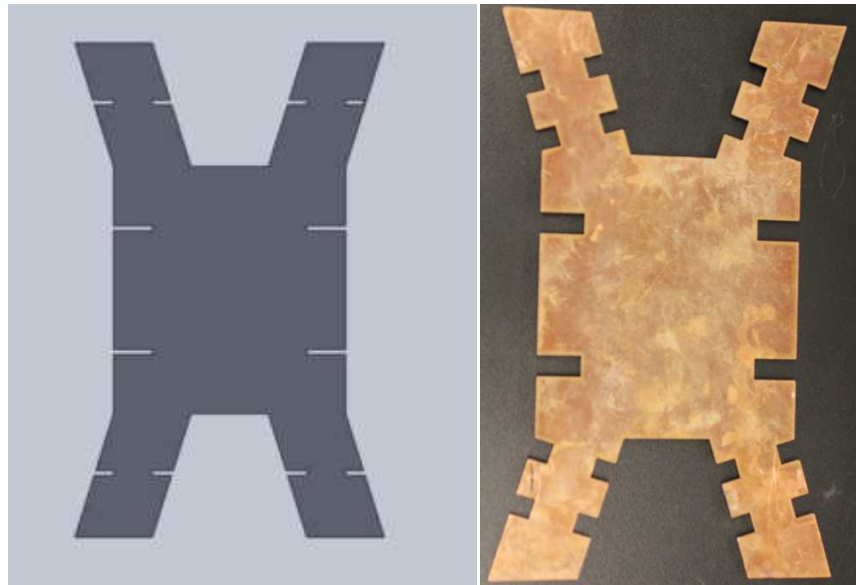
Fig 7.25: (Left) Schematic and (right) visible picture of the copper piece used for restraining the rat

Nose Cone& holder:
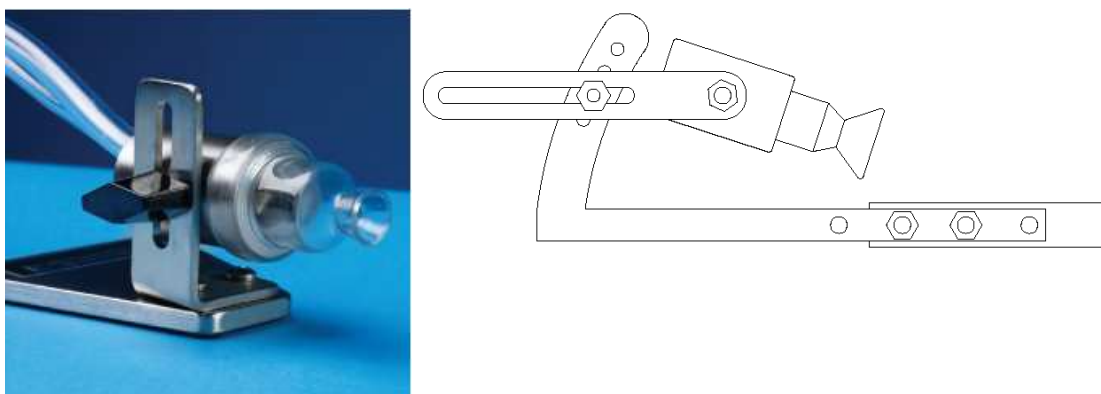
Fig 7.26: (Left) Nose cone from EZ Anesthesia and (right) design of holder for mounting the nose cone

A breathing device, EZ-103A Microflex Breather was purchased from E-Z Anesthesia to serve the purpose of a nose cone. The breathing device consisted of nose cone, valve, an input tube for delivering anesthetizing gas and an exhaust tube for sending unused gas to charcoal filter. The valve mitigates gas flow while the tight fitting nose cone eliminates gas leakage. The cone was fitted onto the rat's snout where it created a tight fitting. The arrangement was good for the entire length of the experiment.

Nose cone was fixed to the rat mount using a metal frame with movement along y- and z-axis. The frame was adjusted so as to approach the rat's snout at an angle. The nose cone was put on the rat's snout and frame fixed in place by tightening the screws.

CHAPTER – 8: CONTROLLED RAT STUDY

8.1 Three burn test

A three-burn experiment was done as a prelude to the main study for validating the system performance and experimental protocol.

Male SD rat weighing 720 g was anesthetized using gas anesthetic isofluorane. The rat was placed on the copper plate and its extremities tied to the plate. The plate was further taped on to water circulation pad. Isofluorane anesthetic was used at 4% for induction and 2% for maintenance.

Upon preparation, the rat was placed on the mount and a flat abdominal area was identified. Mylar window was placed flush against the skin. Control scan of the area (4 cm by 4 cm) was taken.

Brand temperature was precisely monitored using a thermocouple (Omega Engineering, Inc.). The thermocouple was placed inside the fin of the brand close to the edge through a hole and situated in place using a screw. A small diameter (0.005") was chosen to ensure precision in monitoring temperature. Three temperatures were chosen based on previous studies and literature search – 120° C, 160° C and 200° C to ascertain the final two temperatures for the rat trial. The brand was placed on the hot plate and upon reaching the desired temperature was placed in contact with the rat's abdomen for 10 sec. The drop in temperature resulting from heat transfer and environmental cooling was noted.

126

For every burn, pair of before and after images was taken. The rat was woken up following the images and kept alive for three days. Follow up images were taken at 72 hrs. Rat was sacrificed and skin resected and submitted for histology.

a)
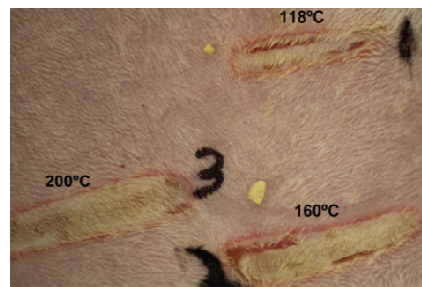
b)

118 C
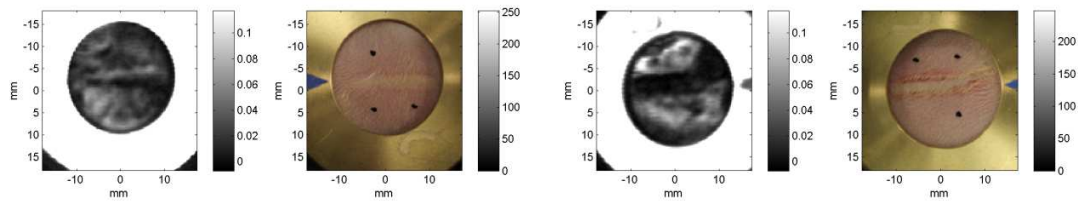
160 C
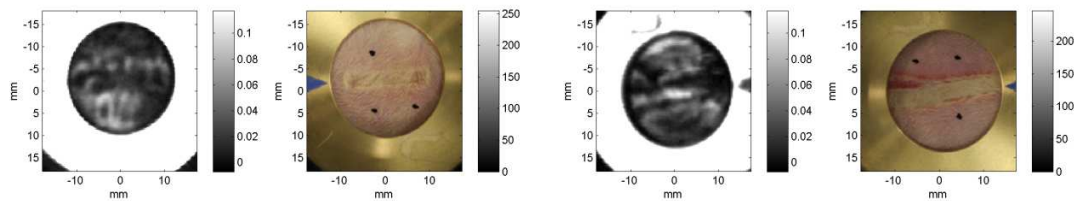
200 C
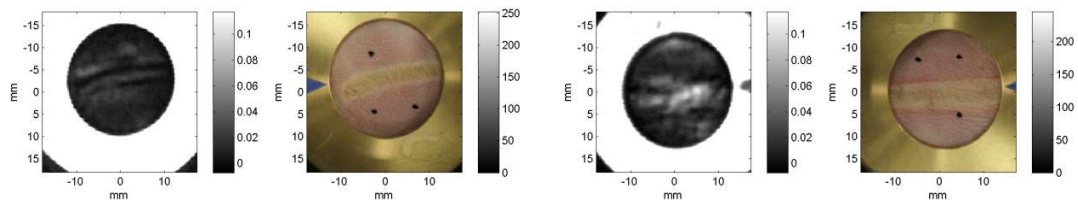
Fig 8.1: a) Visible picture showing 118, 160 and 200 C burn three days post burn, b) (left) THz images immediate post burn and (right) three days post burn

The visible pictures and THz images immediate and 72 hours post burn are reported. Histological evaluation of the burn sections shows the 118 C is a superficial partial thickness burn. 200 C burn was identified as a full thickness burn. In case of the 160 C burn there was a little bit of uncertainty. The depth of damage would qualify 160 C to be full thickness however neutrophils and macrophages in the dermal region indicate regeneration, suggesting a lower severity as opposed to the 200 C burn. A temperature between 118 and 160 was chosen to inflict a lower severity burn. Finally, 130 C and 200 C were selected as the two temperatures for inducing partial and full thickness burns.

8.2 Experimental design

8.2.1 Animals

Male SD rats were used for the controlled rat study. The animals were batch ordered three months prior to the experiment and housed in 6th floor of UCLA vivarium. The weight range of the animals was 465 g to 680 g.

Table 8.1: Name and weight of rats enrolled in the study

Rat Label	Rat name	Weight (g)
0000410094	A	465
0000437467	B	530
0000437469	C	550
0000410096	D	606
0000398988	E	625
0000398989	F	680
0000410095	G	650
0000437470	H	608
0000438269	I	600
0000438268	J	577

The rats were prepared for the experiment as per ARC guidelines. A relatively flat area on the abdomen was selected and shaved with surgical clippers. The surgical site was then cleaned with three alternating scrubs of Betadine and 70 % alcohol. Prior to imaging the animal was subcutaneously injected with Buprenorphine (0.05 mg/kg), a pain relieving drug. The rat was restrained on the copper plate in a supine position with arms and legs stretched out and tied to the plate with surgical ribbons. The plate was placed on the mount over the water circulation pad. The water circulation pad ensured maintenance of near body temperature during the course of the experiment.

8.2.2 Imaging

A 12.7 µm Mylar window suspended from a brass frame was used to make the imaging plane uniform. The window was pressed against the skin with contact pressure. This defined the field of view. The boundary of the frame was traced on the skin with a thick black sharpie. A 40 mm x 40 mm scan of windowed abdomen was taken prior to injury for all the animals. The THz reflectivity was maximized off animal's skin for every individual.

Following the control scan, window was removed and the burn inflicted using the rectangular brass brand (19 mm x 19 mm x 5 mm) with the longer edge of the rectangle being orthogonal to the rostrocaudal axis of the animal. The brand was heated up to the desired temperature; 130^0 C for partial thickness category and 200^0 C for full thickness and pressed against the skin for 10 sec with contact being the only pressure. One burn was induced per rat within the control scan area. Post burn the animal was scanned every 15 min for the first hour and every 30 min for the remaining 6 hrs taking about 10 min to acquire an image. The Mylar

window was kept stationary during continuous scanning to remove any discrepancies in z settings arising from removing the window between scans. At the end of 7 hrs, the rat was roused and taken back to the vivarium. Rats were housed in cages with care fresh bedding to ensure minimum discomfort to the wound and antibiotic Trimethoprim-Sulfamethoxazole was administered orally. Follow up scans were taken at 24 hrs, 48 hrs and 72 hrs post burn. The rats were euthanized on day 3. Sections of skin along the rostrocaudal axis were taken from the left, center and right region of the burn containing the burnt and surrounding normal area and submitted for histology. 6 sections per region at a micrometer setting of 8 μ were analyzed for the determination of burn severity.

8.2.3 Image registration

External fiducial markers were used to align the THz images to their respective visible pictures. Two triangular painter's tape pieces positioned on diametrically opposite sides of the brass frame of the Mylar window served as the markers. The triangles were visible in the THz image. A visible picture was taken before every THz scan. The markers on the visible picture were aligned with the corresponding view on the THz images with respect to location and size of the markers. The Mylar window was kept stationary during continuous scanning resulting in all THz images being registered to one another during the 7 hr period.

Interpatient registration was performed as follows. The center of the burn was chosen to be the intrinsic fiducial marker. Setting the center as the point of origin, THz images across all rats were rotated and translated to line up in the same orientation.

130

8.3 Results

8.3.1 Image generation

Below are the time series of THz images from Rat A depicting the evolution of burn over a span of three days. The burn on Rat A was induced at a temperature of 130^0 C and later confirmed to be of partial thickness severity across all regions. The images were generated in both gray and color (256) scale. All the images were normalized with respect to their respective control image. For every subject there were a total of 21 images – a control image, 17 continuous scans and 3 follow up images. Videos depicting the wound evolution for four rats over three days have been uploaded as supplemental material.

a)

Left	Center	Right

b)

Control · Post Burn

15 min · 30 min

45 min · 1 hr

1.5 hr · 2 hr

2.5 hr · 3 hr

3.5 hr · 4 hr

4.5 hr · 5 hr

5.5 hr · 6 hr

132
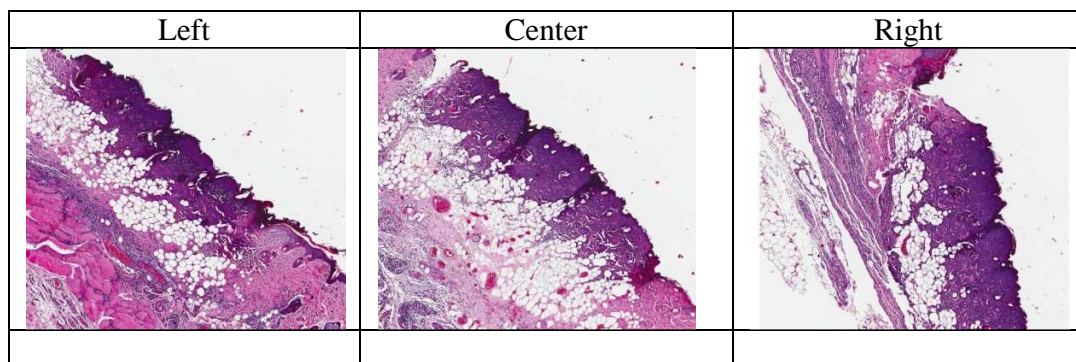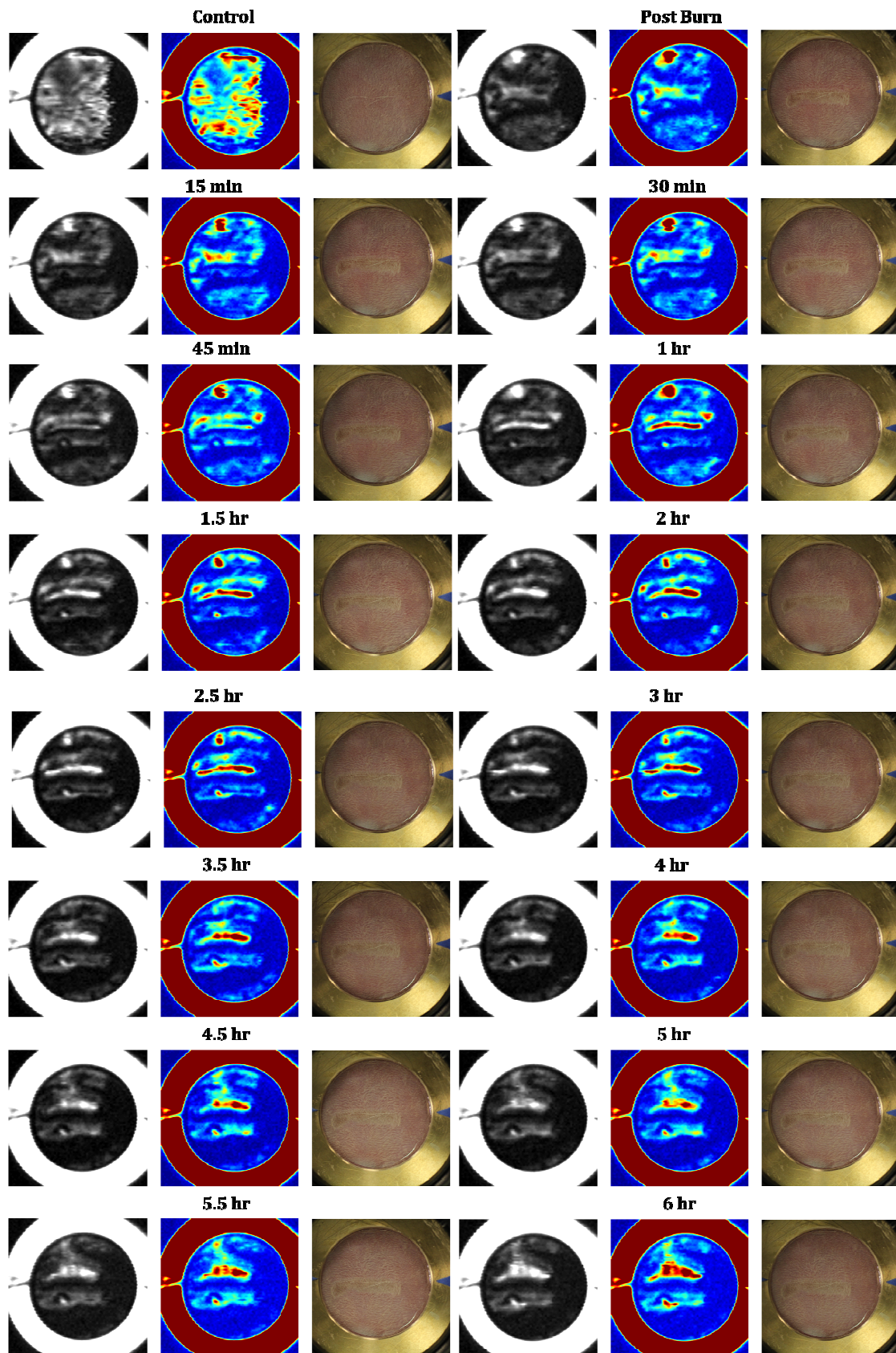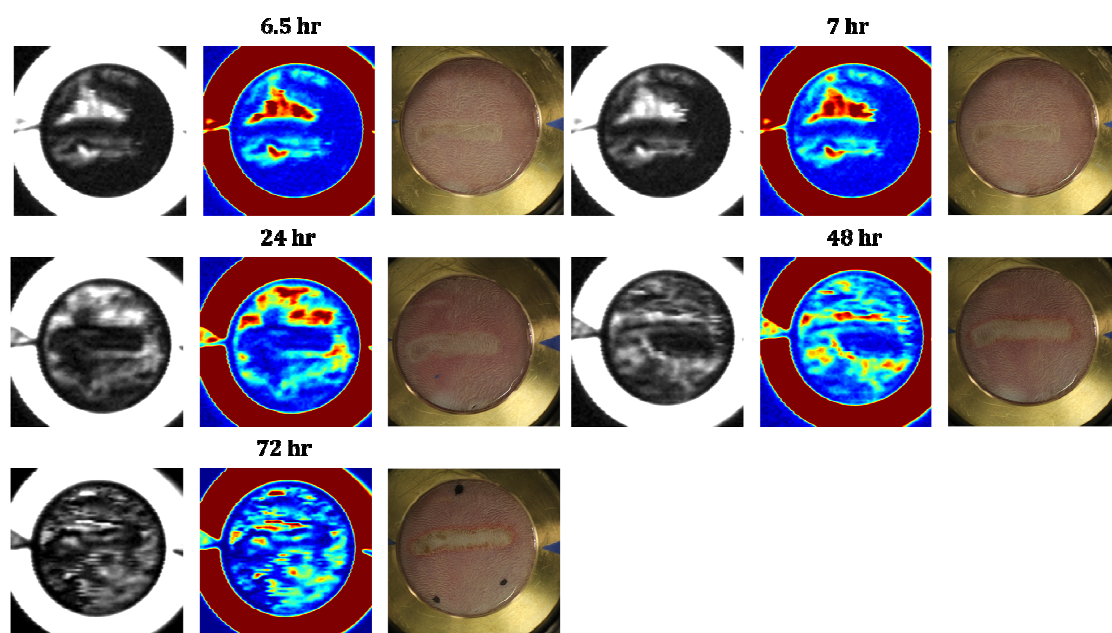
Fig 8.2: a) H&E sections from left, center and right regions of Rat A's burn, b) THz images in gray and color showing the evolution of burn over 3 days

8.3.2 Histological analysis
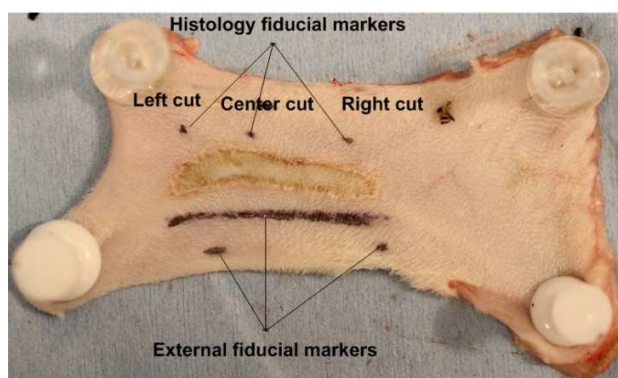
Fig 8.3 Sample preparation for histopathological analysis

Fig 8.3 shows the resected skin from Rat A in the rostrocaudal axis. The orientation of skin is the same as the orientation of the visible and THz images. Three sharpie dots and a line served as

external fiducial markers. The burn region was divided into three segments and marked with dots using India ink. These served as histology markers. Segments were cut orthogonal to the longer edge of the burn in the left, center and right regions containing the dots respectively. Each of the three segments gave 6 sections each which were H&E stained and analyzed to determine burn severity.
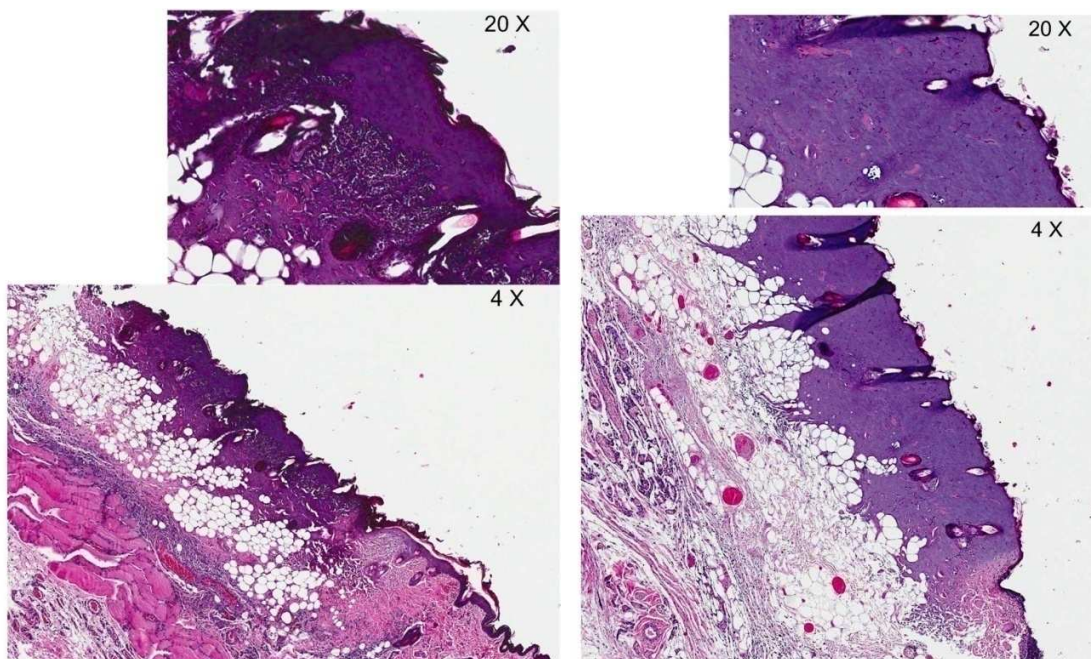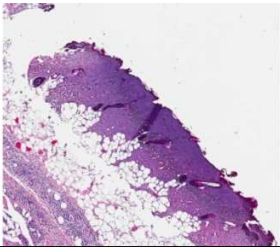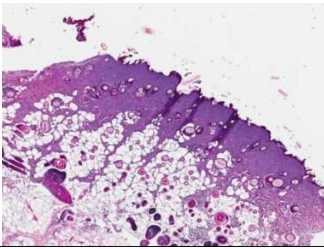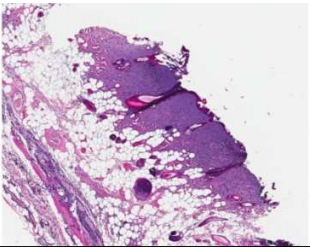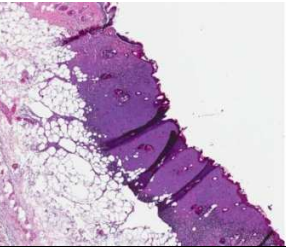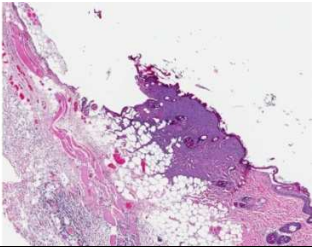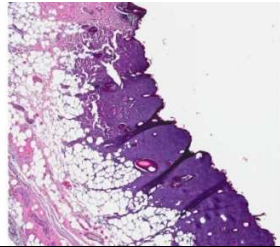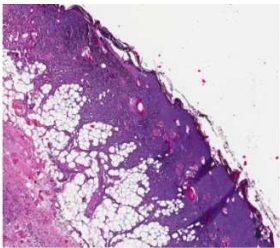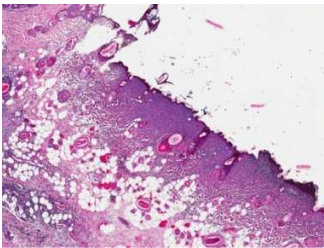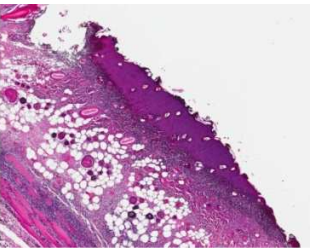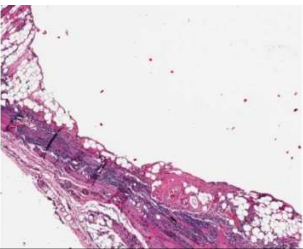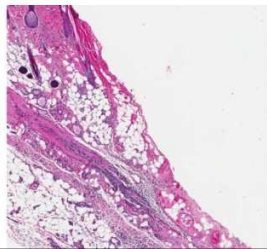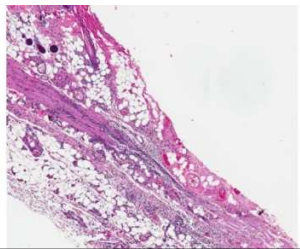
Fig 8.4: H&E sections showing (left) partial thickness and (right) full thickness damage

Classification of the above burns into burn severity category was based on depth of injury measurements calculated by measuring collagen discoloration, patency of blood vessels and infiltration of neutrophils and macrophages in the dermal space[179, 180].

The two temperatures used for our study gave partial thickness and full thickness severities. Biopsies from rats induced at 200⁰ C showed a complete loss of collagen crystallinity which caused the change in H&E stain color from red to blue. Full damage all through the dermis up to the subcutaneous layer and blocked blood vessels were noticed in full thickness burn sections. In contrast patent blood vessels and neutrophils and macrophages were used as distinguishing features for deciding whether a section was of partial or full thickness severity. A blind examination of sections was carried out for an unbiased analysis.

Table 8.2: H&E sections of partial thickness and full thickness severity across burn wound in 4 rats. * denotes scratching was observed between day 2 and 3
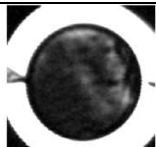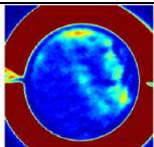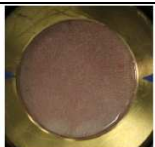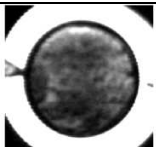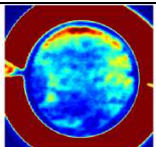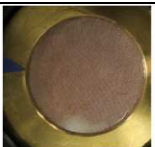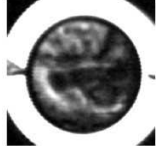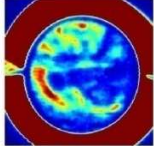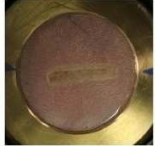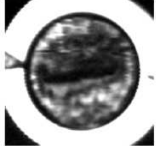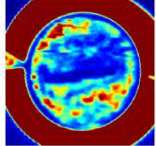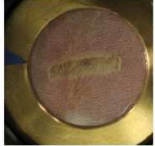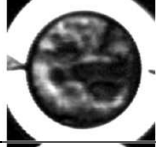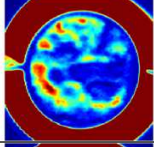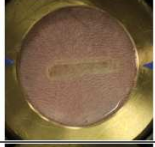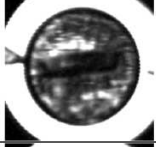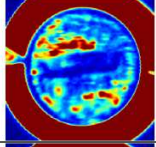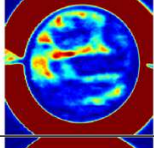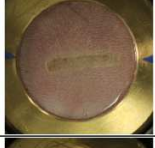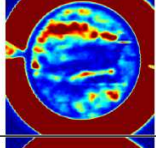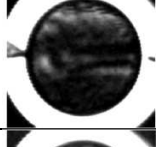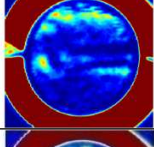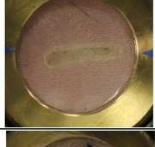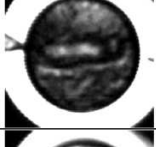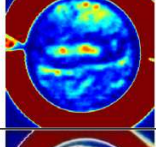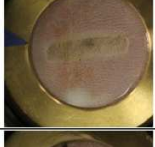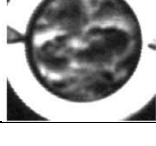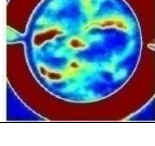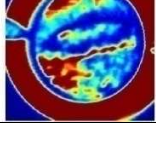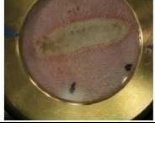
Rat	Burn severity		
	Left	**Center**	**Right**
C 130ºC	Partial	Partial	Partial
E 130ºC	Partial	Partial	Partial
H 200ºC	Full	Partial	Full
J 200ºC	Full*	Full*	Full*

8.3.3 Image analysis
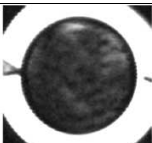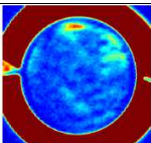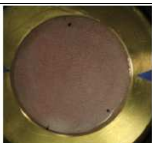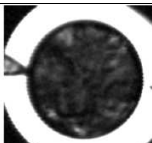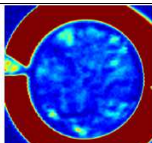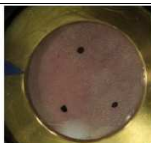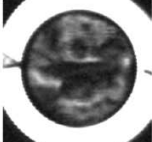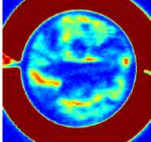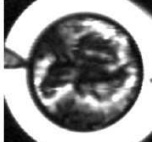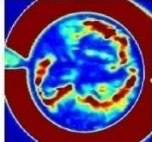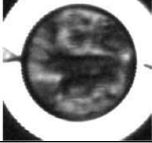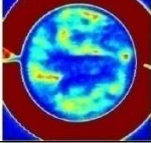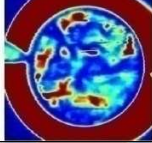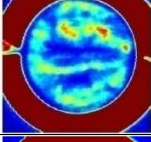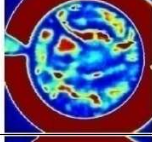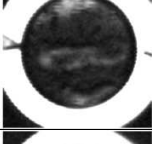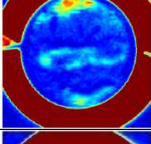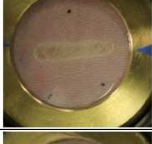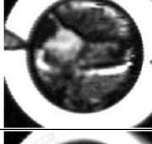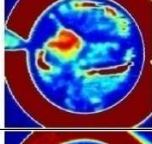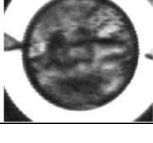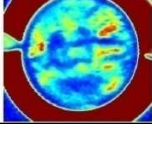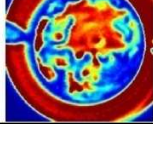
Representative scans from partial thickness and full thickness burns at time points - immediate post burn (t=0), 30 min, 1.5 hr, 7 hr and 72 hrs following burn induction are presented below.

Table 8.3 a) & b) THz images of partial thickness and full thickness burn wounds over 72 hrs. Visual changes in THz images were noticed in images at these time points

a)

Time	Partial thickness (Rat C) 130⁰ C	Full thickness (RatH) 200⁰ C
Control		
Immediate Post burn		
30 min		
1.5 hr		
7 hr		
72 hr		

b)

Time	Partial thickness (Rat E) 130	Full thickness (Rat J) 200
Control		
Immediate Post burn		
30 min		
1.5 hr		
7 hr		
72 hr		

The following time periods were selected based on visual appearance of significant morphological changes in the field of view across all rats. The immediate post burn image for both the burn severities appear brighter than their corresponding controls. It has been reported that thermal injury is followed by an instantaneous inflammatory response beginning as early as couple of minutes post injury[48].For burns less than 10% total body surface area, this response is local and confined to the vicinity of the injured area[47, 48, 181]. Rapid transudation of fluid from intravascular to extravascular space increases the net water content of injured tissue. This physiological response is captured in the first 30 min by our THz system which is sensitive to changes in water concentration in the tissue. The flow of water to and from the site of injury is visualized in the THz images acquired at t=0 and t=30 min. At 1.5 hrs post burn, the shape of the burn becomes discernible in both the burn groups as evident from the THz images. Literature reports that edematous response following burns continues to rise and has been found to be maximal around 3 hours post burn[182].A similar response is seen in the THz images acquired over the span of first few hours for both burn categories. A tissue ring of low reflectivity which has been seen previously by our group and been hypothesized to be the zone of stasis is observed in both burns in all the images. THz images of burn wound at 7 hrs begin to show fluid redistribution in the field of view. It is known that the rapid phase of edema is followed by redistribution and resorption. Resorption of fluid begins at about 24 hours post injury which is observed in our THz images as well[181]. No change is noted in the visible pictures taken corresponding to THz images over the continuous scanning period. The 72 hour image is taken for histological correlation.

The THz images acquired over the course of three days show the influx and dissipation of edema in the wounded area. Shifts in hydration are observed in the follow up images acquired at day 2 & day 3.THz images of full thickness burns appear brighter than the partial thickness burns over the 7 hour period. However4 out of the 10 rats had burns of both partial thickness and full thickness nature hence nothing conclusive can be said unless the data is analyzed quantitatively.

8.4 Preliminary statistical analysis

8.4.1 Burn sections

Three segments corresponding to histology cuts along left, center and middle regions of the burn were used for statistical analysis. This accounted for variations across severity observed in some burns. The segments obtained from THz images were not registered with histology. It was however assumed that histology was representative of burn characteristic of that particular region.

Three vectors of equal length extending from the edge all the way across the burn in the caudal rostral direction were drawn. The vectors were randomly spaced across the burn. Each burn had a left, center and right reflectivity vector and was matched against burn severity of that region. 30 segments gave 17 partial thickness and 13 full thickness reflectivity vectors. Not all segments were used for the analysis.
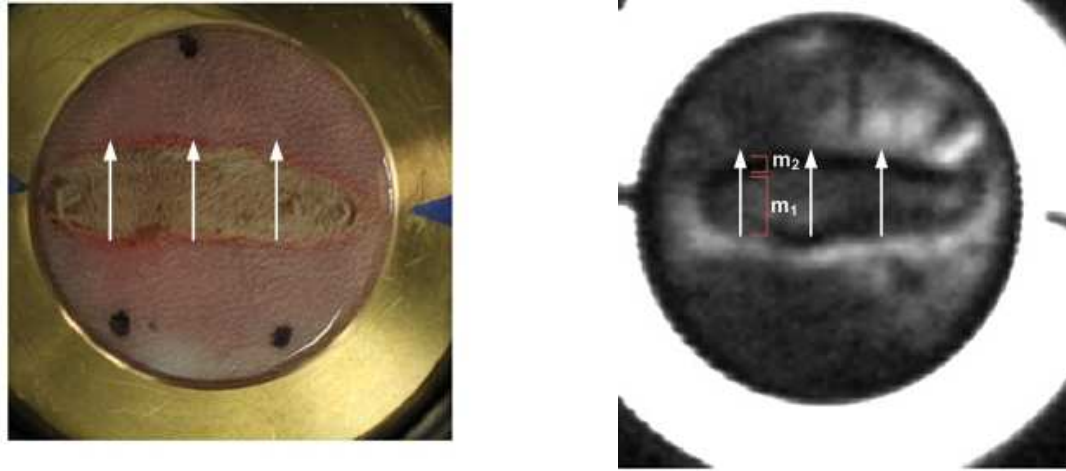
Fig 8.5: Procedure for obtaining mean wound zone reflectivities. (Left) Cuts made through the burn wound in the visible picture translates to (right) reflectivities across the wound from the THz image

The first 5 mm of the vector were averaged to give m_1 which represented mean reflectivity across the zone of coagulation. The next 1 mm was taken to be representative of zone of stasis and mean reflectivity m_2 was used for analysis.

8.4.2 Partial thickness vs. full thickness

Images taken in the continuous scanning period (7 hours) were registered and normalized across all rats and hence used for statistical analysis. Control and follow up scans could not be considered for any quantitative analysis.

Multivariate statistical tests - Pillai's trace, Wilks' Lambda, Hotelling's trace and Roy's Largest Root were used for testing difference between partial thickness and full thickness burns

both for differences in mean reflectivities (m_1 and m_2 combined) and dependence on time. Images acquired at t=0 (immediate post burn), t= 1.5 hour and t=7 hour were used.

Table 8.4 Results for partial and full thickness groups combined

Tests	p-values	Significance
Multivariate	0.066	No
Time Interaction	0.081	No
Pairwise (full vs. partial)	0.046	Yes

The above table shows that partial thickness and full thickness burns cannot be distinguished from one another on the differences in reflectivities when all three time points are considered. However a pairwise test between the two groups without taking time into account gives a significant result which suggests that there is a significant difference in the wound reflectivities of partial thickness and full thickness burns but time adds variability. Other image time points were also explored and similar results were obtained. Partial thickness and full thickness burns have significantly different wound reflectivities but the time at which they become apparent is unclear.

142

8.4.3 Partial thickness

Differences in reflectivities across the zones of coagulation (m_1) and zone of stasis (m_2) within individual groups were tested. Time points t=0, t=1.5 hr and t=7 hr were used and time of acquisition was treated as a covariate for multivariate tests.

Table 8.5 Results for the partial thickness group

Tests	p-values	Significance
Multivariate	0.018	Yes
Time Interaction	0.011	Yes
Pairwise (m_1 vs. m_2)	0.018	Yes

p-values for all the tests done for the partial thickness group were less than 0.05 indicating that a significant difference in mean reflectivities for zones of coagulation and partial thickness is observed. The time interaction is also significant meaning that these zones are distinguishable at all the time points. These results could infer that couple of min after injury, wound zones can be differentiated in partial thickness burns on the basis of their reflectivities. The zones remain distinguishable several hours after injury.

8.4.4 Full thickness

The same sets of tests were repeated for the full thickness group. Again image at time points t=0, t=1.5 hr and t=7 hr were used.

Table 8.6 Results for the full thickness group

Tests	p-values	Significance
Multivariate	0.094	No
Time Interaction	0.286	No
Pairwise (m_1 vs. m_2)	0.094	No

All the tests gave insignificant results. Full thickness burns were found to have indistinguishable wound zones over the 7 hour period.

8.5 Discussion

Contact burns of partial thickness and full thickness severity were inflicted on adult rats. There were 5 rats in each group with one burn per animal. The burns were induced by the same person for all the rats with temperature and time of contact being precisely monitored to ensure minimum variability in the burn induction process. The entire experiment was done unintermittedly for making the study as controlled as possible. These measures allowed us to attempt a quantitative analysis of the data which was lacking in the previous experiments.

The immediate response to thermal injury is characterized by a rush of fluid to the site of injury. The inflammatory response begins as early as couple of minutes post injury and continues for a couple of hours. Researchers have reported a 75% increase in water content of burned over unburned skin at 30 minutes post injury with 90% of that increase occurring in the first 5 to 10 min[53]. Edema formation is reported to be maximal 4 to 6 hours post injury and begins to resolve by 24 hours [52,181,182]. THz imaging captures the influx, redistribution and dissipation of edematous fluid in the burn region for both the burn severities. An overall increase in reflectivity is observed in the first post burn image across all rats. Image acquisition time of the reflective THz system is in the order of a couple of minutes which allows us to visualize the immediate post burn response. The subsequent images continue to appear more reflective though the increase in reflectivity is not homogenous across the field of view. The image acquired at 1.5 hours post burn for all the rats shows a clearly defined burn region with a dark ring of low reflectivity enveloping the burn. Classic burn wound pathophysiology describes three concentric burn wound regions: zone of coagulation, zone of stasis and zone of hyperemia[42]. Zone of

stasis is the intermediate region between the central zone of devitalized tissue and the outermost zone of hyperemia. This region is characterized by low perfusion and ongoing hypoxia. Hypoperfusion and free radical injury in the zone of stasis increases intravascular permeability promoting the leakage of fluid in the interstitial spaces[58].This translates to the appearance of zone of stasis as a low reflectivity region surrounding the burn in the THz images. Regions of high reflectivity in the vicinity of zone of stasis observed in the THz images relate to local fluid shifts occurring across the burn wound zones.

Several groups have reported the difficulty in inducing uniform contact burns. Factors such as skin thickness, skin hydration, blood supply and convective heat loss often cause varied susceptibility to thermal injury[183, 184]. This problem was addressed by analyzing the severity across three regions in the same burn. Skin segments from left, center and right regions chosen at random were submitted for histopathological evaluation. The results showed that 4 out of 10 rats had both partial and full thickness regions. Preliminary burn imaging experiments did not incorporate a thorough histological examination and due to lack of sufficient histological examination cannot be used as a reference for partial thickness and full thickness response in THz images. Other confounding factors inhibiting comparison between the present and previous results were small sample size, shape and size of the brand and burn temperature. However the previous experiments identified burn zone curves as a parameter for distinguishing between severities and were used for quantitative analysis for the present study.

The parameters investigated for distinguishing among partial thickness and full thickness burns were reflectivities of zone of coagulation and zone of stasis and how these changed with

146

time over the 7 hour period. Due to lack of image registration follow up scans could not be included in the analysis. Overall reflectivities of partial thickness and full thickness burns across for both the zones were significantly different but their dependence on time could not be isolated. The time variability was further investigated by analyzing the groups separately. It was discovered that for partial thickness burns the mean reflectivities of stasis and coagulation wound zones were different. The reflectivities were distinguishable as early as immediate post burn and remained significantly different for the entire 7 hour period. The full thickness group on the other hand showed no difference in reflectivities of the two zones at any time point.

Among body's early reactions to thermal injury, edema is the most dramatic physiological response. For burns covering less than 10% total body surface area the response is localized to the vicinity of the wound. Degree of burn severity influences the magnitude of fluid shifts and resultant edema. Full thickness injuries cause complete coagulation of vessels in the affected tissue thereby limiting edema formation. Partial thickness burns on the other hand have better vascular perfusion and therefore are more edematous. This explains the pronounced local fluid shifts occurring across the wound zones in partial thickness injuries. Our system which uses water as the primary contrast mechanism is able to detect these hydration shifts and is able to outline the zone of stasis in partial thickness burns. This distinction is evident as early as 10 min post burning and remains significant over 7 hours. Thermal insult to the tissue in deep burns results in greater tissue loss and lower perfusion as compared to milder burns. This renders the centrally affected coagulated zone indistinguishable from the peripheral zone of stasis over the 7 hours. While this prevents us from identifying the boundary of stasis zone in full thickness burns, it could be used as a parameter in distinguishing between the two burn severities. Monitoring of

147

full thickness burns over longer periods of time may provide a better insight into the behavior of the zone of stasis and its interaction with other two zones.

Burn wound progression, a process by which partial thickness burns convert to full thickness burns is a product of primary tissue loss and secondary consequences like altered perfusion, edema and toxic inflammatory mediators in the zone of stasis. Early identification of this zone can prevent progressive tissue loss. The present investigation suggests that Reflective THz imaging system might be able to identify the zone of stasis boundary as early as 10 min post injury. These results could have relevant clinical implications where early diagnosis dictates treatment. Early identification of vulnerable zone can prevent tissue loss, better treatment planning preventing delayed healing, likelihood of hypertrophic scarring and wound infection. A big sample size is however required to substantiate this claim.

Through the present investigation we might have identified burn classifiers for Reflective THz imaging. Reflectivities across burns, difference in reflectivities across zones of coagulation and stasis and time dependence of the evolution of these features are parameters that should be examined to differentiate between burn severities.

No change in visible pictures

Scratching for some burns

t = 0   t = 90 min   t = 7 hr   Day 1 to Day 3

Edema   Burn shape discernable   Wound zones visible   Fluid shifts
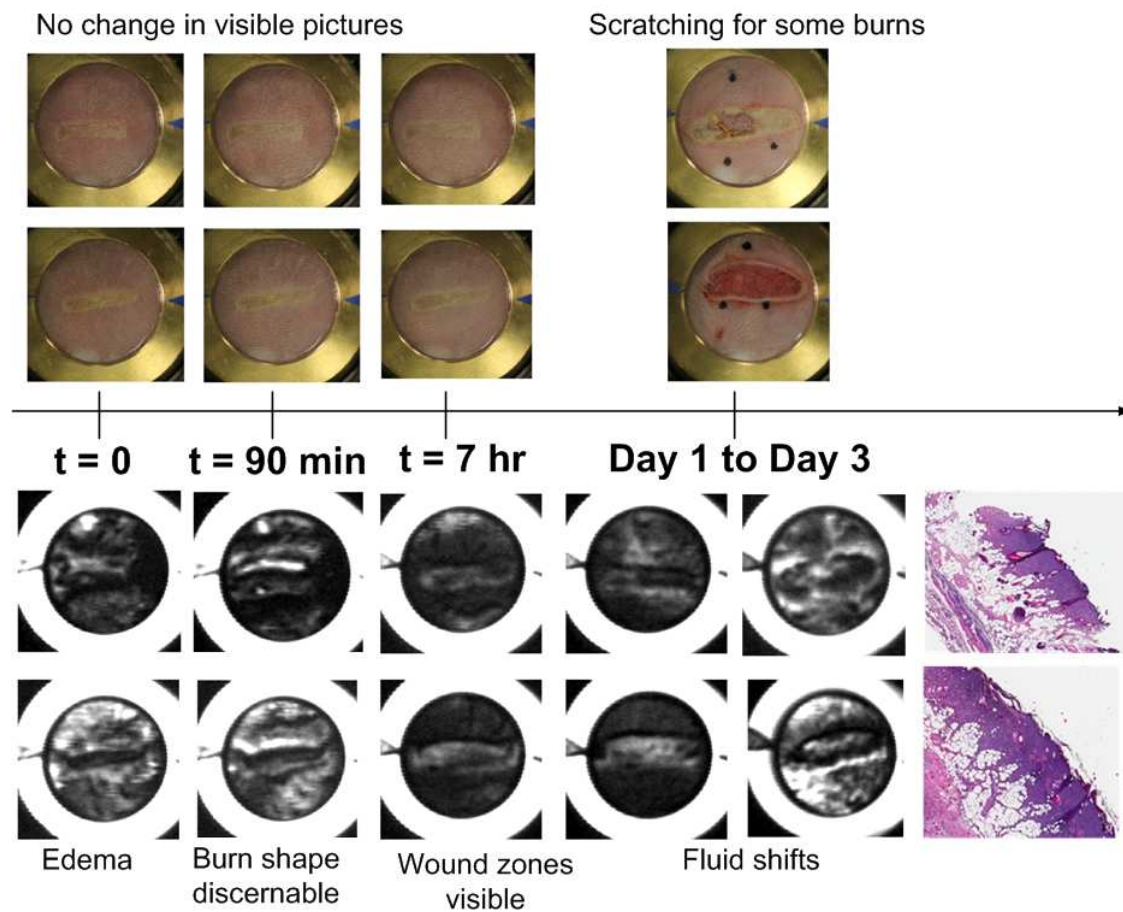
Fig 8.6: Visual summary of observations

8.6 Limitations and improvements:

The study involved a small sample size of 10 subjects. Though repeatability was demonstrated and an attempt to quantitatively analyze the data was made, more subjects are needed to substantiate the above claim. It was observed that the system is prone to drift which

149

adds variability to the data. System issues such as drift, absence of a calibration phantom make it hard to normalize the data across all animals on different days. Control and follow up images could not be compared to the 7 hour images due to lack of external fiducial markers. For some rats, three sharpie dots in the field of view were experimented as fiducial markers. It was observed that the sharpie dots disappeared on day 2. Hence for image registration of all images taken over three days and across all rats, a robust fiducial marker needs to be determined. Finally histological correlation of burn zones was not performed for the above experiments. Lack of THz image to histological registration and financial constraints prevented such an analysis.
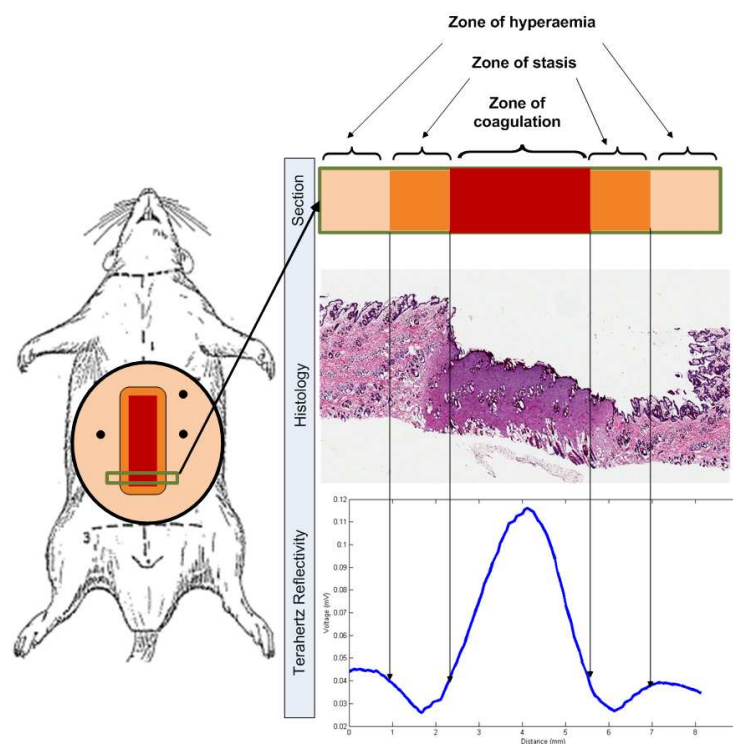
Fig 8.7 Intraspecimen, intraspecimen and histological registration scheme for future experiments

The above figure suggests improvements in image registration over the current set of experiments. Three robust dots in the imaging field of view could solve the intraspecimen, intraspecimen and histological registration all at once. This would allow us to use all the images and correlate with histology.

8.7 Concluding remarks

In summary this work has shown that Reflective THz system can visualize and detect burns of partial and full thickness severities. Burn wounds cause local variations in skin hydration which are exploited by the systems sensitivity to water and translated as contrast in the THz image. The advantage of this technique is two-fold in not only visualizing the burn but also in identifying burn wound zones which presently remain a clinical challenge. The results were obtained in vivo in rats, are repeatable and impervious to the shape and size of rats. Further partial thickness and full thickness burns could be distinguished from one another based on hydration changes that are specific to the physiologic response to the burn type.

References:

[1] AJ Fitzgerald, E Berry, NN Zinovev, S Homer-Vanniasinkam, RE Miles, JM Chamberlain*, et al.*, "Catalogue of human tissue optical properties at terahertz frequencies," *Journal of biological physics,* vol. 29, pp. 123-128, 2003.

[2] RM Woodward, BE Cole, VP Wallace, RJ Pye, DD Arnone, EH Linfield*, et al.*, "Terahertz pulse imaging in reflection geometry of human skin cancer and skin tissue," *Physics in medicine and biology,* vol. 47, pp. 3853-3863, 2002.

[3] VP Wallace, PF Taday, AJ Fitzgerald, RM Woodward, J Cluff, RJ Pye*, et al.*, "Terahertz pulsed imaging and spectroscopy for biomedical and pharmaceutical applications," *Faraday discussions,* vol. 126, pp. 255-263, 2004.

[4] BE Cole, RM Woodward, DA Crawley, VP Wallace, DD Arnone, and M. Pepper, "Terahertz imaging and spectroscopy of human skin in vivo," *Proceedings of SPIE,* vol. 4276, pp. 1-10, 2001.

[5] KF Ross and H. Gordon, "Water in malignant tissue measured by cell refractometry and nuclear magnetic resonance," *Journal of microscopy,* vol. 128, pp. 7-21, 1982.

[6] DW Wilmore, JM Long, AD Mason, RW Skreen, and B. Pruitt, "Catecholamines: Mediator of the hypermetabolic response to thermal injury," *Annals of surgery,* vol. 180, pp. 653-668, 1974.

[7] "Burn incidence and treatment in United States fact sheet," 2007.

[8] J Ruminski, M Kaczmarek, A Renkielska, and A. Nowakowski, "Thermal parametric imaging in the evaluation of skin burn depth," *IEEE Transactions on biomedical engineering,* vol. 54, pp. 303-312, 2007.

[9] DM Mittleman, M Gupta, R Neelamani, RG Baraniuk, JV Rudd, and M. Koch, "Recent advances in Terahertz imaging," *Applied Physics B,* vol. 68, pp. 1085-1094, 1999.

[10] ZD Taylor, RS Singh, MO Culjat, JY Suen, WS Grundfest, H Lee*, et al.*, "Reflective THz imaging of porcine skin burns," *Optics letters,* vol. 33, pp. 1258-1260, 2008.

[11] SW Smye, JM Chamberlain, AJ Fitzgerald, and E. Berry, "The interaction between THz radiation and biological tissue," *Physics in medicine and biology,* vol. 46, pp. R101-R112, 2001.

[12] ZD Taylor, RS Singh, MO Culjat, JY Suen, WS Grundfest, and E. Brown, "THz imaging based on water-concentration contrast," *Proceedings of SPIE,* vol. 6949, pp. 69490D-1-69490-D-8, 2008.

[13] JF Federici, B Schulkin, F Huang, D Gary, R Barat, O Oliviera*, et al.*, "THz imaging and sensing for security applications-explosives, weapons and drugs," *Semiconductor science and technology,* vol. 20, pp. S266-S280, 2005.

[14] P. Siegel, "Terahertz technology in biology and medicine," *IEEE transactions on microwave theory and techniques,* vol. 52, pp. 2438-2447, 2004.

[15] BB Hu and M. Nuss, "Imaging with THz waves," *Optics latters,* vol. 20, pp. 1716-1718, 1995.

[16] DD Arnone, CM Ciesla, A Corchia, S Egusa, M Pepper, JM Chamberlain*, et al.*, "Applications of terahertz technology to medical imaging," *EUROPTO conference on terahertz spectroscopy and applications II,* vol. 3828, pp. 209-219, 1999.

[17]   RM Woodward, EH Linfield, M Pepper, VP Wallace, BE Cole, DD Arnone*, et al.,* "Terahertz pulse imaging in reflection geometry of skin tissue using time-domain analysis techniques," *Proceedings of SPIE,* vol. 4625, pp. 160-169, 2002.

[18]   V. W. AJ Fitzgerald, M Jimenez-Linan, L Bobrow, RJ Pye, AD Puroshottam, DD Arnone, "Terahertz pulsed imaging of human breast tumors," *Radiology,* vol. 239, pp. 533-540, 2006.

[19]   D.A. van Hal, E. Jeremiasse, H.E. Junginger, F. Spies, and J.A. Bouwstra, "Structure of Fully Hydrated Human Stratum Corneum: A Freeze-Fracture Electron Microscopy Study," *J. Invest Dermatol* vol. 106, pp. 89-95, 1996.

[20]   DQ Ho, YM Bello, GL Grove, J Manzoor, AP Lopez, CR Zerweck*, et al.,* "A pilot study of noninvasive methods to assess healed acute and chronic wounds," *Dermatologic surgery,* vol. 26, pp. 42-49, 2000.

[21]   JL Alfonso Sánchez, SB Perepérez, JL Bastida, and M. Martínez, "Cost utility analysis applied to the treatment of burn patients in a specialized center," *Archives of surgery,* vol. 142, pp. 50-57, 2007.

[22]   "Burn incidence and treatment in the US," 2007.

[23]   PA Brigham and E. McLoughlin, "Burn incidence and medical care use in the United States: estimates, trends, and data sources," *Journal of burn care and rehabilitation,* vol. 17, pp. 95-107, 1996.

[24]   LA Fingerhut and M. Warner, "National vital statistics system," *National center for health sciences,* 1999.

[25]   TA Fordyce, M Kelsh, ET Lu, JD Sahl, and J. Yager, "Thermal burns and electric injuries among electric utility workers, 1995-2004," *Burns,* vol. 33, pp. 209-220, 2007.

[26]   "National burn repository," *American burn association,* 2005.

[27]   JR Wheeler , RV Harrison , RA Wolfe , and B. Payne, "The effects of burn severity and institutional differences on the costs of care," *Med Care,* vol. 21, pp. 1192-1203, 1983.

[28]   D. Herndon, "Total burn care," p. 16, 2006.

[29]   MM Celis, OE Suman, TT Huang, P Yen, and D. Herndon, "Effect of a supervised exercise and physiotherapy program on surgical interventions in children with thermal injury," *Journal of burn care and rehabilitation,* vol. 24, pp. 57-61, 2003.

[30]   NA Cucuzzo, A Ferrando, and D. Herndon, "The effects of exercise programming vs traditional outpatient therapy in the rehabilitation of severely burned children," *Journal of burn care and rehabilitation,* vol. 22, pp. 214-220, 2001.

[31]   EA Deitch, TM Wheelahan , MP Rose , J Clothier, and J. Cotter, "Hypertrophic burn scars: analysis of variables.," *Journal of trauma,* vol. 23, pp. 895-898, 1983.

[32]   Z Dedovic, I Koupilova , and P. Brychta, "Time trends in incidence of hypertrophic scarring in children treated for burns," *Acta Chir Plast* vol. 41, pp. 87-90, 1999.

[33]   WS McDonald and E. Deitch, "Hypertrophic skin grafts in burned patients; a prospective analysis of variables," *Journal of trauma,* vol. 27, pp. 147-150, 1987.

[34]   ED Spurr and P. Shakespere, "Incidence of hypertrophic scarring in burn-injured children," *Burns,* vol. 16, pp. 179-181, 1990.

[35]   KM Bombaro, LH Engrav, GJ Carrougher, SH Weichman, L Faucher, BA Costa*, et al.,* "What is the prevalence of hypertrophic scarring following burns?," *Burns,* vol. 29, pp. 299-302, 2003.

[36] M. S. Richard P, Staley M, Johnson R.M. "." J Burn Care Rehabil 2000; 21:506-512, "Multimodal versus progressive treatment techniques to correct burn scar contractures," *Journal of burn care and rehabilitation,* vol. 21, pp. 506-512, 2000.

[37] B Henderson, GH Koepke, and I. Feller, "Peripheral polyneuropathy among patients with burns," *Arch Phys Med Rehabil,* vol. 52, pp. 149-151, 1971.

[38] K Kowalske, R Holavanahalli, and P. Helm, "Neuropathy after burn injury," *Journal of burn care and rehabilitation,* vol. 22, pp. 353-357, 2001.

[39] AJ Margherita, LR Robinson, DD Heimbach , VL Fishfader , VASchneider , and DJones, "Burn-associated peripheral polyneuropathy. A search for causative factors," *Am J Phys Med Rehabil,* vol. 74, pp. 28-32, 1995.

[40] P. Esselman, "Burn Rehabilitation: An Overview," *Arch Phys Med Rehabil,* vol. 12, pp. S3-S6, 2007.

[41] D. M. Jackson, "The diagnosis of depth of burning," *The british journal of surgery,* vol. 40, p. 588, 1953.

[42] D. Jackson, "The diagnosis of depth of burning," *Br. J. Surg.,* vol. 40, pp. 588-596, 1953.

[43] V. Singh, L. Devgan, S. Bhat, and S. M. Milner, "The Pathogenesis of Burn Wound Conversion," *Annals of Plastic Surgery,* vol. 59, pp. 109-115, 109.

[44] L. DeSanti, "Pathophysiology and Current Management of Burn Injury," *Advances in Skin & Wound Care,* vol. 18, pp. 323-332, 2005.

[45] B. Latha and M. Babu, "The involvement of free radicals in burn injury: a review," *Burns,* vol. 27, pp. 309-317, 2001.

[46] L.H. Evers, D. Bhavsar, and P. Mailander, "The biology of burn injury," *Experimental Dermatology,* vol. 19, pp. 777-783, 2010.

[47] G. Arturson and S. Mellander, "Acute changes in Capillary Filtration and Diffusion in Experimental Burn Injury," *Acta physiol,* vol. 62, pp. 457-463, 1964.

[48] S. Sevitt, "Early and Delayed Edema and Increase in Capillary Permeability after Burns of the Skin," *J. Path. Bact.,* vol. LXXV, pp. 27-37, 1958.

[49] H.F. Carvajal, B.H. Brouhard, and H. A. Linares, "Effect of antihistamine antiseretonin and ganglionic blocking agents upon incresed capillary permeability following burn trauma," *J. Trauma,* vol. 15, pp. 969-975, 1975.

[50] O. Cope and F. D. Moore, "The study of capillary permeability in experimental burns and burn shock using radioactive dyes in blood lymph," *J. Clin. Invest.,* vol. 23, pp. 241-257, 1944.

[51] G.G. Gaulitz, J. Song, D.N. Herndon, C.S. Finnerty, D. Boehning, J.M. Barral*, et al.*, "Characterization of the Inflammatory Response During Acute and Post-Acute Phases After Severe Burn," *Shock,* vol. 30, pp. 503-507, 2008.

[52] R. H. Demling, "The Burn Edema Process: Current Concepts," *Journal of Burn Care & Rehabilitation,* vol. 26, pp. 207-227, 2005.

[53] L. L. Leape, "Early Burn Wound Changes," *Journal of Pediatric Surgery,* vol. 3, pp. 292-299, 1968.

[54] H.F. Carvajal, H.A. Linares, and B. H. Brouhard, "Relationship of burn size to vascular permeability changes in rats," *Surg Gynecol Obstet,* vol. 149, pp. 193-202, 1979.

[55] G. Arturson and C. E. Johnson, "Transcapillary transport after thermal injury," *Scand J Plast Reconstr Surg,* vol. 13, pp. 29-38, 1979.

[56] S. Sharar, D. Humbach, M. Green, R.K. Winn, and J. Hildebrandt, "Effect of body surface thermal injury on renal and cutaneous blood flow in goats," *J. Burn care Rehab,* vol. 9, pp. 26-30, 1988.

[57] A.J. Singer and R. A. F. Clark, "Cutaneous Wound Healing," *The New England Journal of Medicine,* vol. 341, pp. 738-746, 1999.

[58] V. Singh, L. Devgan, and S. M. Milner, "The Pathogenesis of Burn Wound Conversion," *Annals of Plastic Surgery,* vol. 59, pp. 109-115, 2007.

[59] C.C Kao and W. L. Garner, "Acute Burns," *Plast Reconstr Surg. ,* vol. 105, pp. 2482-2492, 2000.

[60] M.C. Robson, E.J. Del Brecco, and J. P. Heggers, "The effect of prostaglandins on the dermal microcirculation after burning, and the inhibiiton of the effect by specific pharmacological agents," *Plast Reconstr Surg.,* vol. 63, pp. 781-787, 1979.

[61] H.F. Zhang, K. Maslov, G. Stoica, and L. V. Wang, "Imaging acute thermal burns by photoacoustic microscopy," *Journal of Biomedical Optics,* vol. 11, pp. 054033-1-054033-5, 2006.

[62] B.S. Atiyeh, S.W. Gunn, and S. N. Hayek, "State of the Art in Burn Treatment," *World journal of Surgery,* vol. 29, pp. 131-148, 2005.

[63] J. F. de Boer, S.M. Srinivas, A. Malekafzali, Z. Chen, and J. S. Nelson, "Imaging thermally damaged tissue by Polarization Sensitive Optical Coherence Tomography," *Optics Express,* vol. 3, pp. 212-218, 1998.

[64] A.G. Hargroder , J.E. Davidson, D.G. Luther, and J. F. Head, "Infrared imaging of burn wounds to determine burn depth," in *SPIE Conference on Infrared Technology and Applications XXV*, 1999, pp. 103-108.

[65] J.M. Still, E.J. Law, K.G. Klaavuhn, T.C. Island, and J. Z. Holtz, "Diagnosis of burn depth using laser-induced indocyanine green fluorescence: a preliminary clinical trial," *Burns,* vol. 27, pp. 364-371, 2001.

[66] J. V. Frangioni, "In vivo-infrared fluorescence imaging," *Current Opinion in Chemical Biology* vol. 7, pp. 626-634, 2003.

[67] R. Pethig, "Dielectric properties of body tissues.," *Clin. Phys. Physiol. Meas. ,* vol. 8, pp. A5-A12, 1987.

[68] R. L. S Gabriel S, C Gabriel "The dielectric properties of biological tissues: III. Parametric models for the dielectric spectrum of tissues " *Phys. Med. Biol. ,* vol. 41, pp. 2271-2293, 1996.

[69] E Pickwell, BE Cole, AJ Fitzgerald, VP Wallace, and M. Pepper, "Simulation of terahertz pulse propogation in biological systems," *Applied physics letters,* vol. 84, pp. 2190-2192, 2004.

[70] C. S. JT Kindt, "Far-infrared dielectric proprties of polar liquids probed by femtosecond terahertz pulse spectroscopy," *Journal of physical chemistry,* vol. 100, pp. 10373-10379, 1996.

[71] P. A. C Ronne, SR Keilding, "THz spectroscopy of liquid H2O and D2O," *Physical review letters,* vol. 82, pp. 2888-2891, 1999.

[72] A. R. SI Alekseev, MK Logani, MC Ziskin, "Millimeter wave dosimetry of human skin," *Bioelectromagnetics,* vol. 29, pp. 65-70, 2008.

[73] L. T. C Romme, A Wallqvist, KV Mikkelsen, "Investigation of the temperature dependence of dielectric relaxation in liquid water by THz reflection spectroscopy

and molecular dynamics simulation," *Journal of chemical physics,* vol. 18, pp. 5319-5331, 1997.

[74] K. S. T Loffler, S Czasch, T Bauer, HG Roskos, "Visualization and classification in biomedical terahertz pulsed imaging," *Phys Med Biol,* vol. 47, pp. 3847-3852, 2002.

[75] K. C. A Rogalski, "Infrared device and techniques," *Opto electronics review,* vol. 10, pp. 111-136, 2002.

[76] DM mittleman, M Gupta, R Neelaman, RG Baraniuk, JV Rudd, and M. Koch, "Recent advances in terahertz imaging," *Applied physics B,* vol. 68, pp. 1085-1094, 1999.

[77] JP Dougherty, GD Jubic, and W. Kiser, "Terahertz imaging of burned tissue," *Proceedings of SPIE,* vol. 6472, pp. N-1 - N-9, 2007.

[78] A. S. J Maurer, W Ebert, H Bauer, R Felix, "Contrast-enhanced high resolution magnetic resonance imaging of pigmented malignant melanoma Mn-TPPS4 & Gd-DTPA: Experimental results," *Melanoma Res* vol. 10, pp. 40-46, 2000.

[79] J. B. I Idy-Peretti, FA, SB Richard, BG Querleux, RV Cluzan, "Lymphedematous skin and subcutis: In vivo resolution magnetic resonance imaging evaluation," *Journal of investigative dermatology,* vol. 110, pp. 782-787, 1998.

[80] A. J. MR Rajeshwari, A Sharma, NR Jagananthan, U Sharma, MN dEGAONKAR, "Evaluation of skin tumors by magnetic resonance imaging," *Laboratory investigation,* vol. 83, pp. 1279-1283, 2003.

[81] M. M. S Nouveau-Richard, P Bastien, O de Lacharriere, "In vivo epidermal thickness measurement: ultrasound vs. confocal imaging.," *Skin research and technology,* vol. 10, pp. 136-140, 2004.

[82] H. E. C Passman, "A 100-MHz ultrasound imaging system for dermatologic and ophthalmologic diagnostics." IEEE transactions on ultrasonic's, ferroelectrics and frequency control " *IEEE transactions on ultrasonic's, ferroelectrics and frequency control,* vol. 43, pp. 545-552, 1996.

[83] S. P. JA Sanchez, ZL Bastida, MM Martinez, "Cost-utility analysis applied to the treatment of burn patients in a specialized center," *Archives of surgery,* vol. 142, pp. 50-57, 2007.

[84] W. S. EJ Droog, F Sjoberg, "Measurement of depth of burns by laser Doppler perfusion imaging," *Burns,* vol. 27, pp. 561-568, 2001.

[85] P. Shakespere, "Looking at burn wounds: The AB Wallace memorial lecture," *Burns,* vol. 18, pp. 287-295, 1992.

[86] K. M. HF Zhang, LV Wang, "Imaging acute thermal burns by photoacoustic microscopy," *Journal of biomedical optics,* vol. 11, pp. 054033-1-054033-5, 2006.

[87] BS Atiyeh, SW Gunn, and S. Hayek, "State of art in burn treatment," *World journal of surgery,* vol. 29, pp. 131-148, 2005.

[88] K. M. H.F. Zhang, L.V. Wang, "Imaging acute thermal burns by photoacoustic microscopy," *Journal of biomedical optics,* vol. 11, pp. 054033-1 - 054033-5, 2006.

[89] S. S. S. J.F. de Boer, A. Malekafzali, Z. Chen, J.S. Nelson, "Imaging thermally damaged tissue by polarization sensitive optical coherence tomography," *Optics Express,* vol. 3, pp. 212-218, 1998.

[90] J. D. AG Hargroder, DG Luther, JF Head, "Infrared imaging of burn wounds to determine burn depth," *Part of the SPIE Conference on Infrared Technology and Applications XXV,* vol. 3698, pp. 103-108, 1999.

[91]   JM Still, EJ Law, KG Klaavuhn, TC Island, and J. Holtz, "Diagnosis of burn depth using laser-induced indocyanine green fluorescence: a preliminary clinical trial," *Burns,* vol. 27, pp. 364-371, 2001.

[92]   J. Frangioni, "In vivo-infrared fluorescence imaging," *Current Opinion in Chemical Biology,* vol. 7, pp. 626-634, 2003.

[93]   N. Karpowicz, H. Zhong, J. Xu, K.-I. Lin, J.-S. Hwang, and X. C. Zhang, "Comparison betweeen pulsed terahertz time-domain imaging and continuous wave terahertz imaging," *Semicond. Sci. Technol. ,* vol. 20, pp. 293-299, 2005.

[94]   DA Crawley, C Longbottom, BE Cole, CM Ciesla, D Arnone, VP Wallace*, et al.*, "Terahertz pulse imaging: A pilot study of potential applications in dentistry," *Caries research,* vol. 37, pp. 352-359, 2003.

[95]   D.A. Crawley, C. Longbottom, B.E. Cole, C.M. Ciesla, D. Arnone, V.P. Wallace*, et al.*, "Terahertz Pulse Imaging: A Pilot Study of Potential Applications in Dentistry," *Caries Research,* vol. 37, pp. 352-359, 2001.

[96]   W. L. DB Bennett, ZD Taylor, WS Grundfest, ER Brown, "Stratified media model for terahertz reflectometry of the skin," *IEEE sensors journal,* vol. 11, pp. 1253-1262, 2011.

[97]   S. W. A Dreyhaupt, M Helm, "Optimum excitation conditions for the generation of high electric terahertz radiation from an oscillator driven photoconductive device," *Optics letters,* vol. 31, pp. 1546-1548, 2006.

[98]   D. G. M van Exter, "Characterization of an optpelectric terahertz beam system " *IEEE transactions on microwave theory and techniques,* vol. 38, pp. 1684-1691, 1990.

[99]   A Gurtler, C Winnewisser, H Helm, and P. Jepsen, "Terahertz pulse propogation in the near field and the far field," *Journal of the optical society of America A,* vol. 17, pp. 74-83, 2000.

[100]   B. A. G. J.M Khosrofian, "Measurement of a Gaussian laser beam diameter through the direct inversion of knife-edge data," *Applied optics* vol. 22, pp. 3406-3410, 1983.

[101]   JE Bjarnson, TLJ Chan, AWM Lee, MA Celis, and E. Brown, "Millimeter-wave, terahertz, and mid-infrared transmission through common clothing," *Applied Physics Letters,* vol. 85, pp. 519-521, 2004.

[102]   S Mickan, D Abbott, J Munch, XC Zhang, and T. v. Doorn, "Analysis of system trade-offs for terahertz imaging," *Microelectronics journal,* vol. 31, pp. 503-514, 2000.

[103]   R Appleby, PR Coward, and G. Sinclair, "Terahertz detection of illegal objects," *NATO Security through Science series,* vol. 2007, pp. 225-240, 2007.

[104]   GR Ziegler, SSH Rizvi, and J. Acton, "Relationship of water content to Textural characteristics, water activity and thermal conductivity of commercial sausages," *Journal of Food science,* vol. 52, pp. 901-905, 1987.

[105]   T. AP Moloney, Dunsany, *The fat content of meat and meat products.* Cambridge: Woodhead publishing limited, 2002.

[106]   J. S. Garrow, "New approaches to body composition," *The American Journal of chemical nutrition,* vol. 35, pp. 1152-1158, 1982.

[107]   C. T. AR Hargens, PD Gollnick, SJ Mubarak, BJ Tucker, WH Akeson, "Fluid shits and muscle function in humans during acute simulated weightlessness," *Journal of applied physiology,* vol. 54, pp. 1003-1009, 1983.

[108]   "Oral Health in America: A Report of the Surgeon General," Rockville2000.

[109] ".National Health and Nutrition Examination Survey III," National Center for Health Statistics (NCHS). Centers for Disease Control and Prevention (CDC), unpublished data., Hyattsville1988–1994.

[110] H. K. Schade U, Martin M.C & Fried D, "THz near-field imaging of biological tissues employing synchrotron radiation," *Lawrence Berkeley National Laboratory,* 2004.

[111] M. N. EAM Kidd, RF Wilson, "Prevalence of clinically undetected and untreated molar occlusal dentine caries in adolescents on the Isle of Wight," *Carries Res,* vol. 26, pp. 397-401, 1992.

[112] J. D. S. KL Weerheijim, WE Van Amerongen, J DE Graaf, "Sealing of occlusal hidden caries lesions: an alternative for curative treatment?," *J Dent Child* vol. 59, pp. 263-268, 1992.

[113] J. T. B. B Angmar-Mansson B, "Advances in methods for diagnosing coronal caries -a review.," *Adv Dent Res,* vol. 7, pp. 70-79, 1993.

[114] R. H. CE Ketley, "Visual and radiographic diagnosis of occlusal caries in first permanent molars and in second primary molars," *Br Dent J,* vol. 174, pp. 364-370, 1993.

[115] E. K. DNJ Ricketts, BGN Smith, RF Wilson, "Clinical and radiographic diagnosis of occlusal caries: a study in vitro," *J Oral Rehabil,* vol. 22, pp. 15-20, 1995.

[116] C. L. C. MC Huysmans, "The challenges of validating diagnostic methods and selecting appropriate gold standards.," *J Dental Res,* vol. 83, pp. 48-52, 2004.

[117] V. W. E Pickwell, BE Cole, S Ali, C Longbottom, RJM Lynch, M Pepper "A comparison of Terahertz Pulsed Imaging with Transmission Microradiography for Depth Measurement of Enamel Demineralisation in vitro," *Caries Res,* vol. 41, pp. 49-55, 2007.

[118] A. F. NN Zinov'ev, SM Strafford, DJ Wood, FA Carmichael, RE Miles, MA Smith, JM Chamberlain, "Identification of Tooth Decay using Terahertz Imaging and Spectroscopy," *IEEE* pp. 13-14, 2002.

[119] D. A. CM Ciesla, A Corchia, D Crawley, C Longbottom, EH Linfield "Biomedical applications of terahertz pulse imaging," *Proc SPIE,* vol. 3934, pp. 73-81, 2000.

[120] Y. J. J Ryu, S Baek, J Lee, S Kim , J Kim, "Diagnosis of Dental Cavity and Osteoporosis Using Terahertz Transmission Images," *Springer Series in Chemical Physics,* vol. 66, pp. 265-267, 2001.

[121] C. L. D Crawley, VP Wallace, BE Cole, D Arnone, M Pepper M. "" 2003; 8(2):303-307., "Three-dimensional terahertz pulse imaging of dental tissue.," *Journal of Biomedical Optics,* vol. 8, pp. 303-307, 2003.

[122] J. W. NJC Bauer, FHM Jongsma, WF March, F Hendrikse, M Motamedi M, "Noninvasive Assessment of the Hydration Gradient across the Cornea Using Confocal Raman Spectroscopy.," *IOVS,* vol. 39, pp. 831-835, 1998.

[123] K. M. DW Leonard, "Refractive indices of the collagen fibrils and extrafibrillar material of the corneal stroma," *Biophys. J,* vol. 72, p. 1382, 1997.

[124] S. Mishima, "Corneal thickness," *Surv Opthalmol,* vol. 13, pp. 57-96, 1968.

[125] J. W. J. YL Kim, TK Goldstick, MR Glucksberg "Variation of corneal refractive index with hydration," *Physics in Medicine and Biology,* vol. 49, pp. 859-868, 2004.

[126] S. M. BO Hedsby, "The thickness-hydration relationship of the cornea.," *Exp. Eye. Res.,* vol. 5, 1966.

[127] A. B. NG Congdon, K Bandeen-Roche, D Grover, HA Quigley, "Central Corneal Thickness and Corneal Hysteresis Associated with Glaucoma Damage," *American Journal of Opthamology,* vol. 141, p. 868, 2006.

[128] J. J. WS Kim, "Corneal Hydration Affects Ablation during Laser In Situ Keratomileusis Surgery," *Cornea,* vol. 20, pp. 394-397, 2001.

[129] G. C. DCW Siew, RP Cooney, PM Wiggins, "Micro-Raman spectroscopic study of organ cultured cornea," *J Raman Spectroscopy* vol. 26, pp. 3-8, 1995.

[130] J. W. NJ Bauer, FHM Jongsma,F Hendriske M Motamedi, "Noninvasive Assessment of the Hydration Gradient across the Cornea Using Confocal Raman Spectroscopy.," *Iovs* vol. 39, pp. 831-835.

[131] B. M. M Bohnke, R Walti, JJ Ballif, P Chavanne, R Gianotti, RP Salathe, "Precision & Reproducibility of measurements of human corneal thickness with Rapid Optical Low-Coherence Reflectometry (OLCR)," *Journal of Biomedical Optics,* vol. 4, pp. 152-156, 1999.

[132] R. S. Y Li , D Huang, "Corneal Pachymetry Mapping with High-speed Optical Coherence Tomography.," *Ophthalmology,* vol. 113, pp. 792-799.

[133] P. T. RS Singh, JL Bourges, JP Hubschman, DB Bennett, ZD Taylor, H Lee, ER Brown, WS Grundfest, MO Culjat, "Terahertz Sensing of Corneal Hydration," *Proc. of IEEE EMBS,* 2010.

[134] RM Nalbandian, RL Henry, KW Balko, DV Adams, and NR Neuman, "Pluronic F-127 gel preparation as an artificial skin in the treatment of third-degree burns in pigs," *Journal of Biomedical Materials Research,* vol. 21, pp. 1135-1148, 1987.

[135] KF Ross and R. Gordon, "Water in malignant tissue measured by cell refractometry and nuclear magnetic resonance," *J. Microsc.,* vol. 128, pp. 7-21, 1982.

[136] JH Chen, HE Avram, LE Crooks, M Arakawa, L Kaufman, and A. Briton, "In vivo relaxation times and hydrogen density at 0.063-4.85 T in rats with implanted mammary adenocarcinomas," *Radiology,* vol. 184, pp. 427-434, 1992.

[137] E K Rofstad, E Steinsland, O Kaalhus, Y B Chang, B Hovik, and H Lyng, "Magnetic resonance imaging of human melanoma xenografts in vivo: proton spin lattice and spin-spin relaxation times versus fractional water content and fraction of necrotic tumour tissue," *Int. J. Radiat. Biol.,* vol. 65, pp. 387-401, 1994.

[138] DA van Hal, E Jeremiasse, HE Junginger, F Spies, and J. Bouwstra, "Structure of Fully Hydrated Human Stratum Corneum: A Freeze-Fracture Electron Microscopy Study," *J. Invest Dermatol* vol. 106, pp. 89-95, 1996.

[139] DQ Ho, YM Bello, GL Grove, J Manzoor, AP Lopez, CR Zerweck*, et al.*, "A Pilot Study of Noninvasive Methods to Assess Healed Acute and Chronic Wounds," *Dermatol Surg* vol. 26, pp. 42-49, 2000.

[140] AJ Fitzgerald, E Berry, NN Zinovev, GC Walker, MA Smith, and J. Chamberlain, "An introduction to medical imaging with coherent terahertz frequency radiation" *Physics in medicine and biology,* vol. 47, pp. R67-R84, 2002.

[141] L Chrit, P Bastien, GD Sockalingum, D Batisse, F Leroy, M Manfait*, et al.*, "An in vivo Randomized Study of Human Slin Moisturization by a New Confocal Raman Fiber-Optic Microprobe: Assessment of a Glycerol-Based Hydration Cream," *Skin Pharmacol Physiol* vol. 19, pp. 207-215, 2006.

[142] R. Bazin and C. Fanchon, "Equivalence of face and volar forearm for the testing of moisturizing and firming effect of cosmetics in hydration and biomechanical studies," *International Journal of Cosmetic Science,* vol. 28, pp. 453-460, 2006.

[143] P Sator, JB Schmidt, and H. Honigsmann, "Comparison of epidermal hydration and skin surface lipids in healthy individuals and in patients with atopic dermatitis," *J Am Acad Dermatol,* vol. 48, pp. 352-358, 2002.

[144] L Coderich, M de Pera, N Perez-Cullel, J Estelrich, and A de la Maza, "The effect of liposomes on skin barrier structure," *Skin Pharmacol Appl Skin Physiol,* vol. 12, pp. 235-246, 1999.

[145] T Marjukka Suhonen, J. Bouwstra, and A. Urtti, "Chemical enhancement of percutaneous absorption in relation to stratum corneum structural alterations," *Journal of controlled release,* vol. 59, pp. 149-161, 1999.

[146] S Verdier-Sevrain and F. Bonte, "Skin hydration: a review on its molecular mechanisms," *Journal od cosmetic dermatology,* vol. 6, pp. 75-82, 2007.

[147] H Tagami, Y Kanamaru, K Inoue, S Suehisa, F Inoue, K Iwatsuki*, et al.*, "Water Sorption-desorption Test of the Skin in vivo for functional assessment of the Stratum Corneum," *The Journal of Investigative Dermatology* vol. 78, pp. 425-428, 1982.

[148] E. Berardesca, "EEMCO guidance for the assessment of Stratum Corneum hydration: electrical methods," *Skin Research and Technology,* vol. 3, pp. 126-132, 1997.

[149] RR Warner, MC Myers, and D. Taylor, "Electron probe analysis of human skin: determination of the water concentration profile " *J Invest Dermatol,* vol. 90, pp. 218-224, 1988.

[150] W Meyer, R Schwarz, and K. Neurand, "The skin of domestic mammals as a model for the human skin; with special reference to the domestic pig," *Current problems in dermatology,* vol. 7, pp. 39-52, 1978.

[151] HQ Marcarian and M. Calhoun, "Microscopic anatomy of the integument of adult swine," *American journal of veterinary research,* vol. 27, pp. 765-772, 1966.

[152] P. Forbes, *Vascular supply of the skin and hair in swine*: Oxford: Pergamon, 1967.

[153] H. Carter, *Variation in the hair follicle population of the mamalian skin.* New York: Elsevier, 1965.

[154] N Nicolaides, HC Fu, and G. Rice, "The skin surface lipids of man compared with those of eighteen species of animals," *Journal of Investigative Dermatology,* vol. 51, pp. 83-89, 1968.

[155] G. Weinstein, "Autoradiographic studies of turnover time and protein synthesis in pig epidermis," *Journal of Investigative Dermatology,* vol. 44, pp. 413-419, 1965.

[156] TP Sullivan, WH Eaglstein, SC Davis, and P. Mertz, "The pig as a model for human wound healing," *Wound repair and regeneration,* vol. 9, pp. 66-76, 2001.

[157] VK Gupta, JL Zatz, and M. Rerek, "Percutaneous absorption of sunscreens through micro-yucatan pig skin in vitro," *Pharmaceutical Research,* vol. 16, pp. 1602-1607, 1999.

[158] GA Simon and H. Maibach, "The pig as an experimental animal model of percutaneous permeation in Man: Qualitative and Quantitative observations - An overview," *Skin Pharmacol Appl Skin Physiol,* vol. 13, pp. 229-234, 2000.

[159] T Maisch, C Worlicek, P Babilas, M Landthaler, and R.-M. Szeimies, "A HCl/alcohol formulation increased 5-aminolevulinic acid skin distribution using an ex vivo full

thickness porcine skin model," *Experimental Dermatology,* vol. 17, pp. 813-820, 2008.

[160] N Sekkat, YN Kalia, and R. Guy, "Biophysical study of porcine ear skin in vitro and its comparison to human skin in vivo," *Journal of Pharmaceutical Sciences,* vol. 91, pp. 2376-2381, 2002.

[161] M. Bouclier, D. Cavey, N. Kail, and C. Hensby, "Experimental models in skin pharmacology," *Pharmacol Rev.,* vol. 42, pp. 127-154, 1990.

[162] D.Q. Ho, Y.M. Bello, G.L. Grove, J. Manzoor, A.P. Lopez, C.R. Zerweck*, et al.,* "A Pilot Study of Noninvasive Methods to Assess Healed Acute and Chronic Wounds," *Dermatol Surg* vol. 26, pp. 42-49, 2000.

[163] J.W. Fluhr, M. Gloor', S. Lazzerini, P. Kleesz, R. Grieshaber, and E. Berardesca, "Comparative study of five instruments measuring stratum corneurn hydration (Comeometer CM 820 and CM 825, Skicon 200, Nova DPM 9003, DermaLab). Part I. In vitro," *Skin Research and Technology,* vol. 5, pp. 161-170, 1999.

[164] R.M. Woodward, B.E. Cole, V.P. Wallace, R.J. Pye , D.D. Arnone, E.H. Linfield*, et al.,* "Terahertz pulse imaging in reflection geometry of human skin cancer and skin tissue," *Physics in Medicine and Biology,* vol. 47, pp. 3853-3863, 2002.

[165] T.M. Suhonen, J.A. Bouwstra, and A. Urtti, "Chemical enhancement of percutaneous absorption in relation to stratum corneum structural alterations," *Journal of Controlled Release,* vol. 59, pp. 149-161, 1999.

[166] C. Gabriel, S. Gabriel, and E. Corthout, "The dielectric properties of biological tissues: I. Literature survey,," *Physics in Medicine and Biology,* vol. 41, pp. 2231-2249, 1996.

[167] H. Tagami, Y. Kanamaru, K. Inque, S. Suehisa, F. Inque, K. Iwatsuki*, et al.,* "Water Sorption desorption Test of the skin in vivo for functional assessment of the Stratum Corneum," *Journal of Investigative Dermatology,* vol. 78, pp. 425-482, 1982.

[168] K. Martin, "In vivo Measurements of Water in Skin by Near-Infrared Reflectance," *Applied Spectroscopy,* vol. 52, pp. 1001-1007.

[169] S. Naito, M. Hoshi, and S. Mishimo, "In vivo dielectric analysis of free water content of biomaterials by time domain reflectometry," *Anal Biochem,* vol. 251, pp. 163-172, 1997.

[170] E.R Brown, Z.D. Taylor, P. Tewari, R.S. Singh, M.O. Culjat, D.B. Bennett*, et al.,* "THz Imaging of Skin Tissue – Exploiting the Strong Reflectivity of Liquid Water," in *Infrared Millimeter & Terahertz Waves*, 2010.

[171] P.T. Pugliese and A. J. Milligan, *Bioengineering and the skin*: MTP Press, 1981.

[172] J.E. Bertie, M.K. Ahmed, and H. H. Eysel, "Infrared intensities of liquids, 5. Optical dielectric constants, integrated intensities, and dipole moment derivatives of H2O & D2O at 22 C," *J. Phys. Chem.,* vol. 93, pp. 2210-2218, 1989.

[173] R. Bazin and C. Fanchon, "Equivalence of face and volar forearm for the testing of moisturizing and firming effect of cosmetics in hydration and biomechanical studies," *International Journal of cosmetic science,* vol. 28, pp. 453-460, 2006.

[174] S.L. Zhang, C.L. Meyers, K. Subramaniam, and T. M. Hancewicz, "Near infrared imaging for measuring and visualizing skin hydration. A comparision with visual assessment and electrical methods," *Journal of Biomedical Optics* vol. 10, 2005.

[175] R.R Warner, K.J. Stone, and Y. L. Boissy, "Hydration Disrupts Human Stratum Corneum Ultrastructure," *J. Invest Dermatol,* vol. 110, pp. 275-284, 1998.

[176] FX Heredero, C Hamann, JM Obispo Martin, C Rodriguez Arias, and S. C. Menchero, "Experimental burn models," *Annals of Burns and Fire disaster,* vol. 9, 1996.

[177] D Kistler, B Hafemann, and K. Schmidt, "A model to reproduce predictable full-thickness burns in an experimental animal," *Burns,* vol. 14, pp. 297-302, 1988.

[178] KC Arthur, HP Ehrlich, RL Trelstad, MJ Koroly, ME Schattenkerk, and R. Malt, "Differences in healing of skin wounds caused by burna nd freeze injuries," vol. 191, pp. 244-248, 1980.

[179] A.J. Singer, L. Berruti, H.C. Thode, and S. A. McClain, "Standardized Burn Model Using a Multiparametric Histologic Analysis of Burn Depth," *Academic Emergency Medicine,* vol. 7, pp. 1-6, 2000.

[180] A.M.J. Watta, M.P.H. Tyler, M.E. Perry, A.H.N. Roberts, and D. A. McGrouther, "Burn depth and its histological measurement," *Burns,* vol. 27, pp. 154-160, 2001.

[181] T. Lund, H. Onarheim, and R. K. Reed, "Pathogenesis of Edema formation in Burn Injuries," *World journal of Surgery,* vol. 16, pp. 2-9, 1992.

[182] B.H. Brouhard, H.F. Carvajal, and H. A. Linares, "Burn Edema and Protein Leakage in the Rat," *Microvascular Research,* vol. 15, pp. 221-228, 1978.

[183] S. Langer, O. Goertz, L. Steinstraesser, C. KUHNEN, H.U. Steinau, and H. H. Homann, "New model for in vivo investigation after microvascular breakdown in burns: use of intravital fluorescent microscopy," *Burns,* vol. 31, pp. 168-174, 2005.

[184] H.A. Green, D. Bua, R.R. Anderson, and N. S. Nishioka, "Burn Depth Estimation Using Indocyanine Green Fluorescence," *Arch Dermatol,* vol. 128, pp. 43-49, 1992.